Toward Efficient Si-based Anodes for Li-ion Batteries for EV Application

DISSERTATION

submitted in partial fulfillment of the requirements for the degree of

Doktor/in der technischen Wissenschaften

by

Arlavinda Rezqita

Registration Number 1328919

to the Institute of Chemical Technologies and Analytics

at the Vienna University of Technology

Advisor : Prof. Dr. Hermann Kronberger

The dissertation has been reviewed by :

Prof. Dr. Atanaska Trifonova	Prof. Dr. Günter Fafilek

Vienna, 27.11.2016

Arlavinda Rezqita

Declaration of Authorship

Arlavinda Rezqita

Vorgartenstrasse 67/41, 1200, Vienna, Austria

I hereby declare that I have written this Doctoral Dissertation independently, that I have completely specified the utilized sources and resources and that I have definitely marked all parts of the work including tables, maps and figures which belong to other works or to the internet, literally or extracted, by referencing the source as borrowed.

Vienna, November 2016

_____

Arlavinda Rezqita

Acknowledgement

A special thanks to my family for all their endless love and support. For my mother who always encourages me to pursue my dreams. For my father who made sacrifices on my behalf and showed me resilience. Lastly, I would like to thank to Bernd Plassnegger who is supportive and encouraging during my final year. Thank you.

<div align="right">

Arlavinda Rezqita

Vienna, November 2016

</div>

Abstract

Li-ion batteries technology dominates the market today because it exhibits both high gravimetric and volumetric energy density as well as a long lifespan. However, to satisfy current demands, especially for electrical vehicle application, many improvements on Li-ion batteries are necessary. Increasing the energy density of Li-ion batteries requires the development of new electrode materials with higher charge capacities. On the anode side, silicon (Si) has attracted interest due to its high theoretical capacity of 3579 mAh g^{-1}, which is ten times higher than the conventional graphite used in commercial Li-ion batteries. However, practical application is limited because of poor cycling stability.

In this dissertation, the development of a Si-based anode which meets a rational design for a full cell configuration has been studied. The first approach has been the development of Si/mesoporous carbon (Si/MC) composites as an active material. Si/MC composites were synthesized by dispersing Si nanoparticles in a 3D Resorcinol-Formaldehyde (RF) polymer, followed by carbonization and HF etching. The second approach has been the selection of the proper commercial conductive additives to improve the electrical conductivity of Si/MC anodes. Graphite, Super C65, Super C45, and a combination of graphite and Super C65 were compared. The third approach for dealing with the initial capacity loss has been the use of electrolyte additives. The effect of three different electrolyte additives : vinyl carbonate (VC), succinic anhydride (SA), and lithium bis(oxalato)borate (LiBOB) on the electrochemical performance of Si/MC anodes were investigated.

The as-prepared Si-based anode by using a facile synthesis exhibited a discharge capacity of $\sim$> 800 mAhg^{-1} with average columbic efficiency of $\sim$99% over 400 cycles. Additionally, the as-prepared Si/MC anode was coupled with a commercial Li[Ni$_{1/3}$Mn$_{1/3}$Co$_{1/3}$]O$_2$ (NMC) cathode to see the limiting working potential in a full cell configuration.

"It always seems impossible until it is done." –Nelson Mandela

Table of Content

Table of Figures

Table of Tables

Abbreviations

BET	Brunauer-Emmett-Teller
BJH	Barrett–Joyner–Halenda
CB	Carbon black
CCCV	Constant-Current Constant-Voltage
CMC	Carboxyl methyl cellulose
CNT	Carbon nanotube
CV	Cyclic voltammetry
CVD	Chemical vapor deposition
CE	Coulumbic efficiency
DEC	Diethyl carbonate
DMC	Dimethyl carbonate
DWSiNT	Double-walled Si–SiOx nanotube
EC	Ethylene carbonate
EDAX	Energy dispersive x-ray spectroscopy
EIS	Electrochemical impedance spectroscopy
EMC	Ethyl methyl carbonate
FEC	Fluoroethylene carbonate
FIB	Focused ion beam
FWHM	Full width half at half maximum
FTIR	Fouries transform-Infrared spectroscopy
HEVs	Hybrid electric vehicles
HF	Hydrofluoric acid
HRTEM	High-resolution transmission electron microscopy
Na-CMC	Carboxymethylcellulose sodium
NMP	N-Methylpyrrolidine
OCV	Open circuit voltage
PAA	Polyacrylic acid
PC	Propylene carbonate
PE	Polyethylene
PP	Polypropylene
PHEVs	Plug-in hybrid electric vehicles
PVD	Pressure vapor deposition

RF	Resorcinol formaldehyde
SBR	Styrene-butadiene rubber
SEI	Solid electrolyte interphase
SEM	Scanning electron microscopy
SHE	Standard hydrogen electrode
SiNWs	Silicon nanowires
SiNPs	Silicon nanoparticles
SPE	Solid polymer electrolyte
TEM	Transmission electron microscope
TGA	Thermal gravimetric analysis
VC	Vinylene carbonate
XPS	X-ray photoelectron spectroscopy
XRD	X-ray diffraction

List of Symbols

V	voltage
μ	chemical potential
Q	capacity
C_C	capacity of cathode
C_A	capacity of anode
I	current
t	time
m	weight
M	molecular mass
F	Faraday's contant
x	number of electron
S	surface area
W	energy
P	power
σ_{Li}	Li-ion conductivity
σ_e	electron conductivity
S	siemens
f	frequency
ω	angular frequency
Z_{Re}	real axis
Z_{im}	imaginary axis
D	grain size
K	shape factor
λ	wavelength
d	spacing between layers of atoms
β	full width at half maximum (FWHM)
2θ	peak position at XRD pattern
Re	electrolyte resistance
Rct	charge–transfer resistance
Cdl	double-layer capacitance
W	Warburg impedance

P   partial vapour pressure

P_0 saturated pressure of adsorbate gas

V_a volume of gas adsorbed at standard temperature

V_M mole volume

A   plot slope of imaginary resistance (Z_{im}) vs. inverse square root of angular frequency $(1/\sqrt{2\omega f})$

Chapter I

Introduction

1.1   Motivation

Energy storage technologies play an important role in shifting the consumption of fossil fuels into renewable energy. Particularly, Li-ion batteries dominate the market of portable devices for their outstanding specific capacity and long lifespan. However, to fulfill current requirements, in particular for electrical vehicle application, further improvements are still required. The development of Li-ion batteries requires to consider not only their technical aspects such as energy capacity and rate capability, but also economic, environmental, and safety aspects.

Increasing the energy density of Li-ion batteries requires the development of new electrode materials with higher specific capacities. On the anode side, silicon has attracted interest due to its high theoretical capacity of 3579 mAh g^{-1}, which is ten times higher than that of the conventional graphite used in commercial Li-ion batteries today. However, practical application is limited because of poor cycling stability of Si anode. The large volume changes of Si anodes during lithiation/delithiation is a main shortcoming to be solved. They cause continuous loss of electrical contact between Si particles and current collector which leads to increasing internal resistance of the electrode. To improve the cycling stability of the electrode, continuous electrical conducting pathways and stable Solid-Electrolyte Interphases (SEI) are also required. Several strategies have been reported to reduce the volume change and improve the stability of silicon electrodes, either by using nanostructured particles, polymeric binders, conductive additives, or applying specific cycling conditions (pre-cycling, adjusted cut-off voltages, and current rates). However, despite these improvements, cycling performance of Si electrodes remains unsatisfactory for use in practical Li-ion batteries.

1.2   Research objectives

The main goal of this research was to design a Si-based anode which exhibits stable electrochemical performance discharge capacity of ~800 mAhg^{-1} over 400 cycles using a facile synthesis. This dissertation has the following aims and objectives;

1. To optimize the synthesis method of silicon/mesoporous (Si/MC) composites.

2. To improve the electronic conductivity of the as-prepared Si/MC electrodes.

3. To reduce the initial charge loss of the as-prepared Si/MC electrodes.

4. To assess the as-prepared Si/MC-based anode in a full cell configuration.

1.3   Methodological approaches

To meet aforementioned objectives, these following approaches have been done:

1. An in-depth investigation of the difference in physicochemical and electrochemical properties of Si/MC composites before and after HF etching.

2. A comparative study of commercial conductive additives (carbon black of Super C65, carbon black of Super C45, graphite, mixture of carbon black and graphite) for Si/MC elctrodes.

3. Modification of SEI layer by using electrolyte additives (VC with different composition, succinic anhydride, and lithium bis(oxalate)borate).

4. Coupling the Si/MC negative electrode with commercial $Li(Ni_{1/3}Co_{1/3}Mn_{1/3})O_2$ (NMC) positive electrode and testing the cell with charge-discharge tests.

1.4   Structure of the work

This dissertation will summarize the work focusing on the development of Si-based anodes. It is divided into five main chapters. Chapter one states the introduction describing the problem, the objectives of the research, the methodological approaches which have been conducted, and the structure of the dissertation.

Chapter two provides a general overview of Li-ion batteries; such as main component, general reactions during charge/discharge, and materials for positive and negative electrodes. The advantages and drawbacks of each materials are pointed out. Special attention is devoted to silicon-based negative electrodes and current approaches to improve their electrochemical performance.

Chapter three describes the experimental methods which have been applied, from the material preparation and characterization to electrochemical tests. In addition, the synthesis process of silicon/mesoporous carbon (Si/MC) composites is described. Material characterization has been done using XRD, SEM, TGA, and N_2 adsorption. Electrochemical tests used are cyclic voltammetry, charge/discharge test and electrochemical impedance spectroscopy.

Chapter four reports the experimental results and discussion. This chapter is divided in to five parts. First part focuses on the approach in optimizing the manufacture of the Si/MC composite by HF etching. The differences of structural, morphological and electrochemical properties of Si/MC before and after etching are explained. The second part is focused on the improvement of Si/MC electrode with the conductive additives. Three different conductive additives have been used : carbon black (Super C65 & Super C45) and graphite. The third part is focused on decreasing the initial charge loss of Si/MC by using electrolyte additives. The effect of 3-10 wt% vinyl carbonate (VC), 5 wt% succinic anhydride (SA), and 5 wt% lithium bis(oxalato)borate (LiBOB) was investigated. X-ray photon spectroscopy has been applied to understand the influence of electrolyte additives on the formation of the SEI-layer. The fourth part correlates the findings with the reported realistic design of Si/MC-based anodes. The fifth part shows the assembling of full cell compartments containing Si/MC anodes in combination with commercial $Li[Ni_{1/3}Mn_{1/3}Co_{1/3}]O_2$ (NMC) cathodes. Differential capacity (dQ/dV) and differential voltage (dV/dQ) analysis were applied to determine the cut-off voltage window for NMC/Si/MC full cell.

Chapter five summarizes the results and discussions regarding this work. The highlights of the findings will be pointed out.

Chapter II

Theoretical Background

2.1 Introduction into Li-ion batteries

Nowadays Li-ion batteries dominate the market of portable electronics and penetrate the market of transportations, such as hybrid electric vehicles (HEVs) and plug-in hybrid electric vehicles (PHEVs). Most investments are largely focused on Li-ion batteries, as they are forecasted as the most used system for at least 15 years. Figure 1 displays the energy density and power density comparison between different type of secondary batteries [1]. In spite of the tremendous success in the portable electronic market, Li-ion batteries still face great challenges for the transportation vehicle application. Many efforts have been done to improve the aspects of energy/power density, cycling life, safety and overall costs to compete with the internal combustion engine and fossil fuel energy.
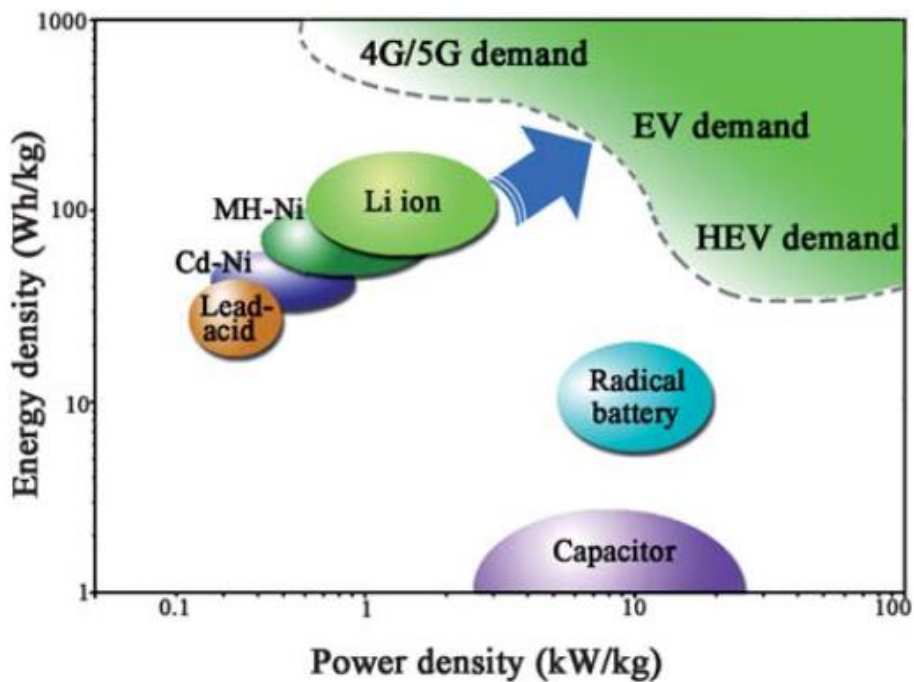
Figure 1. Schematic representation of the different secondary batteries in terms of power density and energy density [1].

2.2   Principle of Li-ion batteries

In 1991, Sony commercialized Li-ion battery with $LiCoO_2$ as positive electrode and graphite as negative electrode. The active materials are deposited on current collectors (copper for negative and aluminium for positive electrode). Both electrodes are separated by a separator   which contains the immersed liquid electrolyte. A separator made of a microporous polyethylene or polypropylene is used as physical barrier between the electrodes. In Li-ion batteries, like in all batteries the conversion of chemical energy into electrical energy is the result of two half-cell redox reactions. By definition, the electrode where a reduction takes place is the cathode, while the electrode where oxidation takes place is the anode. A schematic representation of the operating principle of a Li-ion battery can be seen in Figure 2. During charge, lithium ions are extracted from the positive electrode (oxidation) and intercalate into negative electrode (reduction). The lithium ions travel through the electrolyte while the electrons travel through external circuit to maintain the neutrality of the electrodes. During charge, these reactions are not spontaneous so an external power source is necessary. During discharge, the opposite redox reactions occur spontaneously.
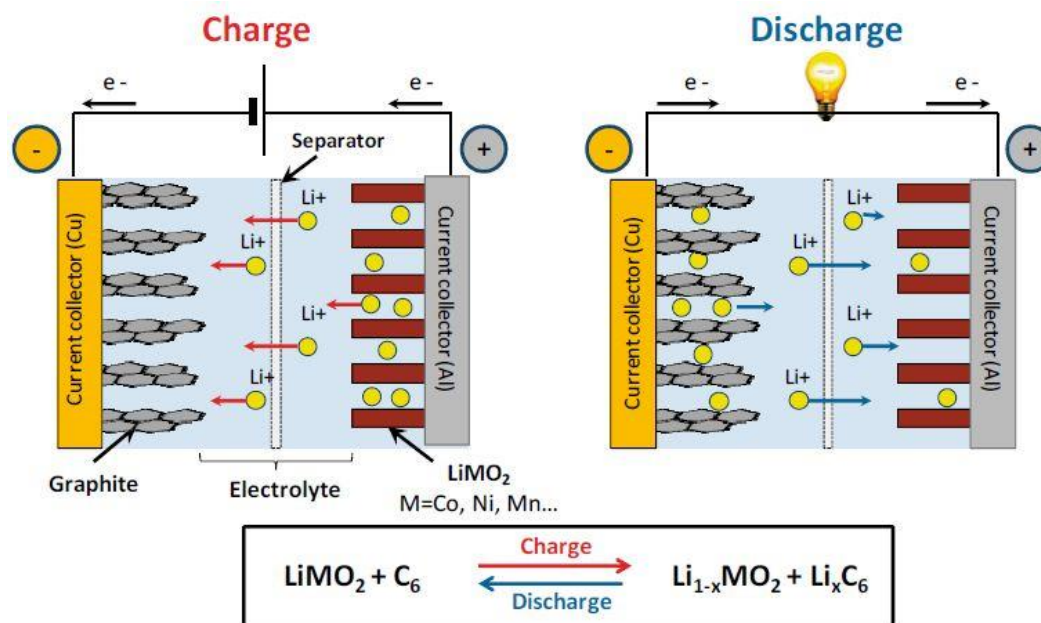
Figure 2. A schematic representation of the operating principle of a Li-ion battery [2].

2.3   Electrochemical evaluation of Li-ion battery performances.

The performance of the battery can be expressed by different parameters, as following :

- Cell voltage

The cell voltage (in volts) is defined as the potential difference between two electrodes :

$$V = \Delta\mu \qquad (1)$$

This voltage can refer to open circuit voltage (OCV) when there is no current applied or to specific load conditions (nominal voltage).

- Capacity

The capacity is a measure of the total amount of charge that can be stored in the battery. It is defined by the equation (2):

$$Q = \int_0^t I.\,dt \qquad (2)$$

Where I : the current (in Ampere)

t : the time while the current is delivered (in seconds)

Q : the capacity in Coulomb (C) or in Ampere-hours (Ah), (1 Ah = 3600 C)

The theoretical capacity of a material can be calculated from the number of electrons exchanged per formula unit of the host material (the number of Li^+ inserted per mole of active material using the equation (3):

$$Q\,(C) = \frac{m.F.\Delta x}{M} \quad or \quad Q\,(mAh) = \frac{m.F.\Delta x}{3.6\,M} \qquad (3)$$

Where m : weight of the active material (g)

F : Faraday's constant (96,485 C.mol^{-1})

Δx : number of electrons exchanged per formula unit of the host material (= number of Li^+ inserted in the host material)

M : molecular weight of the active material (g. mol^{-1})

The specific capacity is defined as the capacity per unit of weight of active material (gravimetric specific capacity in mAh.g^{-1}) or per unit of volume (volumetric specific capacity in mAh.dm^{-3}). For the areal capacity, the capacity is divided by the electrode area A (cm^2).

6

Practical capacity values are in principle lower than the theoretical values due to energy losses by side reactions, resistance etc. and depend on the charing and discharging conditions.

To normalize the battery specifications, C-rate is used to express the battery performance upon galvanostatic testing. C-rate is a measure of the time taken to deliver the full capacity of the battery. For example, C/n means the theoretical capacity C is delivered upon a discharge (or charge) of *n* hours.

- Energy

The energy of a battery is the measure of the amount of energy that the battery can deliver. It is defined by the equation (4):

$$W = U.I.t = U.Q \tag{4}$$

Where   U : the cell voltage (in Volt)

I : the current applied through battery (in Ampere)

Q : the capacity (in Coulomb or Ah)

T : the time while the current is delivered (in seconds)

The specific energy is expressed per unit of mass (in $Wh.g^{-1}$), the energy density per unit of volume (in $Wh.dm^{-3}$).

- Power

The power represents the ability of the battery how fast to deliver the lithium ions. It is defined as the energy per time unit and can be calculated by using the equation (5).

$$P = U.I \tag{5}$$

The value depends on the "internal resistance" of the battery, which is determined by the electronic and ionic conductivity and polarization. For the batteries, the specific power (W kg^{-1}) and the power density (W dm^{-3}) are generally used.

- Cyclability or cycle life

The cyclability corresponds to the number of charge/discharge cycles that can be carried out before a lower limit of the capacity is reached ($\sim 80\ \%$ of the initial capacity).

- Coulombic efficiency

The coulumbic efficiency (CE) reflects the contribution of side reactions and is defined as the ratio of the charge capacity over the discharge capacity (equation (6)). A battery should have the coulumbic efficiency as close as possible to 100% to be used in commercial application.

$$CE = \frac{Q_{charge}}{Q_{discharge}} \ x \ 100 \ \% \qquad (6)$$

- Capacity retention

The capacity retention (CR) can mathematically show the capacity fading in the battery. Capacity retention of the nth cycle is calculated by :

$$CR = \frac{Q_{discharge_n}}{Q_{discharge_{n-1}}} \ x \ 100\% \qquad (7)$$

2.4 Main drawbacks and challenges for Li-ion batteries

The progress in battery research is far from following Moore's law (doubling of the storage capacity in 18 months). Since the first commercial Li-ion batteries produced, approaches have been done on improving the system performance, increasing the safety, decreasing costs and improving the sustainability. Despite the breakthrough from nanomaterials, present Li-ion technology does not satisfy the requirements for large volume application, such as renewable energy and electric transportation fields. To satisfy the current needs, increasing their energy and power density are required. One effort to be done is improving the active materials for positive and negative electrodes. The materials should be capable to absorb much lithium, thus delivers a larger capacity. In addition, the anode and cathode materials should present a large electrochemical potential difference ($\sim$5V).

In addition, the structure and composition of the electrodes are determining the battery performance to a large extent. The choice of binder, conductive additives, and the internal structure have a strong impact on the global performance of a Li-ion batteries.

8

2.5 Materials for Li-ion batteries

The selection of the electrode materials for Li-ion batteries is based on intercalation compounds that can reversibly host lithium ions. For commercial Li-ion batteries, the positive electrode consists of a lithium containing transition metal oxide whereas the negative electrode uses carboneous materials. An overview of the investigated materials is presented in Figure 3. Most of the current and future promising materials for cathode and anode will be discussed further.
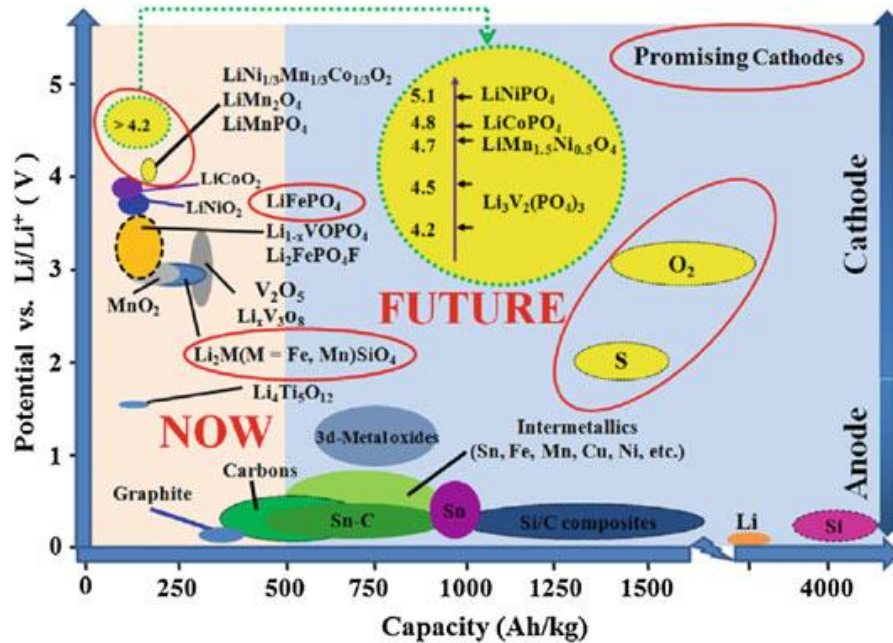
Figure 3. Potential vs. Li/Li+ and specific capacity of selected cathode and anode materials for Li-ion batteries [3].

2.6 Materials for positive electrodes

In Li-ion batteries, positive electrodes are referred as cathodes. They are typically intercalation compounds made of lithium metal oxides to provide lithium. The general formula of intercalation materials is $Li_xM_yX_z$, where M is a metal (usually transition metal), X is an anion (oxides or polyanions $(XO_4)^{n-}$). Whittingham reviewed that the material for positive electrodes has to fulfill following requirements [4]:

1) The material contains have a multi-steps valence change, for example a transition metal.

2) The material reacts reversibly with lithium and causes minimal structure changes during insertion/extraction of the lithium.

3) The material may host several Li-ions per formula unit which can deliver high capacity. The insertion/extraction process should operate at high voltage (around 4V vs. Li/Li^+).

4) The material should have a good electronic and Li-ion conductivity.

5) The material should be thermally and chemically stable, low cost and environmentally benign.

$LiCoO_2$ has been the standard electrode in commerial Li-ion batteries. However, $LiCoO_2$ cathode material is expensive due to the high cost of cobalt and thermally unstable at elevated temperature. Thus, several substitute cathode materials have been studied. The cathode materials used in Li-ion batteries can be classified into three categories :

- One-dimensional structure in which Li-ions are inserted into a single direction or via a first-order phase transition (for e.g : $LiFePO_4$). This type of reaction exhibits a flat potential profile.

- Two-dimensional structure referred as layered structure (for e.g : $LiCoO_2$, $LiNiO_2$, and $LiNi_{1/3}Mn_{1/3}Co_{1/3}O$). This type of reaction exhibits a sloping potential profile.

- Three dimensional structure in which Li-ions are inserted into a 3D framework (for e.g : $LiMn_2O_4$):

$LiFePO_4$ offers high safety and cycle life, but less energy. $LiMn_2O_4$ (LMO) costs less, but it delivers lower energy and degraded electrochemical performance at elevated temperature. While $LiNi_{1/3}Mn_{1/3}Co_{1/3}O$ (NMC) offers lower cost, high energy density, and higher safety compared to $LiCoO_2$. Thus, NMC is a promising cathode material in Li-ion batteries for electrical vehicle application.

2.7 Materials for negative electrodes

The negative electrodes are referred as anodes. Metallic lithium was firstly used as negative electrode. However, the use of metallic lithium causes the formation of dendrites upon cycling leading to loss of capacity and safety problems. Therefore, the metallic lithium was replaced by a lithium intercalation compound which has a electrochemical potential close to that of lithium metal [5]. The materials for negative electrode should have to fulfill the following requirements :

1) The material reacts reversibly with lithium.

2) The material accommodates several Li-ions per metallic atom to provide high capacity.

3) Insertion/extraction processes should operate at a low potential close to Li/Li$^+$ (-3.04V vs. SHE) to obtain a wide cell voltage window.

4) The material should have a good electronic and Li-ion conductivity.

5) The material should be low cost and environmentally benign.

There are three types of reaction involved at the negative electrode of batteries ; (1) insertion/intercalation, (2) alloying/dealloying, (3) conversion.

Commercial Li-ion batteries currently use carbonaceous materials. Yazami et al. were the first to use graphite in an electrochemical cell [6]. Graphite consists of graphene sheets stacked in ABAB (hexagonal) or ABCABC (rhomboedral) patterns. Lithium can be reversibly intercalated between these sheets. At room temperature, one lithium reacts with six atoms of carbon giving a theoretical capacity of 372 mAhg^{-1}.

$$Li^+ + e^{-1} + 6C \rightarrow LiC_6 \qquad\qquad [\,i\,]$$
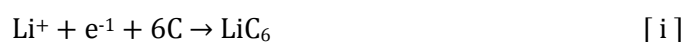
In addition, graphite is used also because it has a low insertion voltage ($\sim$ 0.2 – 0.05 V vs. Li/Li$^+$). It has good reversibility as the volume expansion is $\sim$ 10%.

The second type of the negative electrodes is metals and semi metals which react with lithium. The electrochemical formation of alloys between lithium and a metal can be explained by following general equation [ii]:

$$M + xLi^+ + xe^- \rightarrow Li_xM \qquad\qquad [\,ii\,]$$

Alloying elements are mainly in group 13 (Al, Ga, In), 14 (Si, Ge, Sn, Pb), and 15 (As, Sb, Bi) of the periodic table. Alloys generally provide higher volumetric and gravimetric capacities than the insertion materials (graphite, Li$_4$Ti$_5$O$_{12}$, etc). However, these materials suffer from volume expansion upon cycling. The volume expansion can destroy the electrode structure leading to the contact loss between active material, the current collector, and the conductive material [7].

The third type of materials investigated as candidates for the negative electrode in Li-ion batteries are conversion materials. They contain a transition metal coupled with an anion. The conversion reaction takes place during lithiation following general question [iii]:

11

$$M_yX + nLi^+ + ne^- \leftrightarrow yM + Li_nX \qquad\qquad [\text{ iii }]$$
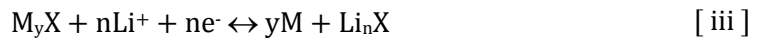
Where M = transition metal, X = anion, and n = formal oxidation of X.

The conversion reaction involves the complete reduction of the transition metal to the metallic state. When Li is removed from the structure, the M_yX phase is transformed into a nanosized phase that is maintained upon further cycles. Most of the 3d transition metals belong to this type such as Co, Cu, Fe.

2.8   Electrolyte

2.8.1   Requirement of electrolytes

The electrolyte should ensure sufficient charge transport by high ionic conductivity and fast (mass-) transport of the lithium ions. In general, electrolytes for Li-ion batteries should have these requirements:

- Large electrochemical potential window

- A Li^+-ion conductivity $\sigma_{Li} > 10^{-4}$ S cm^{-1} over the temperature range of battery operation

- An electronic conductivity $\sigma_e < 10^{-10}$ S cm^{-1}

- A transference number $\sigma_{Li}/\sigma_{total} \approx 1$, where σ_{total} is $\sigma_{Li} + \sigma_e$

- Chemical stability over ambient temperature ranges and temperatures in the battery under high power (25 – 160°C)

- Chemical stability with respect to the electrodes, in order to prevent corrosion of both electrodes and current collector

- Preferably nonflammable and nonexplosive if there is a short-circuit

- Low toxicity and low cost

In addition, immobilized electrolytes or separators should provide a physical barrier between the negative and positive electrodes in order to prevent electrical or chemical short circuits. Immobilized electrolytes can be formed in two ways. First, adsorbed electrolyte which is fabricated from microglass fibers and partially filled with electrolyte. Second, gelled electrolyte in which fumed silica is added to the electrolyte causing it harden into a gel [8].

2.8.2   Types of electrolytes

In Li-ion batteries, liquid electrolytes are mostly used. They are mainly composed of a lithium salt dissolved in mixtures of organic solvents (for e.g : carbonates) [9]. Most carbonates exhibit a large electrochemical window and undergo electrochemical oxidation at a potential of 4.7 V vs. Li/Li$^+$. Cathodic reduction proceeds at potentials near 1 V vs. Li/Li$^+$ [9], [10]. In addition, their viscosity is relatively low, which results in a high diffusivity for lithium ion diffusion. Therefore, carbonates or carbonate blends are the most commonly used electrolytes for Li-ion batteries. They consist of one or more of the following compounds : propylene carbonate (PC), ethylene carbonate (EC), diethyl carbonate (DEC), dimethyl carbonate (DMC), ethylmethyl carbonate (EMC). For graphite anodes, EC is preferably used because (1) it forms a passivating SEI layer on the anode surface that protects the electrolyte from further decomposition after initial SEI formation [11], (2) its high polarity favors salt dissociation for high ionic conductivity.

The preferred salt for Li-ion batteries, lithium hexafluorophosphate (LiPF$_6$), is used because (1) its high ionic conductivity (~10 mS cm^{-1} at room temperature) due to the low charge density of the complex anion, (2) it is stable over a wide electrochemical window, (3) it participates in the formation of a stable SEI on the graphite surface and (4) it passivates Al current collector at high potentials. Lithium bis(oxalato)borate (LiBOB) and lithium difluoro(oxalate)borate (LiDFOB) also form favorable SEI at graphite anode. However, these two salts are not stable > 4V vs. Li/Li$^+$ due to oxidation of oxalate and have lower ionic conductivity in comparison to LiPF$_6$. Meanwhile, lithium bisfluorosulfonyl imide (LiSFI) exhibits higher ionic conductivity than LiPF$_6$ and forms stable SEI. However, it does not passivate the Al current collector at high potential (3.3 V vs. Li/Li$^+$) [12]. Therefore, LiBOB, LiDFOB, and LiSFI can not replace LiPF$_6$ as single salt, but can be used as an additive or a co-salt in combination with LiPF$_6$.

Another type of electrolyte used is solid polymer electrolyte (SPE) which consists of lithium salts incorporated into a polymer. It can act additionally as a separator between the electrodes. However, the high cost and low ionic conductivity make them unsuitable for the large size Li-ion batteries to be used in the transportation vehicles. Meanwhile, gel polymer electrolyte compromises the liquid electrolyte and solid polymer electrolyte. However, it suffers loss of the mechanical strength at elevated temperatures.

2.8.3 Solid Electrolyte Interphase (SEI)

2.8.3.1 SEI models

During the first lithium insertion into the negative electrode host, lithium reacts and decomposes the electrolyte. Thus, forming a passivation layer on the surface of the electrode, so-called Solid Electrolyte Interphase (SEI). SEI on anode surface is the key to control the power and cycle performance of lithium ion battery. When the SEI reaches a critical thickness, the electrolyte no longer decomposes and stops further reduction. The typical SEI thicknesses ranges from ~20 Å to several hundreds of Å [13]. The performance of a battery upon long-term cycling is strongly related to the properties of SEI (composition, thickness, morphology, density).

An "ideal" SEI should meet several requirements :

- Very low electronic conductivity (t_{e-} ~ 0)

- High ionic conductivity (t_{Li+} ~ 1)

- Uniform and stable composition

- Good adhesion to the electrode materials

- Good flexibility and mechanical properties to accommodate the volume expansion of the active materials

- Low solubility in the electrolyte to avoid further electrolyte degradation

Several factors that affect the SEI properties are the electrolyte composition (solvent, salt, additives), the nature of electrode materials (active material and binder), the electrochemical cycling conditions (charge- and discharge rate, depth of discharge, etc), and the operating temperature [14].

2.8.3.2 SEI composition

The composition of SEI is complex and still discussed in the literature. A recent study described that the SEI consists of a dense layer of inorganic compounds which forms a protective layer towards reduction. The SEI layer is the product of electrolyte decomposition which may contain Li_2CO_3, lithium alkyl carbonate, lithium alkyloxide, and residues of an LiF- or $LiPF_6$-based electrolyte [15]. Figure 4 illustrates the composition of SEI layer on graphite anode [16]. Two mechanisms have been proposed for the electrochemical reduction of carbonate-based solvents [17]. The first stage takes place

14

before the intercalation of lithium ions into graphite. The SEI formed in this stage is structurally porous, higly resistive, dimensionally unstable and enriched with inorganic components. The second stage occurs simultaneously with the intercalation of lithium ions. The SEI formed is more compact, highly conductive, and enriched with the organic compounds. When the reduction mechanism of solvents generates more gas, the product contains more Li_2CO_3 and SEI layer is less stable. On the contrary, when the reaction generates less gas, the resulting products are insoluble in the electrolyte, and the SEI layer is compact and stable. The effect of nonaqueous electrolytes and additives on the performance of Si anodes is mainly adopted from electrolytes from graphite-based Li-ion batteries (i.e $LiPF_6$ in mixtures of ethylene carbonate (EC) and dimethyl carbonate (DMC).
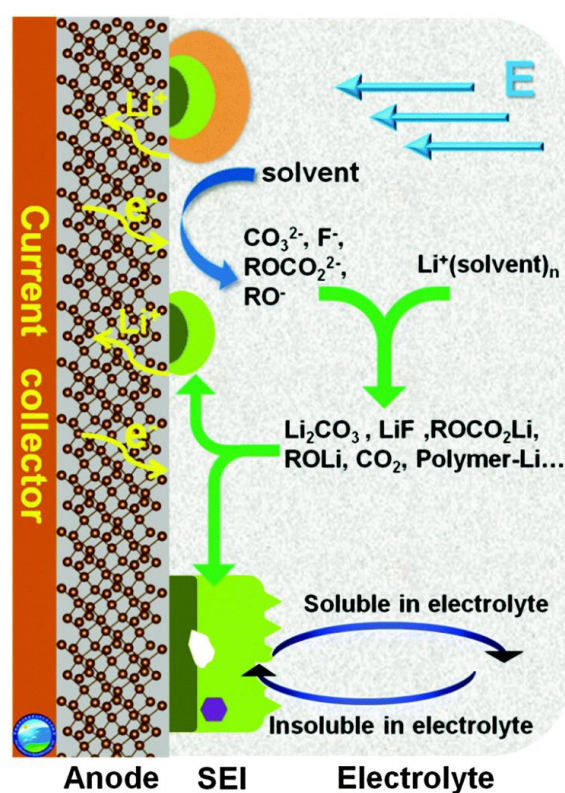
Figure 4. Scheme of SEI layer [16].

2.9   Separator

Separator physically isolates the cathode and the anode to prevent the electrical and physical contact of the electrodes. The separator does not participate actively in electrochemical reactions, but it strongly contributes to the battery safety. Separators used in the Li-ion batteries are typically a microporous polyethylene (PE) or polypropylene (PP) membrane. A trilayer separator which consists of PP-PE-PP is also used for their safety feature. The safety feature is based on the different melting temperature ranges between PE

(120-130°C) and PP (>165°C). When the battery operation reaches the melting temperature range of PE, the PE layer melts and closes its pores to shut down the current. Whereas PP remains to isolate the electrodes. Since the pore closing is irreversible, the battery will be damaged permanently once the thermal shutdown occurs.

2.10 Silicon based anode for Li-ion batteries

Based on Figure 3, Si is an attractive candidate of alloying elements since it presents the highest theoretical charge capacity (3579 mAh g^{-1} at room temperature), which is ten times higher than the conventional graphite electrode used for commercial application (372 mAh g^{-1} at room temperature). This is due to capability of one mol Si to host up to 3.75 mol of lithium [18]. Table 1 compares the properties of graphite and silicon as anode for Li-ion batteries.

Table 1. Comparison of Si and graphite as anode for Li-ion batteries [19].

Anode material	C	Si
Density (g.cm^{-3})	2.25	2.33
Lithiated phase	LiC_6	$Li_{15}Si_4$
Theoretical specific capacity (mAh g^{-1})	372	3579[a]
Theoretical volumetric capacity (mAh cm^{-3})	837	8339
Volume change (%)	12	>280
Potential versus Li (V)	0.05	0.4
Conductivity (S.cm^{-1})	0.61×10^3	2.52×10^{-6}

[a] The theoretical specific capacity of Si is based on $Li_{15}Si_4$.

2.10.1 Li-Si alloy

Huggins et al. showed that during the lithiation of Si at high temperature (415 °C), four distinct voltage plateaus appear corresponding to $Li_{12}Si_7$, Li_7Si_3, $Li_{13}Si_4$, and $Li_{22}Si_5$ [20]. The formation of the highly lithiated phase $Li_{22}Si_5$ ($Li_{4.4}Si$) gives a theoretical capacity of ~4200 mAh g^{-1}. However, the lithiation of Si at room temperature occured differently. Limthongkul et al. showed that continual lithiation took place since the first discharge around 0.1V vs. Li/Li$^+$. The crystalline Si particles were converted into $Li_{15}Si_4$ ($Li_{3.75}Si$) [21]. They also showed that this process leaded to partial destruction of the Si crystal lattice forming amorphous Li_xSi phase [22].

16

2.10.2 Main challenges of Si anode

Chan et al. [23] and Ji et al. [24] confirmed that anodes made of pure crystalline Si suffered from poor capacity preservation. By using scanning electron microscopy (SEM) and high-resolution transmission electron microscopy (HRTEM), Chon [25] and Liu [26] reported that crystalline-amorphous phase transformation during the initial lithiation induces high compressive stress of ca. 0.5 GPa. By using ex-situ and in-situ X-ray diffraction (XRD), Obrovac et al. [27] and Hatchard et al. [28] investigated that a $Li_{15}Si_4$-phase was formed at ~50 mV vs. Li/Li$^+$. Due to a large internal resistance, the dealloying reaction is not completed while Si remains in a lithiated state.

To summarize, three fundamental challenges of Si-based anode can be outlined, as illustrated on Figure 5 [29]. First, the extreme volume change over 280% during lithium insertion/extraction induces the large stress of Si (Figure 5a). Second, the drastic change of electrode morphology will cause capacity loss (Figure 5b). Third, the low stability of the solid electrolyte interphase (SEI) layer on Si anode weakens the electrical contact and elongates the Li$^+$ ion diffusion path, as illustrated in (Figure 5c) [30]. SEI is a layer from the decomposition product of the organic electrolyte below ~1 V vs. Li/Li$^+$ which passivates the electrode surface. Verma et al. confirmed the formation of this passivating SEI film on the Si surface by HRTEM, Fourier Transform Infrared Spectroscopy (FTIR), and X-ray Photoelectron Spectroscopy (XPS) [14].
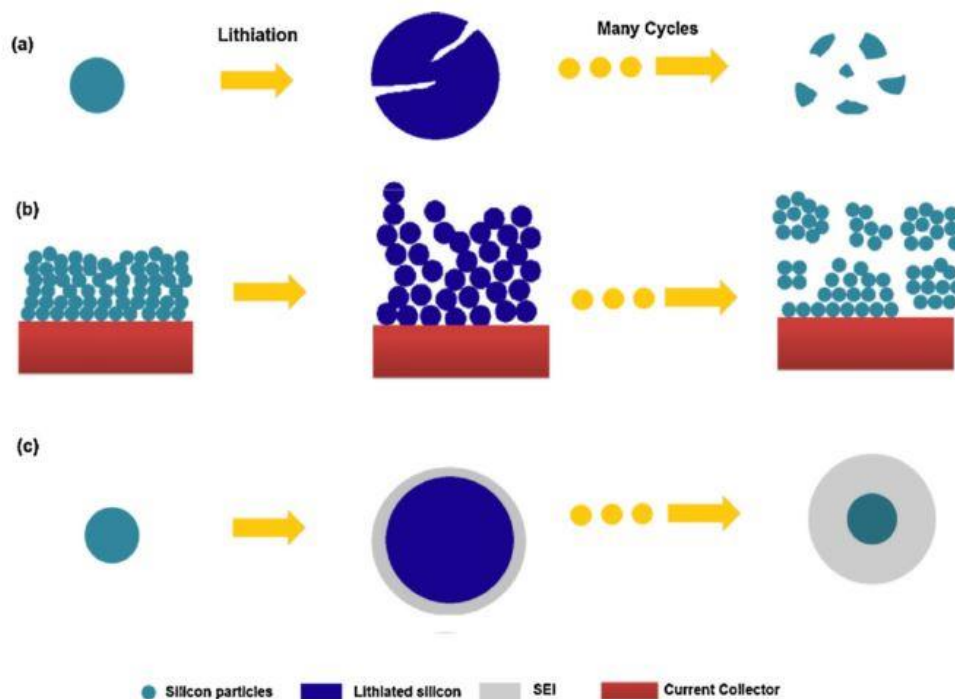
Figure 5. Si electrode failure mechanisms: (a) material pulverization, (b) morphology and volume change of the entire Si electrode, (c) continuous SEI growth [29].

2.10.3 Improvement of the Si-based electrode materials

2.10.3.1 Limitation of the capacity

Several strategies have been followed to improve Si-based anodes including the limitation of the capacity for reducing the degradation caused by volume expansion. Because of the close (causal) relationship between the Li-insertion and volume expansion, limiting the amount of lithium inserted in the host material will limit also the volume expansion. The capacity can be limited experimentally by controlling the voltage (lower cut-off voltage) [31]. Jung et al. showed that lowering the voltage limit from 0 to 0.2V reduced the capacity fading, however the capacity was limited to 400 mAh g^{-1} [32]. Therefore, the voltage window needs to be adjusted. Li et al. proposed the lower limit voltage to 70 mV [33]. Obrovac for the first time proposed a constant-current/constant-voltage (CCCV) procedure to reversibly cycle crystalline Si particles [34]. This method includes two steps: first, the particles are partially lihiated and converted into a desired amount of amorphous silicon, and then the electrode is cycled with a lower cut off voltage of 170 mV to avoid over-lithiation and to maintain the crystalline core.

2.10.3.2 Modification of the Si morphologies

Stress induced by volume expansion is the main reason for capacity fading of Si-based anode. Therefore, the initial morphology of Si plays an important role in determining the capacity and cyclability. Since 1996, the transition from large particles to micro-particles has shown to improve the cycling performance of alloy-materials [35]. Lately, many problems associated with electrochemical alloying have been mitigated with nanostructured Si. Their small dimension and high surface area allow nanostructured Si particles to accommodate the lithium with minimal internal stress. Moreover, their shorter distance of electronic and ionic transport may facilitate Li-ion diffusion and electron transfer leading to better electrochemical performances [36]. In the past decade, various structural designs of nanostructured Si materials have been investigated in attempt to improve the Si-based anodes, such as Si nanoparticles, Si nanoporous, Si nanowires, Si nanotubes, and Si thin films.

2.10.3.3 Si Nanoparticles (SiNPs)

In 1999, Li et al. firstly reported that SiNPs with ~78 nm size demonstrated greater improvement than bulk Si [37]. This improvement was attributed to the smaller volume variation of single nanometer alloy particles compared to single large size alloy particles during cycles [38]. Besides, nanosized materials often have higher plasticity and deformability which prevent the crack and pulverization of the electrode [39]. Liu et al. reported that the critical diameter of Si particle without fracture during lithiation was ~150 nm [40]. Due to their advantages, SiNPs offer their great potential to fabricate Li-ion batteries anodes. In addition, synthesis methods for SiNPs are rather mature. SiNPs are already commercially available [41]. However, SiNPs have the drawback to maintain not sufficiently the electrical connection to the current collector [42]. Recent strategy deals with the utilization of conductive additives and of selected binders that keep the integrity of the electrode.

2.10.3.4 Si Nanowires (SiNWs)

Silicon nanowires have recently received much attention for application as Li-ion batteries anode due to sufficient internal space for large volume changes, robust electrical contacts between individual wires and the substrate and high resistance against fracture formation [29]. The pioneering work of using SiNWs as anodes of Li-ion batteries was done by Cui's group in 2007 using the vapour–liquid–solid (VLS) process on stainless steel substrates using Au catalyst [23]. SiNW electrode maintained a discharge capacity close to 75% of the theoretical charge capacity but a low cycle life (10 cycles). For SiNW, the diameter plays a important role for their mechanical properties during cycling. Ryu et al. confirmed the exact

"critical diameter" of SiNWs $\approx$ 300 nm by both theoretical calculation and ex situ TEM observation [43]. This finding brings a significant improvement in selecting appropriate methods for fabrication of SiNWs with suitable diameters for electrodes. The use of SiNWs has a great impact on the design of Si anode materials. However, their use in the near term is unlikely because of the high synthesis costs and the presence of impurities and toxic compounds.

2.10.3.5 Si Nanotubes (SiNTs)

Among various Si nanostructures, SiNTs show great promise because their structure can potentially undergo reversible morphological change during lithiation/de-lithiation [44]. Compared to SiNWs, the maximum stress in SiNTs is much lower due to the additional free inner surface possessed by tubular structures. Park et al. for the first time prepared SiNTs for Li-ion batteries anode by reductive decomposition of a Si precursor in an alumina template and etching [45]. These SiNTs showed high reversible charge capacity of 3247 mAh g^{-1} with coulombic efficiency of 89% at 5C rate. Similarly, Wu et al. designed a double-walled Si–SiOx nanotube (DWSiNT) anode using electrospun nanofibre templating method, in which the inner wall is active silicon and the outer wall is confining SiO_x [30]. DWSiNT anode demonstrated long cycle life (6,000 cycles with 88% capacity retention) with high specific charge capacity (2,971/1,780 mAh g^{-1} at C/5, 940/600 mAh g^{-1} at 12C). The extremely long cycle life of DWSiNT anode was attributed to the formation of stable SEI films associated with the unique double walled structure. These results are considered to be the highest specific capacity values among nanostructured Si anodes. However, fabrication of SiNTs are often complicated and high-cost, which makes them difficult to be implemented in practical battery applications.

2.10.3.6 Si Thin Film

As Si thin film anodes do not contain binders and conductive additives, they may offer higher specific capacity [31]. The important properties of the Si thin films are the thickness, surface morphology, crystallinity, and the bonding between the Si films and the current collector. Two common techniques to synthesize Si thin film are physical vapor deposition (PVD) [46] and chemical vapor deposition (CVD) [47]. For Li-ion batteries applications, the Si thin film is deposited directly on the current collectors, which can be Cu, stainless steel, Ni, or Ti metals. The improved electrochemical performance of Si thin film anodes was attributed to its small dimensions which permit the micromechanical processes of deformation and fracture. Therefore, they are well suited for micro-battery applications.

2.10.3.7 Si Nanoporous

A structure of nanoporous Si is considered as a promising solution by providing enough free space for expansion during lithiation. Nanoporous Si can be prepared in a scalable process using a novel two-step approach combining controlled boron doping and electroless etching [48]. Zhu et al. fabricated Si nanoporous by a scalable electrochemical process in which Si wafers were transferred to flexible and conductive substrates [49]. In spite of porous Si nanoparticles can improve the cycling performance of the electrode, they will reduce the volumetric capacity of the electrode. Most of the 3D porous silicon particles can be synthesized by HF etching process [50], chemical etching (HF/H_2O_2) [51], and electrochemical etching [52].

2.10.4 Synthesis of nanoporous Si

Cho et al. prepared three dimensional nanoporous (3DNP) Si by depositing Si particles on SiO_2 nanoporous templates [53]. This electrode exhibited a high specific capacity > 2800 mAhg^{-1} without significant degradation up to 100 cycles. Despite such promising performance of porous Si-based electrodes, their preparation required several complicated steps, such as fabricating a template, depositing a thin film etc. This makes the preparation expensive, slow, and difficult to scale up. Thakur et al. prepared two dimensional porous Si particles by electrochemical etching of Si wafers in a HF-based solution, followed by sonicating [54]. The Si anode showed an excellent retention capacity of 1000 mAh g^{-1} for over 600 cycles. Park et al. for the first time reported SiNPs in ordered mesoporous carbon (OMC) with a scalable process [55]. The Si/OMC composite was synthesized by a self-assembly procedure using Pluronic F127, a resorcinol–formaldehyde polymer and SiNPs. The electrode showed a reversible capacity above 700 mA h g^{-1} for 50 cycles. Recently, Xu et al. fabricated mesoporous C/Si composite via a similar method. The mesoporous C/Si composite anodes retained a capacity of 1018 mAh g^{-1} at a constant current density of 1000 mA g^{-1} for 100 charge/discharge cycles [56].

2.10.5 Conductive additives for Si-based anodes

To improve the cycling stability of the Si anodes with respect to their internal resistance, continuous electrical conducting pathways are required. Conductive additive plays an important role to improve the conductive percolation network of the Si-based anodes as undoped silicon basically has a low conductivity (2.52. 10^{-6} S cm^{-1}) [57]. Si particles coated with different conducting materials via different techniques have been studied. Carbon nanomaterials are considered as proper conductive additives for Si anodes for several reasons. First, they can accommodate the volume expansion of Si anode [57]. Second, they have high electrical conductivity (1.25 x 10^3 – 3 x 10^5 S m^{-1}) [58]. Third, they can stabilize

the SEI layer [59]. Amorphous carbon, graphite, graphene, carbon fiber, carbon nanotubes, have been studied as conductive additives for Si anodes. Table 2 summarizes the most recent literature data on Si electrodes combined with carboneous material for lithium-ion battery devices.

Table 2. Electrochemical performance of Si/C composites anodes for lithium-ion batteries.

Anode	Cycling stability	Synthesis method
n-Si/C	Reversible capacity of 500 $mAhg^{-1}$ using constant currents of 3.7 mA g^{-1}	CVD [60]
Si/C	Reversible capacity of 1066 $mAhg^{-1}$ with current density 0.05 mA cm^{-2}	mechanical milling [61]
n-Si/amorphous C	capacity retention 84% after 30 cycles at rate of 0.2C	butyl-capped Si annealing [62]
Si/OMC	700 mAh g^{-1} for 50 cycles at rate of 1C	self-assembly using Pluronic F127, resorcinol–formaldehyde polymer and Si nanoparticles [55]
Si/CB	1590 $mAhg^{-1}$ and 870 $mAhg^{-1}$ at rates of rates of 1C and 8C, respectively	CVD [63]
C/Si/C	reversible capacity of 2000 $mAhg^{-1}$ at 50 mAg^{-1}, and 100% capacity retention at 500 mAg^{-1} after 300 cycles	self-rolling technique [64]
SiNW/C	2000 $mAhg^{-1}$ for 100 cycles at C/10 and over 1200 mA h g^{-1} at 1C	supercritical fluid-liquid-solid (SFLS) [65]
SiNP- graphene	storage capacity >2200 mAh g^{-1} after 50 cycles and >1500 mAh g^{-1} after 200 cycles at rate of 100 mA g^{-1}	dispersing SiNPs between graphene sheets [66]
Si- graphene composite	reversible capacity of 1300 mAh g^{-1} (the charge rates from 100 mA g^{-1})	sonochemical method and magnesiothermic reduction [67]
Si–graphene	The capacity retention of 90% after 500 cycles and an average coulombic efficiency in excess of 99.5% at C/5	CVD [68]
G/Si–C	specific capacity of 3.2 mAh cm^{-2} after 100 cycles with coulombic efficiency 99.51%	dispersing SiNPs in Graphite Oxide [69]

Si- graphene composite	specific capacity of 1000 mAh g^{-1} at current density of 1000 mA g^{-1}	solvent exchange method [70]
porous SiNWs/graphene	specific capacity of 2041 mAh g^{-1} at the 20th cycle.	liquid-phase graphite exfoliation method and an electroless HF/AgNO$_3$ etching process [71]
Si-CNT	de-alloying capacity of ~480mAh g^{-1} at C/5 for 150 cycles	vapor deposition routes [72]
Multiwalled Carbon Nano Tube (MWCNT)-embedded SiNP	1510 mAh g^{-1} at a current density of 840 mA g^{-1} for 100 cycles	CVD and spin coating process [73]
VA-CNTs/Si	rate capability of 1900 mAh g^{-1} at 5C and 760 mAh g^{-1} at 15C	two-step CVD process [74]
C-Si core-shell NWs	specific capacity of ~2000 mAhg^{-1} and coulombic efficiency of 98-99.6% at the rate of C/5 over 30 cycles	CVD of a-Si on CNT films [75]
SiNPs-CNF	specific capacity of 2500 mAhg^{-1} at a current density of 500 mA g^{-1} over 50 cycles	pyrolysis [76]
Silicon- vertically aligned carbon nanofibers (Si-VACNF)	3000 to 3650 mAh g^{-1} at the C/10 and 89% of the capacity was retained after 100 cycles at the 1 C rate	magnetron sputtering [77]

Besides carboneous material, Yao et al. prepared a core-shell TiC/C/Si, in which the inactive TiC/C nanofibers acted as a conductive additive [78]. The TiC/C/Si nanocomposite anode showed ~3000 mAh g^{-1} discharge capacity and 92% capacity retention after 100 cycles.

In order to sum up, the addition of a conductive additive can enhance the electrochemical property of Si anodes. However, the amount of conductive additives should be compromised as it reduces the volumetric and gravimetric capacity of Li-ion batteries.

2.11 Binder for Si-based anode

For powder-based Si anodes, the type of binder has a major impact on cycle life as it maintains the electrode`s intregity. The performance of a polymer binder depends on at least four parameters : (i) adhesion strength between the electrode and the current

collector, (ii) interface between the polymer and the active material, (iii) interaction of the binder with the electrolyte, and (iv) the binder`s mechanical properties [79].

Polyvinylidene Fluoride (PVdF), a conventional binder, exhibits a good elastic properties for graphite anodes. However, it suffers from fast capacity fading in Si anodes due to its poor elastomeric property [80]. Significant improvement of cycle performance was found using styrene butadiene rubber (SBR) or binders containing carboxyl groups such as carboxymethyl cellulose (CMC), carboxymethylcellulose sodium (Na-CMC), polyacrylic acid (PAA), and alginic acid (alginate). The molecular structures of those polymer binders are presented in Figure 6. Most of these binders improve adhesion forces between their carboxyl groups and the hydroxyl groups on the Si surface. In addition, they have less interaction with electrolyte solvent.
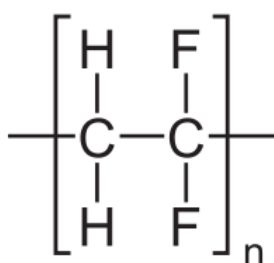
(a) Polyvinylidene Fluoride (PVdF)
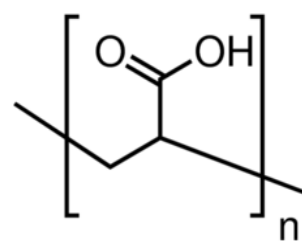
(b) Polyacrylic Acid (PA)
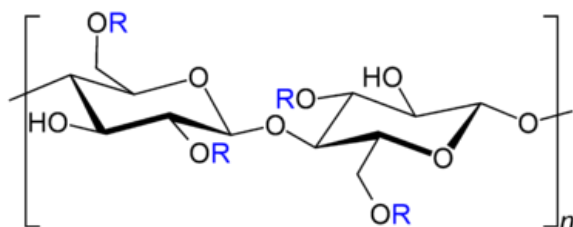
(c) Carboxymethyl Cellulose (CMC)

(d) Carboxymethylcellulose sodium (Na-CMC)
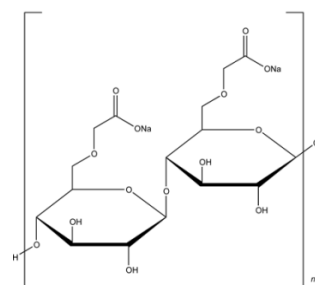
(e) Styrene Butadiene Rubber (SBR)   (f) Alginic Acid (Alginate)
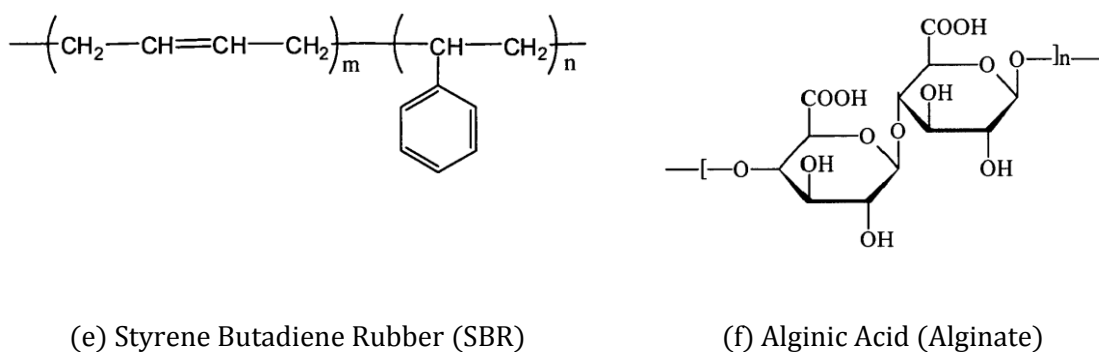
Figure 6. Molecular structures of polymer binders used for Si-anode materials: (a) Polyvinylidene Fluoride (PVdF), (b) Polyacrylic Acid (PAA), (c) Carboxymethyl Cellulose (CMC), (e) Styrene Butadiene Rubber (SBR), (f) Alginic Acid (Alginate).

Li et al. showed that CMC is a good binder which improves the stability of the Li-Si alloy [81]. The hydrogen bonding between the carboxymethyl groups in CMC and the Si surface can accommodate the strong volumetric modification during cycling. Later they also investigated the advantage of combining SBR and Na-CMC for Si anodes which showed an even improved stability with significantly lower amounts compared to bare CMC [82]. The second advantage is the solubility of SBR in ethyl acetate and Na-CMC in water, instead of more harmful organic solvents. However, aqueous solvents can increase surface oxidation of Si, thus affecting the coulombic efficiency and long-term stability of the anode. Besides, the mechanical properties of Na-CMC can not be adjusted by chemical modification for optimal use for Si anodes. Another binder, pure PAA, offers superior performance as a binder for Si anodes. Magasinski et al. reported for the first time that pure PAA showed mechanical properties comparable to those of CMC [79]. PAA contains a higher concentration of carboxylic functional groups than that of CMC. In addition, another study showed that PAA binder had less interaction with electrolyte solvents compared to PVdF which allowed the formation of a stable SEI [83]. Recently, Murase et al. examined binders based on biomaterials, in particular polysaccharides (amylose, amylopectin, and glycogen) for Si-based electrodes [84]. Similarly, Kovalenko et al. studied alginate, a natural polysaccharide extracted from brown algae, which yields a stable Si nanoparticles anode [85]. Alginate macromolecules which are much more polar than the CMC polymer chains can ensure better interfacial interaction between the polymer binder and the particles. They also provide stronger adhesion between the electrode layer and Cu substrate.

In summary, polymer binders for Si anodes should have unique properties, such as sufficient binding to the active material, adhesion to current collectors, insolubility in electrolyte solutions, high melting points, and chemical/electrochemical stability over a wide potential

range. All the binders described above are considered as polymeric and non-conductive. Conventional approaches for maintaining the electrical and mechanical integrity of powder based Si electrode can be done by adding conductive additives combined with polymer binders.

2.12 Electrolyte additives

Electrolyte additives can improve Li-ion batteries effectively. By using no more than 5% either by weight or by volume of the electrolyte, they improve the cyclability of Li-ion batteries. There are numbers of electrolyte additives for Li-ion batteries. The additives are selected to be able to : 1) stabilize the SEI layer, 2) reduce irreversible capacity loss caused by SEI formation during the first cycle, 3) enhance thermal stability of the electrolyte [86].

For Si anodes, vinyl carbonate (VC) [24], [87]–[92], fluoroethylene carbonate (FEC) [87], [88], [93], lithium bis(oxalato)borate (LiBOB) [87], [94], lithium difluorooxalatoborate (LiDFOB) [87], lithium bis(oxalato)borate [87], succinic anhydride (SA) [95], [96], and tris(pentafluorophenyl)borane (TPFFPB) [97], have been studied. The structure of each addtive can be seen in Figure 8.

VC can reduce effectively the irreversible capacity loss and enhances the stability of the SEI layer. XPS studies showed that the addition of VC results the formation of poly(VC) on the electrode surface which makes SEI denser and more stretchable [90]. However, excess VC decreases the cells cycling efficiency and promotes self discharge, so the amount should be compromised.

FEC forms a favorable SEI on the surface of Si anodes [87], [88], [93]. There are two possible mechanisms of FEC reduction proposed in the literature. First, FEC converts into VC through defluorination following the reaction in Figure 7. The resulting VC polymerizes, while HF effectively improves the cycleability of metallic lithium. The main products are LiF and poly(vinylene carbonate). Second, FEC is reduced through opening the five-membered ring to form a $(CH_2CHFOCO_2Li)_2$ dimer.
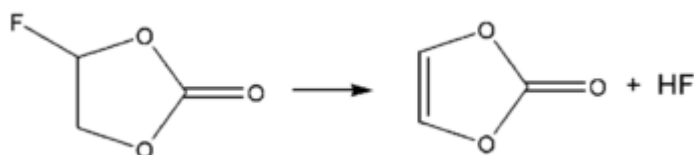
Figure 7. Decomposition reaction of FEC.

The addition of LiBOB generates surface films with a higher concentration of oxalates and $Li_xPF_yO_z$, but lower LiF providing a modest improvement in cycling performance on Si thin film [87]. Based on XPS analysis, LiBOB reacts with the major SEI components such as lithium alkyl dicarbonate and lithium alkoxide to form a more stable oligomer [98]. In addition, LiBOB has several additional functions; (1) it contributes to SEI formation and stabilizes SEI, (2) it reduces dissolution of the cathode materials, (3) it provides overcharge tolerance, and (4) it facilitates Al passivation in the electrolyte solution.

Li et al showed that the use of SA could help improve the interfacial properties of Si/C nanofiber by preventing the decomposition of $LiPF_6$ salt and preserving the integrity of the electrode electrode [96]. The addition has been reported to improve the electrochemical performance of Si thin film [95].
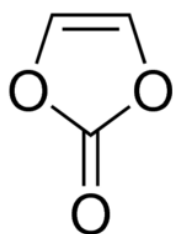
(a) vinylene carbonate (VC)
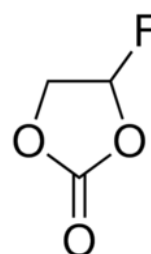
(b) fluoroethylene carbonate (FEC)
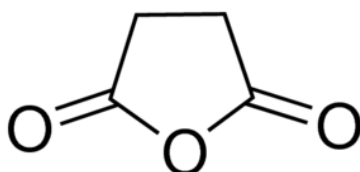
(c) succinic anhydride (SA)
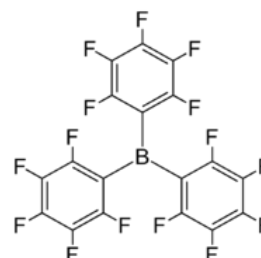
(d) tris(pentafluorophenyl)borane (TPPB)
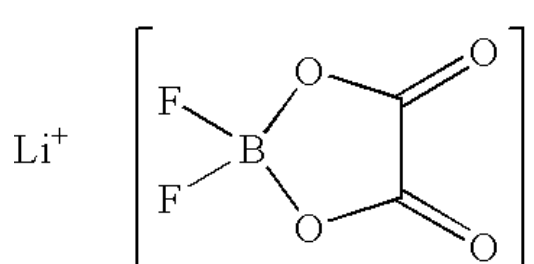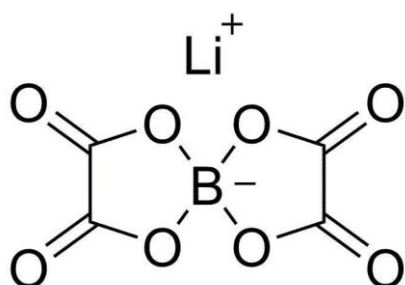
(e) lithium bis(oxalato)borate (LiBOB)   (f) lithium difluorooxalatoborate (LiDFOB)

Figure 8. Chemical structure of SEI modifier additives.

2.12.1 Rational design of silicon based electrode for a full cell configuration

Lee et al reviewed the rational design of silicon-based composites for high-energy storage devices [99]. The total specific capacity of the electrode material of batteries is calculated as a function of the specific capacities of the anode (Q_A) and cathode (Q_C) using equation (8).

$$\text{Total specific capacity } (mAhg^{-1}) = \frac{1}{(^1/_{Q_A} + ^1/_{Q_C})} \qquad (8)$$

Figure 9 displays the total specific capacity of a Li-ion battery as a function of the specific capacity of anode and cathode. The total specific capacity increases significantly with an increasing specific capacity of anode up to about 800-1200 mAhg^{-1} and afterwards it reaches a saturation. The total specific capacity can be also increased by using a high capacity cathode. The total specific capacity of current commercial Li-ion batteries in the range of 101-117 mAhg^{-1}, as a combination of a LiCoO$_2$ cathode (140-170 mAhg^{-1}) and a graphite anode (372 mAhg^{-1}). When a high capacity cathode material (200 mAhg^{-1}) combined with a capacity anode of 1000 mAhg^{-1}, it will yield 52% increase in the total specific capacity. However, the shift from graphite to silicon is more critical for reducing volume of the Li-ion batteries, especially for electrical vehicle applications.
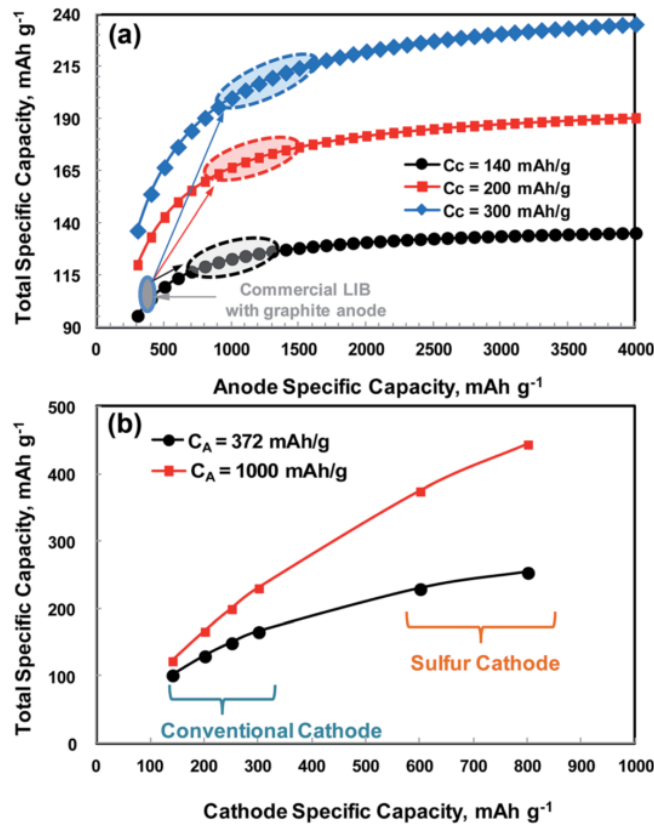
Figure 9. Total specific capacity of a Li-ion battery as a function of the specific capacity of (a) anode and (b) cathode [99].

Recently, Dash et al. reported the theoretical limits of specific capacity of silicon-carbon composite anode [100]. Figure 10 displays the relationship between specific capacity of silicon carbon composites anode and amount of Si in the anode. The specific gravimetric capacity of anode increases linearly with the Si content. However, the specific volumetric capacity of anode increases with the Si content up to a limiting value and then it decreases. This is because any further Si will lead to increased volume expansion which requires higher porosity. From Figure 10, the treshold value was determined to be 11.68 wt.% and the maximum capacity of the SCC anode with no volume expansion constraint was determined to be ~935 mAh.cc^{-1} and ~712 mAh.g^{-1}.
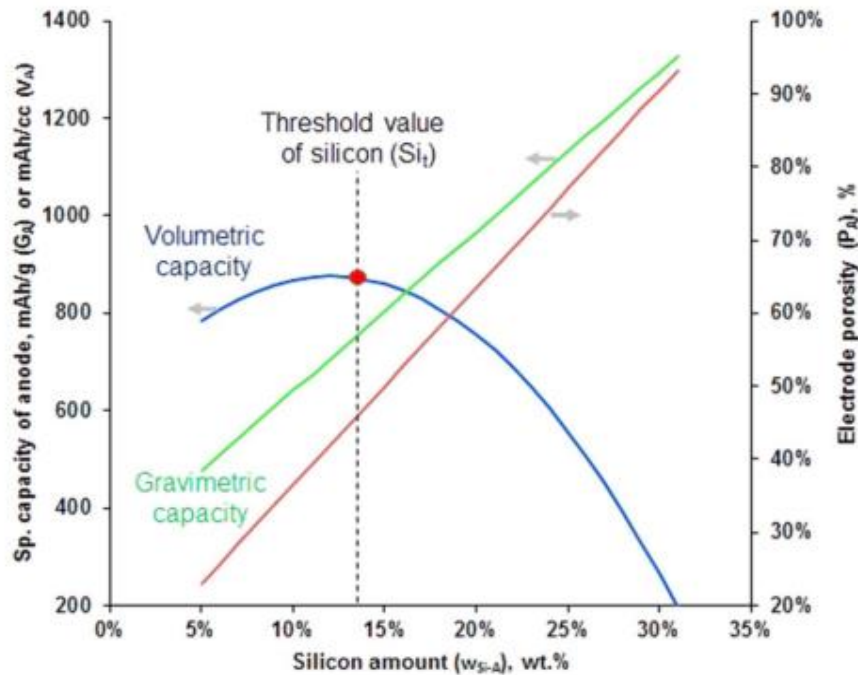
Figure 10. Relationship between specific capacity of anode and the amount of Si in the anode, w_{Si-A} and porosity of anode [100].

2.12.2 Full cells containing Si-based anodes

For full evaluation of the electrochemical performance of Si-based anodes, tests in a full-cell configuration are required. This is an essential step that must be taken before commercialization. However, studies of full cells containing Si-based anodes are still rare. Several studies using Si-based anodes with different standard cathodes such as $LiCoO_2$ [53], [101], [102], $LiFeO_4$ [103], $LiNi_{1/3}Mn_{1/3}Co_{1/3}O_2$ [104], $Li_{1.2}Ni_{0.2}Mn_{0.6}O_2$ [105], $LiMn_2O_4$ [106], have been done by many groups. Yang et al. fabricated a amorphous Si film with an average thickness of 2 μm coupled with commercial $LiCoO_2$ cathode [101]. In the voltage range 2.5–3.9 V at 0.2C, this full cell retained 1159 mAh g^{-1} after 300 cycles. Full cells using 4 μm and 6 μm thick Si films as the anodes and standard commercial $LiCoO_2$ as the cathodes (70 μm thick) delivered stable capacity of about 1.8 mAh cm^{-2} for 200 cycles [102]. A Li-ion full cell with $LiCoO_2$ as cathode and SiNTs as anode delivered a specific capacity above 3000 mAhg^{-1} and a capacity retention of 89% at a rate of 1C [53].

Chapter III

Experimental Methods

This chapter will focus on the experimental methods. It consists of : i) synthesis optimization of Si/MC composite anodes, ii) material characterization of Si/MC powder iii) Si/MC electrode preparation, iv) electrochemical tests of Si/MC anodes in a half cell and a full cell.

3.1   Synthesis optimization of Si/MC composites

Silicon nanoparticles (SiNPs) with particle size of 30–50 nm were purchased from Nanostructured and Amorphous Materials Inc., USA. The commercial SiNPs were originally prepared by laser driven reaction of silane gas (SiH_4). Table 3 lists the physical properties of the commercial SiNPs. Resorcinol (Merck KGaA) 0.29 M and formaldehyde solution (Merck Schuchardt) 0.57 M were used for preparing the gel, following a previous method [107]. As formaldehyde was used as precursor, the reaction rate would be too slow at low pH. Therefore, the pH value was adjusted in the range of 6.5 – 7.4 by adding 5vol% NH_3 (Carl Path GmbH) in H_2O. The solution was put into a sealed vial, while the temperature was maintained at 85℃. Figure 11 illustrates the mechanism of the sol gel polymerization of resorcinol and formaldehyde. Resorcinol (1,3-dihydroxybenzene, $C_6H_4(OH)_2$ is a phenolic tri-functional compound, which is capable of adding formaldehyde (HCHO) in the 2-, 4-, and/or 6- positions of the aromatic ring. The reactions include an addition reaction to form hydroxymethyl derivatives (-CH_2OH) of resorcinol and a condensation reaction of hydroxymethyl derivatives forming a 3-dimensional network (so-called RF gel), crosslinked by methylene (-CH_2-) and methylene ether (-CH_2OCH_2-) groups.

Table 3. Physical properties of commercial Si nanopowder.

Bulk density	~0.08 g/cm³
True density	2.33 g/cm³
Specific surface area	70-80 m²/g
Average particle size	30 - 50 nm
Morphology	Spherical
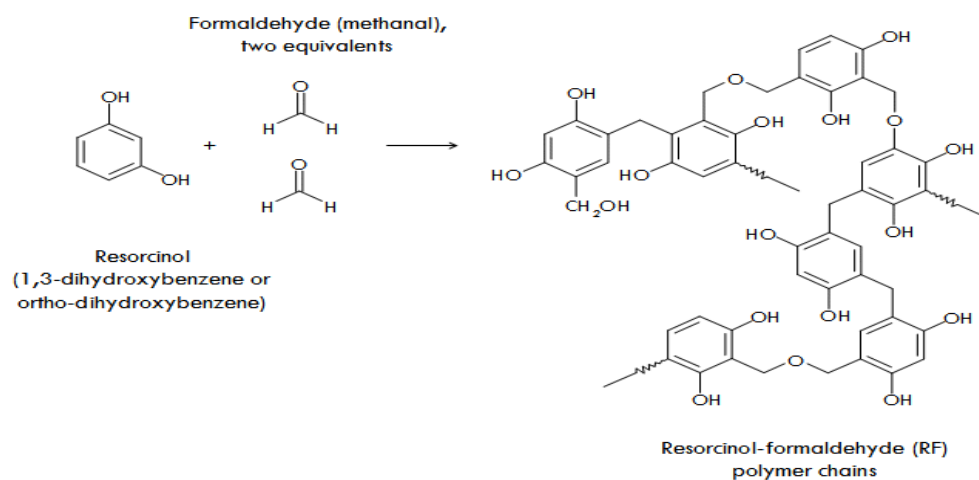
Figure 11. Reaction mechanism of sol-gel polymerization of resorcinol with formaldehyde [108].

Resorcinol-Formaldehyde (RF) gel was chosen to envelope SiNPs since the shape of carbons after pyrolysis from RF gel can be easily controlled [109]. The polymer-like elasticity of the fibrous carbon matrix which is obtained from pyrolysis of the RF polymer could further mitigate the induced stress of Si. When solution became viscous with a milky orange white appearence, SiNPs with particle size 30-50 nm were dispersed. The obtained gel was dried in a vacuum oven overnight. The dried n-Si/RF was calcined at 650°C for 10 h under flowing Argon to yield Si/MC composites. The pyrolysis step transformed the organic gel into a pure carbon structure by removing remaining oxygen- and hydrogen containing groups at an elevated temperature. The temperature of 650°C was used to adjust the surface area. The received powder was mixed using ball milling for better homogenization. The obtained samples were immersed in 1M HF solution for 1 h. Then, the powders were filtered, rinsed off with distilled water to remove any residual HF, and dried in an oven at 120°C for 24 h. HF etching aimed to increase the porosity of Si/MC composites. Si contains oxide layer because it is thermodynamically unstable in air. The Si-F bond (158 kcal mol^{-1}) is the only bond stronger than Si-O (123 kcal mol^{-1}). The higher Si-F bond enthalpy drives the main chemical dissolution reaction used to make porous silicon. In the presence of aqueous HF, SiO_2 spontaneously dissolves as SiF_6^{2-} following the equation [iv] [110]. Finally, Si atoms are etched away from the Si surface by reaction with HF, thus, it generates pores. The schematic diagram of the preparation of Si/MC composites can be seen in Figure 12.

$$SiO_2 + 6HF \rightarrow SiF_6^{2-} + 2H^+ + 2\,H_2O \qquad\qquad [\,iv\,]$$
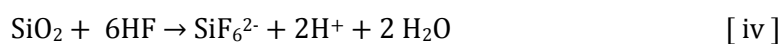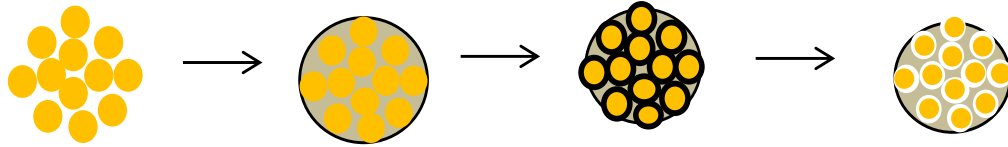
Figure 12. The schematic diagram of the preparation process of Si/MC composites.

3.2 Analytical method and material characterization of Si/MC materials

Characterization of Si/MC composite materials was conducted to understand their distinctive properties. They were aimed to control the synthesis process and to analyze the reason of materials fail during cycling.

3.2.1 Structural characterization

The crystalline structure of the materials was characterized by X-ray Diffraction (XRD) technique. XRD is based on the constructive interference of monochromatic X-rays and a crystalline sample. The constructive interference occurs when the conditions applied satisfy Bragg's Law :

$$n\lambda = 2\,d\,\sin\theta \qquad\qquad (\,9\,)$$

where λ : the wavelength of the rays

θ : the angle between the incident rays and the surface of thecrystal

d : the spacing between layers of atoms

Conversion of the diffraction peaks to d-spacings can be used to identify the material because each material has a unique d-spacings. This is achieved by comparison with the d-spacing of the standard reference. In this work, the structure of material was determined using a X′PERT (PRO) POWDER–Panalytical. X-ray was generated by Cu-Kα radiation (λ = 1.5418Å). The data fitting was carried out by HighScore Plus software.

3.2.2 Physical adsorption characterization

33

The porosity of the materials and electrodes was characterized by using N_2 adsorption-desorption. The specific surface area was calculated based on the amount of gas adsorbed as a monomolecular layer on the surface using the Brunauer-Emmett-Teller (BET) adsorption isothern equation :

$$\frac{1}{\left[V_a\left(\frac{P_0}{P}-1\right)\right]} = \frac{C-1}{V_M C} x \frac{P}{P_0} + \frac{1}{V_M C} \qquad (10)$$

where   P : partial vapour pressure of adsorbate gas in equilibrium with surface at 77.4 K of liquid nitrogen.

P_0 : saturated pressure of adsorbate gas.

V_a : volume of gas adsorbed at standard temperature

V_m : volume of gas adsorbed to produce apparent monolayer on the sample surface

C : constant which is related to the enthalpy of adsorption of the adsorbate gas on the powder sample

The pore volume and pore size distributions were derived from the desorption branches of the isotherms using the Barrett–Joyner–Halenda (BJH) method [111]. N_2 adsorption-desorption was carried out using a Quantachrome Instruments Autosorb iQ, US.

3.2.3   Material composition characterization

The composition of the synthesized Si/MC composite materials was determined by thermal gravimetric analysis (TGA). TGA is a technique in which mass of a substance is monitored as a function of temperature or time. The analysis was conducted on a STA409 C/PC-PFEIFFER VACUUM TGA-7 analyzer (NETZSCH-Gertebau GmbH, Germany) in air atmosphere from 20°C to 1100°C with a heating rate of 5°C min^{-1}.

3.3   Electron Microscopy

3.3.1   Scanning Electron Microscopy (SEM)

The surface morphology of the samples has been observed using SEM. SEM uses a focused beam of high-energy electrons which carry a significant amount of energy to generate a

variety of signals at the surface of solid specimen. The signals that derive from electron-sample interactions reveal information about the external morphology (texture), chemical composition, and crytalline structure and orientation of materials. SEM analysis was conducted by FEI/Philips XL-30 Field Emission ESEM coupled with an energy dispersive X-ray spectroscopy (EDX). In this work, no prior metallization step was required because the samples were sufficiently conductive for characterization. SEM analysis was carried out in AIT Austrian Institute of Technology, Vienna University of Technology, and FELMI-ZFE Institute for Electron Microscopy of the TU Graz.

3.3.2 Transmission Electron Microscopy (TEM)

TEM is a characterization tool for imaging nanomaterials to obtain quantitative measures of particles and/or grain size, size distribution, and morphology. An electron source at the top of the microscope emits electrons that travel through a vacuum in the column of the microscope. In order to visualize the specimen, the sample must be thin enough (typically <200 nm) to allow the electrons to pass through it. To get information on the inner structure of the particles, a thin cross-section of the electrode was prepared by Focused Ion Beam (FIB). In this study, TEM analysis was carried out on a FEI Tecnai F20 TEM/STEM.

3.4 X-ray Photoelectron Spectroscopy (XPS)

Surface compositional analysis was conducted using ex-situ XPS. XPS is a technique for analyzing the surface chemistry of a material. XPS can measure the elemental composition, empirical formula, chemical state, and electronic state of the elements. Spectra of XPS are obtained by irradiating a solid surface with a beam of X-rays and simultaneously measuring the kinetic energy of emitted electrons. When an atom or molecule absorbs an X-ray photon, an electron is ejected. The kinetic energy (KE) of the electron depends on the photon energy (hv) and the binding energy (BE) of the electron following this equation :

$$KE = h\nu - BE \qquad\qquad (11)$$

This study used XPS Monochromatised Al-K alpha (1486.7 eV) at 88 W. The pressure during measurements was 10^{-8} mbar. Maximum energy resolution of the survey measurements in the configuration was 500 meV (at 100 eV Pass Energy). Detailed spectra have been recorded with a maximum resolution of about 50 meV (at 80 eV Pass Energy). For postmortem analysis, samples were prepared by extracting the electrodes from the coin

cells in an Ar-filled glove box. The electrodes were washed gently in extra pure DMC four times to remove Li salts and dried overnight in vacuum. All samples were mounted onto the sample holder inside a glove box and transported inside a desiccator where the samples have been exposed to air for no more than 1 minute before being entered into the ultra-high vacuum chamber of the XPS system. CASA-XPS software was used for data analysis. Quantification of the detected elements was carried out from survey scans using transmission corrections, Scofield sensitivity factors and Tougaard backgrounds [112]. XPS analysis was conducted at Analytical Instrumentation Center, Vienna University of Technology.

3.5   Electrochemical test procedures

3.5.1   Si/MC electrode preparation

For the base electrode, Si/MC composites (92 wt%) were mixed with polyacrylic acid (PAA, 8 wt%), and dissolved in N-methyl-2-2pyrrolidinone (NMP) solution. PAA was purchased from Sigma-Aldrich, USA. PAA was selected because of its high concentration of carboxylic function groups which interact strongly with the Si anode [63]. In addition, PAA adheres more strongly to the copper (Cu) collector than PVdF and CMC. This was proved by using a 180° peel test [113]. The test was based on measurements of the load (N cm^{-1}) required to peel the anode off the Cu collector. PAA binder has less interaction with the electrolyte solvent compared to PVdF which allowed the formation of a stable SEI [83]. NMP solution was selected as solvent instead of aqueous solvent to prevent SiO_2 formation during slurry preparation. The resulting slurry was casted onto a 0.01 mm copper foil current collector. The coated electrode was dried under vacuum at 60°C for 2h, then at 120°C for 4h. The dried film was hot pressed at 120°C to adjust volume density of the electrode. The film was punched into 15 mm diameter discs to form working electrodes. The thickness of the active material without current collector was 0.05 mm with an amount of about 0.7 mg Si in the working electrode. 2032 type coin cells were then assembled in an Argon filled MBraun glove box using Li metal as a counter electrode and three layers of a polypropylene separator manufactured by Freundberg (thickness: 25 μm). The schematic configuration of the lithium coin cell is described in Figure 13. The schematic diagram of the whole preparation procedure of the electrodes is illustrated in Figure 14.

36
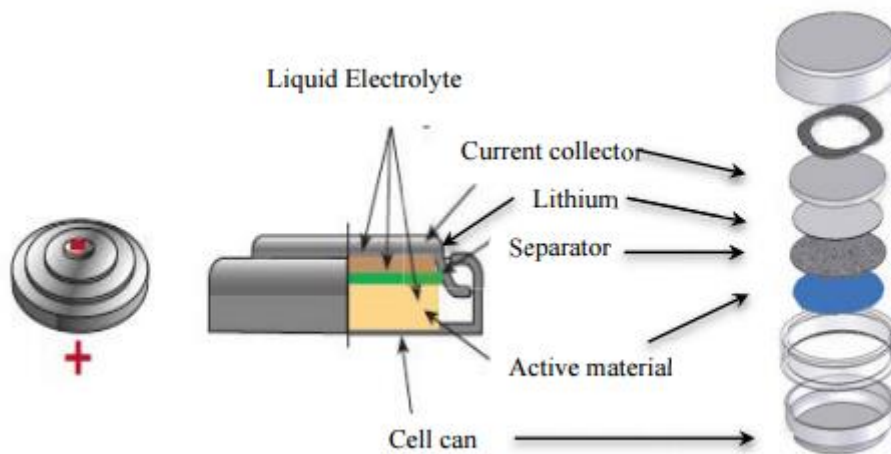
Figure 13. Schematic configuration of coin cell.
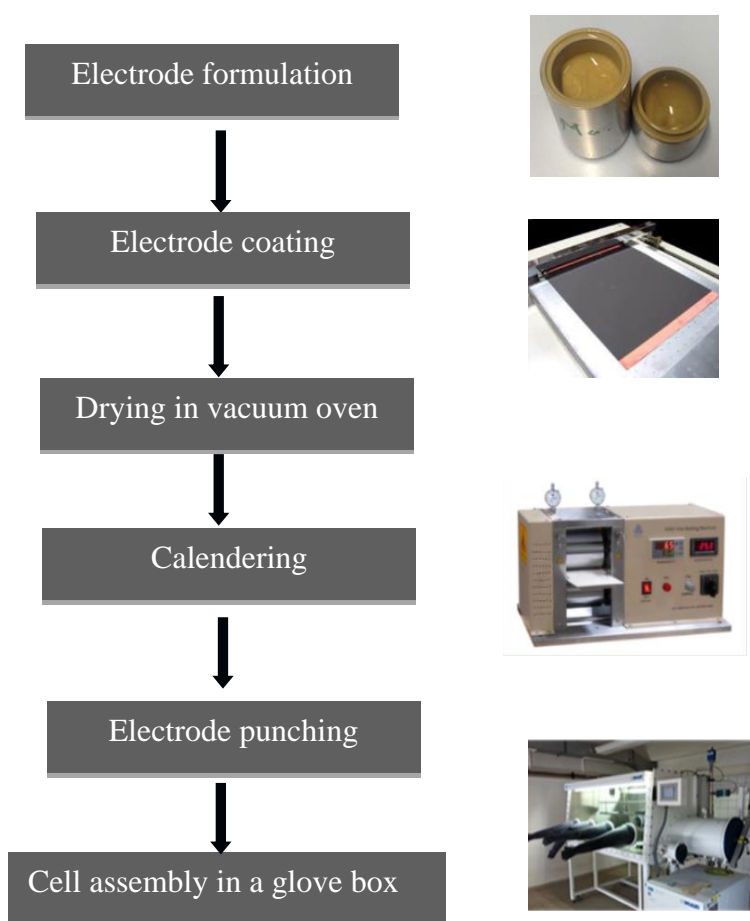
Figure 14. The schematic diagram of the whole preparation procedure of Si/MC composite electrodes.

For the investigation of the effect of conductive additives on Si/MC electrodes, the used electrode compositions are summarized in Table 4.

Table 4. The composition of Si/MC electrodes with different conductive additives.

electrode	Active material	Conductive additive	Binder
Si/MC	Si/MC composites (92 wt%)	no conductive additive	PAA (8 wt%)
Si/MC/G	Si/MC composites (75 wt%)	graphite (15 wt%)	PAA (10 wt%)
Si/MC/CB65	Si/MC composites (75 wt%)	Super C65 (15 wt%)	PAA (10 wt%)
Si/MC/CB45	Si/MC composites (75 wt%)	Super C45 (15 wt%)	PAA (10 wt%)
Si/MC/CB&G	Si/MC composites (75 wt%)	graphite (7.5 wt%) & Super C65 (7.5 wt %)	PAA (10 wt%)

For the investigation of the electrolyte additives on SEI film formation, two sets of experiments have been carried out. Table 5 shows the composition of the standard electrolyte and electrolytes with different electrolyte additives. While, Table 6 shows the composition of the standard electrolyte and electrolyte with different concentrations of VC additive.

Table 5. The composition of standard electrolyte and electrolyte with additives.

Electrolyte	Composition
Standard	1 M $LiPF_6$ in EC : DMC (1:1)
5 wt% VC	1 M $LiPF_6$ in EC : DMC (1:1) + 5 wt% VC
5wt % SA	1 M $LiPF_6$ in EC : DMC (1:1) + 5 wt% SA
5wt% LiBOB	1 M $LiPF_6$ in EC : DMC (1:1) + 5 wt% LiBOB

Table 6. The composition of standard electrolyte and electrolyte with different concentrations of VC additive.

Electrolyte	Composition
Standard	1 M $LiPF_6$ in EC : DMC (1:1)
3 wt% VC	1 M $LiPF_6$ in EC : DMC (1:1) + 3 wt% VC
5 wt% VC	1 M $LiPF_6$ in EC : DMC (1:1) + 5 wt% VC
10 wt% VC	1 M $LiPF_6$ in EC : DMC (1:1) + 10 wt% VC

3.5.2 Cyclic voltammetry

Cyclic voltammetry is widely used for gaining qualitative information about electrochemical reactions. The technique allows us to identify the redox reactions and to determine rate constants and transfer coefficients of an electrode process. It can be used for in-situ analyses of electrode processes inside a battery. The potential of a working electrode versus a reference electrode is linearly shifted at a constant scan rate and the resulting current is measured. A cyclic voltammogram is obtained by recording the current at the working electrode over time during the potential scans. Figure 15 shows the curve of voltage as a function of time and of the current as function of the voltage. The reduction process occurs from the initial potential to the cathodic reverse potential. In this region, the potential is scanned negatively to cause a reduction. The resulting current is called cathodic current. After the reverse potential has been reached, the potential scans positively to cause oxidation. In this work, cyclic voltammetry measurement of electrodes was conducted on a VersaSTAT at a scan rate of 20 µV/s in the potential range of (0.01-1) V vs. Li/Li$^+$. To study the diffusion coefficient of Li-ion, cyclic voltammetry with different scan rates (0.02, 0.05, 0.2 and 0.5 mVs^{-1}) was performed on a Biologic VMP3 multichannel system in the potential range of (0.01-1) V vs. Li/Li$^+$.
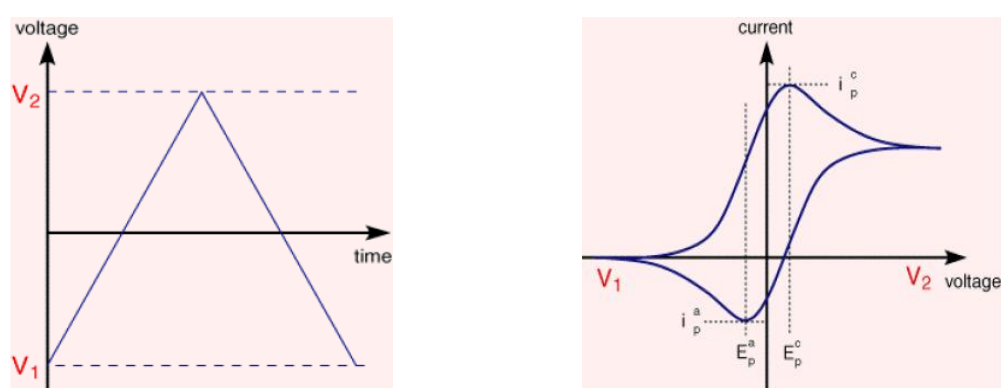
Figure 15. Voltage as a function of time and current as a function of voltage for CV.

3.5.3 Charge/Discharge tests

Charge/discharge tests were performed using the constant current-constant voltage (CCCV) mode. The CCCV test is the most widely used for lithium cells because it provides safe charge/discharge by limiting the cut off voltage. Current as a function of time for CCCV mode is illustrated in Figure 16. To avoid lithium plating, the charging process proceeded to 0.01V vs. Li/Li$^+$ with a constant-current (CC) mode. After the potential set point is reached, the cell potential is proceeded with a constant-voltage (CV) mode at 0.01 V until the current density

decreased to 1/10 of initial specific capacity. Afterwards, the discharging process proceeded to 1 V with CC mode.
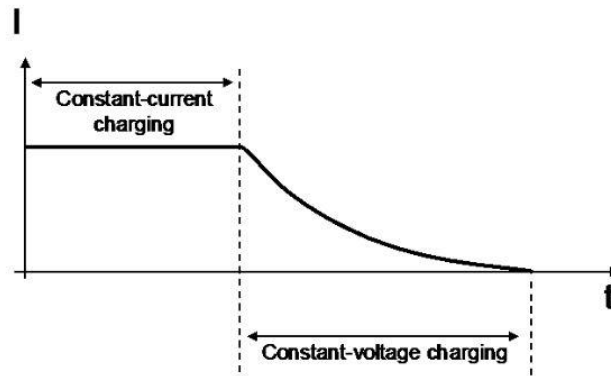
Figure 16. Current as a function of time for CCCV mode.

The charge/discharge test can give information about the electrode's specific capacity and stability, the quality of electrode material, the presence of side reactions (shifted specific potential plateaus), and the life time of the cell. The rate was calculated based on theoretical specific capacity for Si (1C = 3850 mAhg^{-1}). The rate for carbon was calculated based on theoretical specific capacity of graphite (1C = 372 mAhg^{-1}). The theoretical specific capacity of Si/MC composites ($C_{Si/MC}$) is determined as follows :

$$C_{Si/MC} = \frac{m_{Si} \times 3850 \ mAhg^{-1} + m_C \times 372 \ mAhg^{-1}}{m_{Si} + m_C} \qquad (12)$$

Where m_{Si} : mass of Si

               m_C : mass of carbon

3.5.4   Rate capability tests

The rate capability test is a useful technique to asses the electrochemical performance of an electrode. It measures the amount of charge stored in an electrode under various experimental conditions with increasing cycle numbers. So basically, the test ensures the stability of a battery under relatively high current density. The specific current can be expressed in terms of a C-rate, as used for charge/discharge test. The rate capability of the

electrodes was evaluated in a constant current (CC) mode at various C-rates of C/10, C/5, C/3, 1C, and 2C. The test was performed at room temperature using a Maccor Series 4000 battery tester.

3.5.5 Electrochemical impedance spectroscopy

Electrochemical Impedance Spectroscopy (EIS) is a powerful tool to study the electrochemical processes at the electrodes of Li-ion batteries. This method is based on a frequency (ω) dependent resistance of electric circuits. The system is excited from the equilibrium due to a voltage (U) or current (I) perturbance. The impedance can be calculated according to Ohm's Law (R = U/I). The impedance consists of a real part, which is attributed to ohmic resistances and an imaginary part. These values are plotted in a so-called Nyquist plot with a real axis (Z_{Re}; x-axis) and an imaginary axis (-(Z_{im}); y-axis). By using EIS, the kinetics of different reaction steps during the electrochemical reaction on the electrode can be observed by recording the impedance over a wide range of frequencies. EIS measurements were performed before and after charge-discharge tests within a frequency range of 500 kHz to 0.1 Hz. The applied AC voltage was 10 mV. The EIS data were fitted with EC-Lab® software, so-called Z Fit. Z Fit automatically determines the successive EIS values of the EC components for a series of impedance diagrams [114].

3.6 Full cell with Si-based anodes

3.6.1 Cell fabrication

In this study, a Silicon/mesoporous carbon (Si/MC) negative electrode and a commercial Li(Ni$_{1/3}$Co$_{1/3}$Mn$_{1/3}$)O$_2$ (NMC) positive electrode were used for assembling a full cell. This study was carried out in Applied Electrochemistry laboratory in KTH Royal Institute of Technology. To investigate the contribution from each electrode, a NMC half cell and a Si/MC half cell were assembled and coupled with Li metal as reference. All cells were fabricated as pouch-type cells with the dimension shown in Table 7. The cell chemistry used in this study can be seen in

Table 8. A cross sectional view of the pouch cell can be seen in Figure 17.

Figure 17. A cross sectional view of pouch cell configuration

Table 7. Pouch cell construction.

Cell dimensions	80 mm x 80 mm
Electrode dimensions	Cathode diameter : 15 mm Anode diameter : 15 mm
Tabs	Anode : copper Cathode : aluminium Reference for the half cell : nickel

Table 8. Cell chemistry of a pouch cell.

Component	Composition
Negative electrode	75% Si/MC 15% Super C45 10% Polyacrylic Acid (PAA, Sigma Aldrich) 15 μm Cu foil Loading density : 0.95 mg.cm^{-2}
Positive electrode	Li(Ni$_{1/3}$Co$_{1/3}$Mn$_{1/3}$)O$_2$ (Electrodes and more) Loading density : 10 mg.cm^{-2}
Electrolyte	1 M LiPF$_6$ in EC:DEC in a 1:1 weight ratio (LP40, BASF, battery grade)
Separator	Whatman glass microfiber Thickness: 260μm

3.6.2 Electrochemical characterization

Electrochemical measurements were conducted under galvanostatic mode at room temperature. To characterize the NMC half cell, the test was performed at C/10 with a cut-off voltage 2.6 – 4.1 V vs. Li/Li+ using the Biologic VMP3 multichannel system. The Si/MC half cell was cycled with CCCV mode at C/10 (for 4 cycles) and 1C (for subsequent 20 cycles after long resting) with a cut-off voltage 0.005 – 1 V vs. Li/Li+ using the PARSTAT. To investigate the electrochemical performance of the full cell, charge-discharge tests were performed at C/10 for the first cycle and 1C for subsequent cycles with a cut-off voltage 2.6 – 4 V using the Biologic VMP3 multichannel system. Charge-discharge current used for the full cell was the same with the Si/MC half cell.

3.7 Data calculations

The charge and discharge data were analyzed by differential capacity (dQ/dV) and differential voltage (dV/dQ) analysis. The dQ/dV is calculated by the equation (13).

$$\frac{|dQ|}{dV} = \frac{|Q_1 - Q_{t-1}|}{V_t - V_{t-1}} \qquad (13)$$

Where, Q_t, V_t are capacity and voltage measured at a given time t. Q_{t-1}, V_{t-1} are capacity and voltaged measured at a previous time.

In this study, the dQ/dV curves was introduced by the Differential Capacity Analysis (DCA) tool in EC-Lab. The DCA tool transforms the voltage plateus on potential vs. capacity curves into identifiable peaks. These peaks can be associated with the phase transitions of electrode material.

On the other hand, the derivative of voltage with respect to capacity (dV/dQ) is suited for graphical analysis of battery data [115]. It can predict the capacity of battery, since the voltage of a full cell can be calculated from :

$$V_{cell} = V_{cathode} - V_{anode} \qquad (14)$$

$$(dV/dQ)_{cell} = (dV/dQ)_{cathode} - (dV/dQ)_{anode} \qquad (15)$$

Therefore, the contributions from anode and cathode add linearly.

Since the charge and discharge data were too noisy, mathematical filtering was required to emphasize the peaks. The filtering was performed using OriginLab software. A comparison of half cell and full cell was made. The half cell data were used as a basis for assigning the peaks in the full cell to the cathode, anode or a combination of both. The dV/dQ can be used

to analyze the capacity fading in a cell, however, in this work, it was used only to balance the cut-off voltage.

Chapter IV

Results and Discussions

Chapter IV will discuss about results and discussion of the thesis. It is divided into five main parts; (1) optimized method to synthesize silicon/mesoporous carbon (Si/MC) composites with HF etching, (2) investigation of three commercial conductive additives for Si/MC electrodes (Super C45, Super C65, graphite, mixture of Super C45 and graphite), (3) investigation of three additives (vinyl carbonate with different composition, succinic anhydride, and lithium bis(oxalate)borate) for reducing initial charge loss, (4) analysis of a realiability of the as-prepared Si/MC-based anodes, (5) electrochemical test of a full cell containing Si/MC/CB45 anode with commercial $LiNi_{1/3}Mn_{1/3}Co_{1/3}O_2$ cathode.

4.1   Si/MC composites for Li-ion Batteries anode material

The first subchapter will focus on the optimized method to synthesize Si/MC composites. The physicochemical and the electrochemical properties of the synthesized material will be discussed.

4.1.1   Structural and morphological properties of Si/MC composites

The XRD pattern of Si/MC before and after etching can be seen Figure 18. Figure 18a&b display XRD data for Si/MC before and after etching, respectively. Si/MC before etching presents diffraction peaks at 2θ of about 28.4°, 47.4°, 56.2°, and 69.2, corresponding to the (111), (220), (311), (400) planes of crystalline Si, respectively [116]. Two broad peaks at around 23° and 44° can be assigned to the (002) and (100) planes for carbon materials [117]. Si/MC composites after etching show similar diffraction peaks which means that etching process did not change the structure of the composites.
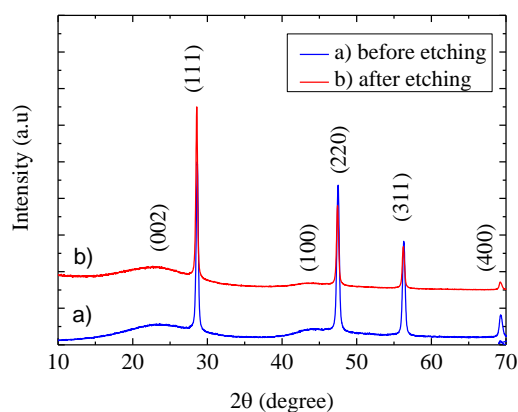
Figure 18. XRD patterns of the Si/MC composites before (a) and after etching (b).

The morphology of the as-synthesized Si/MC composites was investigated by SEM, shown in Figure 19a&b. The non-etched Si/MC composite (Figure 19a) shows that SiNPs with 30-50 nm sized are dispersed into the amorphous carbon network with 50 nm - 1μm sized. The etched Si/MC composite (Figure 19b) shows similar morphology. EDAX analysis was carried out to see the distribution of SiNPs and carbon in the powder, as presented in Figure 19c&d. The result shown in Figure 19c indicates that the non-etched Si/MC composites contain Si, C, and O. Oxygen can be derived from the Si-O layer from the native layer of commercial SiNPs. Similar spectrum can be seen in the etched Si/MC composites with less Si content (Figure 19).
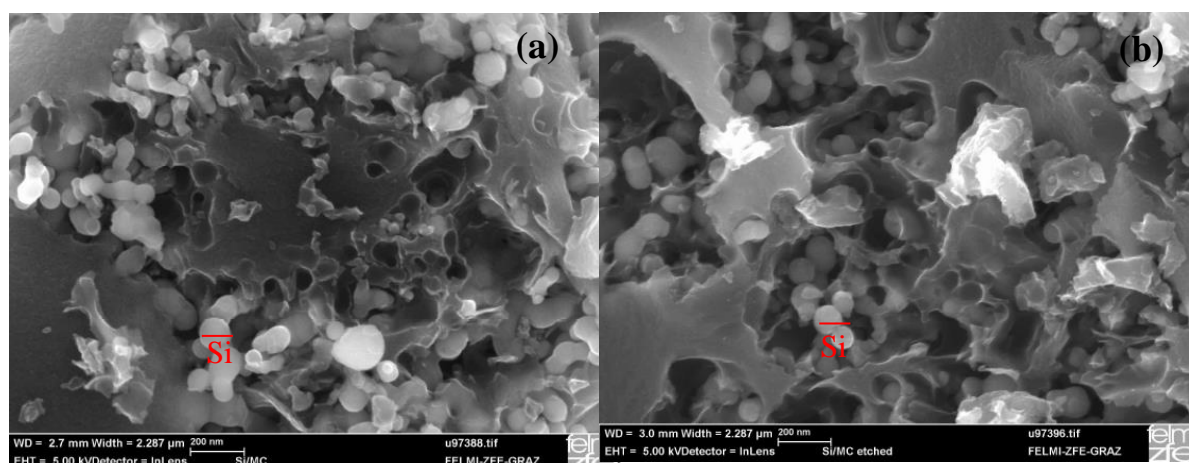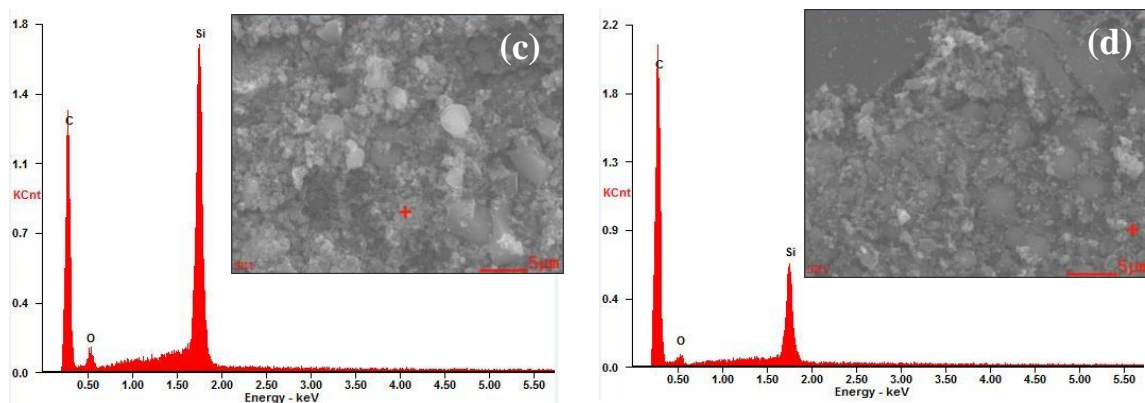
Figure 19. SEM images of the Si/MC composites before (a) and after etching (b), EDAX
spectrum of the Si/MC composites before (c) and after etching (d).

The morphology of the composites was further investigated by TEM, shown in Figure 20.
The dark color of the images corresponds to SiNPs and the grey color corresponds to
amorphous carbon layer. The TEM image of the non-etched Si/MC (Figure 20a) shows that
the Si agglomerates are completely enveloped by an amorphous carbon. For the etched
Si/MC (Figure 20b), SiNPs with ~50 nm are enveloped by the carbon layer with pores of
ca.10 nm.
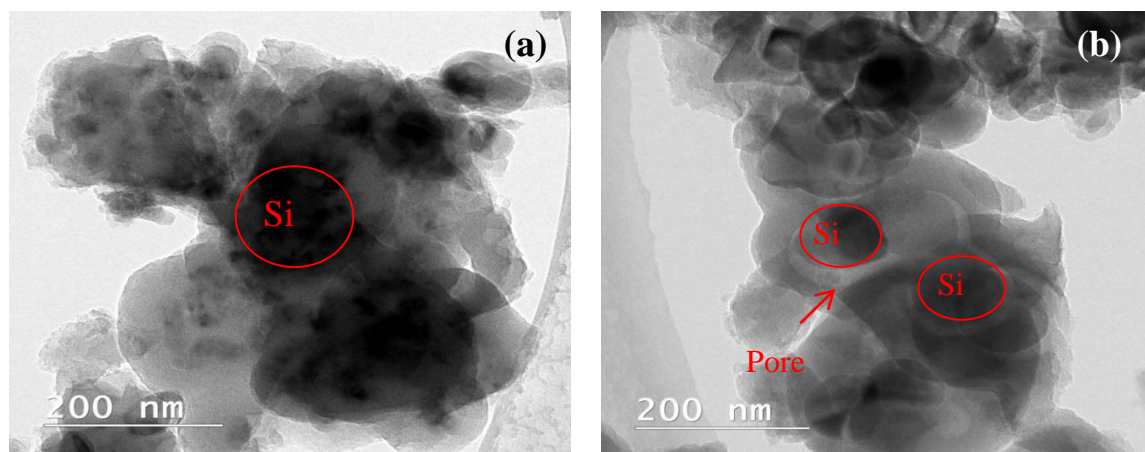
Figure 20. TEM images of Si/MC composites before (a) and after etching (b).

4.1.2   The composition of Si/MC composites

To check the different fractions of Si/MC composites, TGA was performed. Figure 21
presents TGA curves of the Si/MC composites before and after etching. The TGA curve of the
Si/MC composites before etching (Figure 21a) shows three decomposition stages in the

47

temperature ranges of 25-150°C, 150-450°C, and 450-800°C. The decomposition stage at ≥150°C corresponds to the loss of free water. From 450-800°C, the oxidation of carbon into CO_2 and evaporation of CO_2 takes place, then, it is completed at 800°C. The increasing mass above 800°C is caused by the oxidation of Si into SiO_2. The curve for the Si/MC composites after etching (Figure 21b) shows only slight differences. Slightly higher mass loss at 150°C corresponds to a higher water content in Si/MC after etching from the rinsing process. Another difference is the percentage of mass loss. Si content in the Si/C composite before etching was estimated to be 25 wt%, whereas in the Si/C composite after etching it was 12 wt%, which confirmed some Si removal. This result is in good agreement with the EDAX measurements.
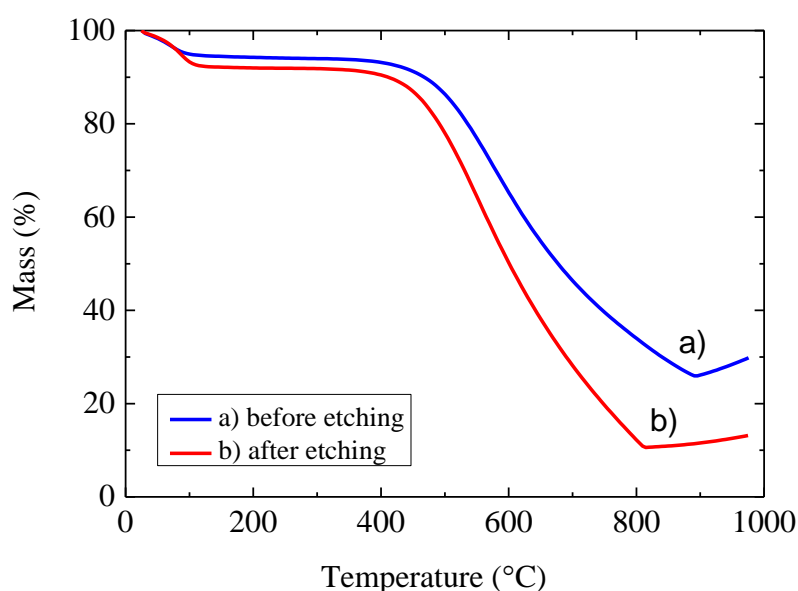
Figure 21. TGA curves of Si/C composites before (a) and after etching (b).

4.1.3 Physicochemical properties of Si/MC

The mesoporous structure in the Si/MC was further characterized by N_2 adsorption/desorption isotherms, shown in Figure 22a. At high pressures, the slope shows increased uptake of adsorbate as pores become filled and hysteris point occurs near the completion of the first monolayer. Such a plot is classified as type IV isotherm according to the IUPAC classification of the sorption isotherms. The type IV isotherm is typical for mesoporous adsorbents. Multipoint BET analysis yields a surface area of 432.95 m²g⁻¹ and the total pore volume of 0.140 cm³g⁻¹ for Si/MC before etching. The Si/MC composites after

etching have a surface area and a total pore volume of 526.32 m^2g^{-1} and 0.187 cm^3g^{-1}, respectively, higher than those of before etching. The BJH analysis gives an average pore diameter of Si/MC before etching of 3.733 nm (Figure 22b). The pore size distribution of the Si/MC composites after etching shows two maxima centered at 3.804 and 11.109 nm. The porous structures which are vulnerable to chemical etching due to their high specific surface area [118], resulted in increased pore diameter, which is also confirmed by the TEM analysis (Figure 20).
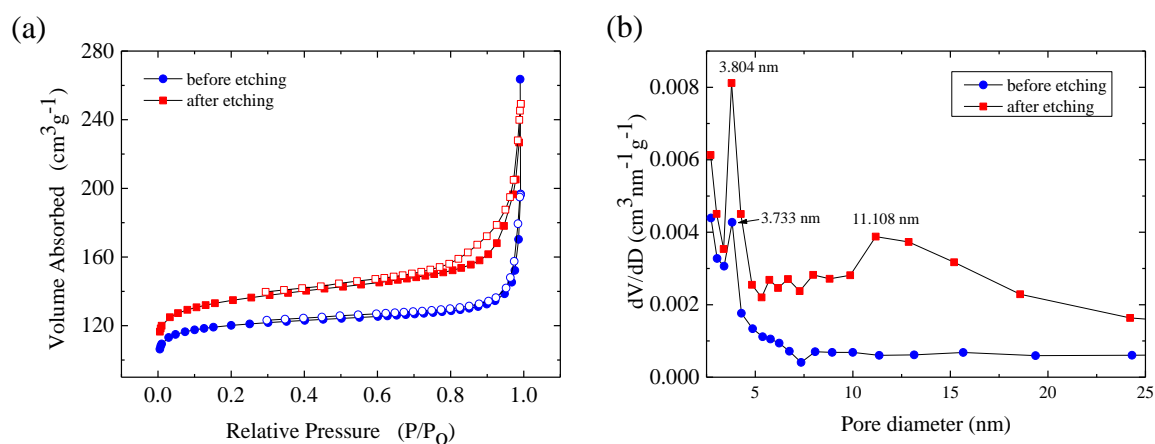
Figure 22. N_2 adsorption/desorption isotherm plots (a) and pore size distribution curve (b) of Si/MC composites before and after etching.

4.1.4   XPS measurement of Si/MC powder

4.1.4.1 Quantification of the sample content

The chemical composition of Si/MC powders before and after etching was investigated using XPS technique. Table 9 shows the relative contents (%) of the samples' surface regions (<10nm), while Figure 23 shows the survey spectra with the regions used for quantification. In addition to the elements C, O and Si, traces (<0.4 at %) of nitrogen have been detected in both samples. Traces of nitrogen can be derived from ammonia as a pH controller during synthesis. From the data in Table 9, it can be seen that after HF etching the O 1s and Si 2p Si/MC are attenuated, concomitant to a 10% decrease in O and a 20% decrease in Si content. As result, the content of C (at%) increases.

Table 9. Relative C, O and Si contents (at%) from XPS survey measurements (see also Fig. 6) for 3 different positions on Si/MC samples before and after HF etching.

Sample	Element(at%)		
	C	O	Si
before etching 1	85.3	11.6	3.1
before etching 2	85.2	11.6	3.3
before etching 3	85.3	11.5	3.2
before etching	**85.3**	**11.6**	**3.2**
after etching 1	87.0	10.1	2.9
after etching 2	87.4	10.2	2.4
after etching 3	87.1	10.2	2.7
after etching	**87.2**	**10.2**	**2.6**
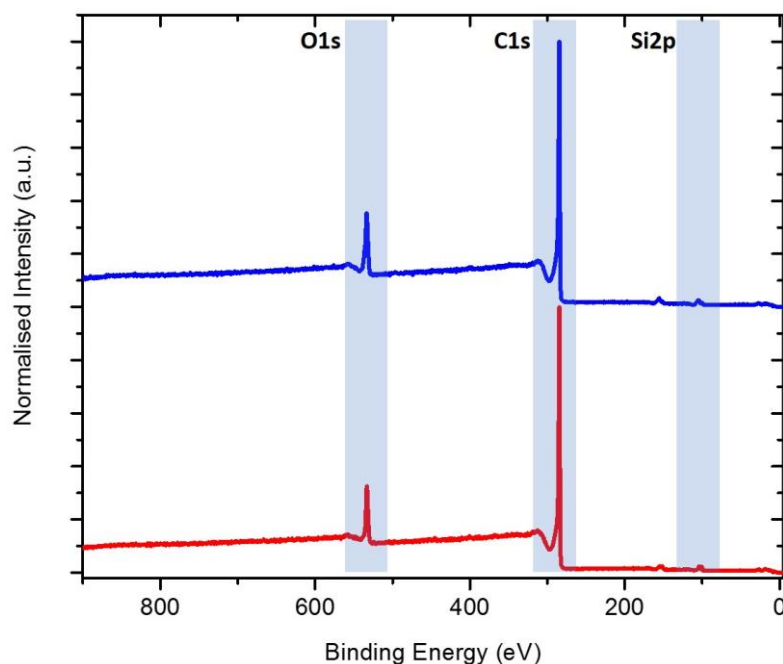
Figure 23. Normalised XPS survey spectra of Si/MC powders before and after HF etching. Blue areas show the regions used for quantification as shown in Table 9.

4.1.4.2 Determination of the chemical states of C, O, and Si

Each spectra line has been fitted using multiple peaks corresponding to components of different chemical states, depicted in Figure 24. C 1s spectra show several components visualized by dashed lines in Figure 24a. The large peak at 284.3 eV binding energy (BE) corresponds to C-C bonds that most probably stem from sp^2 carbon, resulting in the overall asymmetric shape of the C 1s signals. Components at 286.3 eV, 287.5 eV and 289 eV can be assigned to C-O/C-N, C=O and O-C=O bonds. The peak around 290 eV is usually attributed to CO_3 [119]. Most importantly, no significant changes caused by the etching process have been detected in the C 1s signal with the exception of a minor decrease in C-O/C=O/O-C=O signals. Thus, reduction of C/O groups is not the main reason for the overall decrease in O content after HF etching.

The Si 2p detail spectra (Figure 24b) show distinctly different peak structures for the Si/MC before and after etching. Symmetrical Gauss-Lorentz (70%-30%) curves have been used to discern the components of the Si 2p signal. While no major shifts in BE could be detected, the full width at half maximum (FWHM) of all peaks is larger by approximately 50% for the

51

non-etched sample. This behavior points to the non-etched sample being more insulating than the etched one.
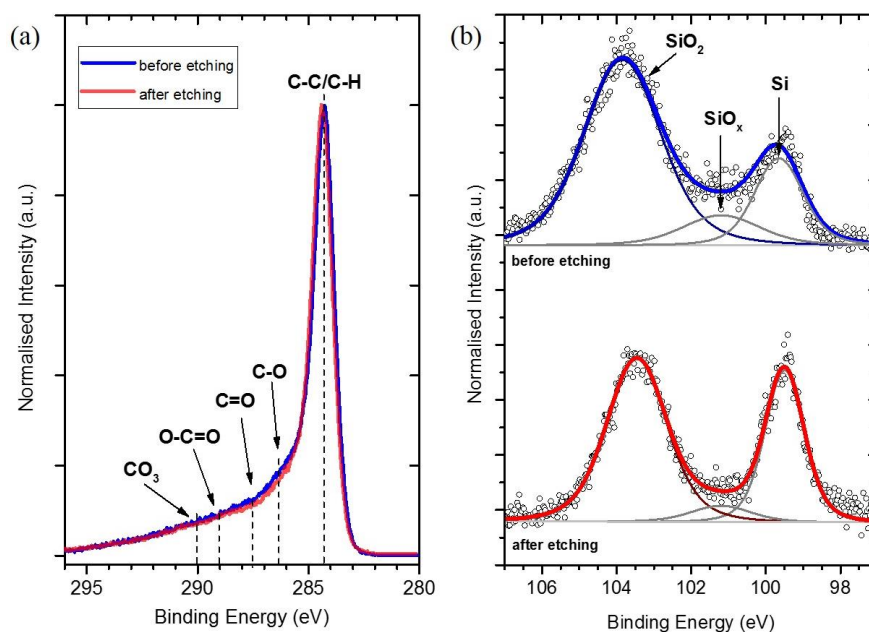
Figure 24. Normalised a C 1s and b Si 2p XPS detail spectra of Si/MC before and after HF etching. Dashed lines in a show the positions of different C/O components. Gaussian-Lorentzian line fits in b represent the Si components as noted on top. SiO_2 signals are shown in dark blue/red, other components in dark grey and the Tougaard background in light grey.

Table 10 summarizes the results of this analysis showing the component's relative abundance and possible assignments of the components.

Table 10. Relative abundance (at%) and possible assignments of the components found in XPS Si 2p detail spectra of Si/MC powder samples before and after HF etching.

Sample	Component (at%)		
	Si I	Si II	Si III
before etching	20.3	11.0	68.6
after etching	35.6	5.8	58.6
Assignment	Si	SiO/Si_3N_4	SiO_2

4.1.5 Electrochemical characterization of the Si/MC anodes

4.1.5.1 Contribution of MC to the specific capacity of Si/MC composite anodes

The electrochemical performance of the mesoporous carbon without Si, prepared by same recipe was evaluated further with charge-discharge test. As shown in Figure 25, the synthesized mesoporous carbon exhibited an initial specific capacity of 325 mAhg[-1]. The discharge capacity decreased to 55 mAh g^{-1} after the first cycle. As reported in a previous study [120], a significant amount of the initial capacity was consumed during SEI formation. The specific capacity of the mesoporous carbon electrode remains at 30 mAhg[-1] after 50 cycles. This result shows that the mesoporous carbon can be lithiated during cycling and contributes to the total specific capacity of Si/MC composites.
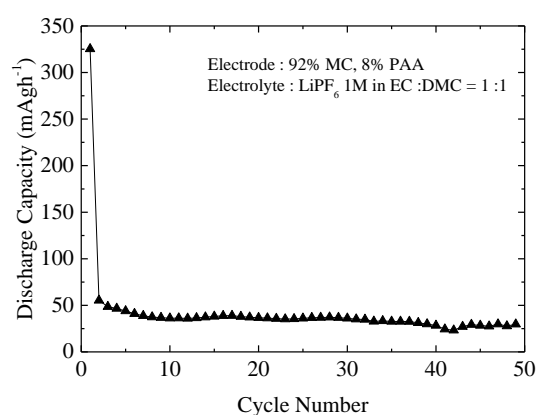
Figure 25. Discharge capacity vs. cycle number of synthesized mesoporous carbon with a charge/discharge current of C/10 from 1 to 0.005 V.

4.1.6 Cyclic voltammetry on Si/MC composite electrodes

Cyclic voltammetry plots from Si/MC electrode before and after etching are shown in Figure 26. The CV curves of Si/MC composite electrode before etching show a pronounced and broad peak at 0.5 V vs. Li/Li+ during the first cycle which disappears in the following cycles (Figure 26a). This peak can be assigned to the decomposition of the electrolyte, forming a SEI layer on the surface of electrode. The following cycles show reversible lithiation/delithiation signals. The peak at 0.2 V vs. Li/Li+ in the cathodic scan corresponds to the reduction of Li+ and the subsequent conversion of crystalline Si to amorphous (α) α-Li_xSi phase [63]. The two peaks at 0.35V and 0.5V vs. Li/Li+ in the reverse scan correspond to delithiation of α-$Li_{8.8}Si$ to α-Si. The delithiation current peaks exhibit an incrementally enhanced intensity from the first cycle to the following cycles. This phenomenon can be attributed mainly to the gradual breakdown of the silicon structure which accelerates Li ion

53

migration into Si due to reduction of the diffusion lengths. For the etched Si/MC (Figure 26b), a broad peak at 0.6 V vs. Li/Li+ during the first cycle is less pronounced, indicating less decomposition reaction of SEI formation. In addition, the constant delithiation current peaks indicate that the structure of Si after etching is more stable. The additional porosity may play a role as voids to accomodate the volume expansion of Si. In consequence, they may reduce the degradation of active material during lithiation/delithiation.
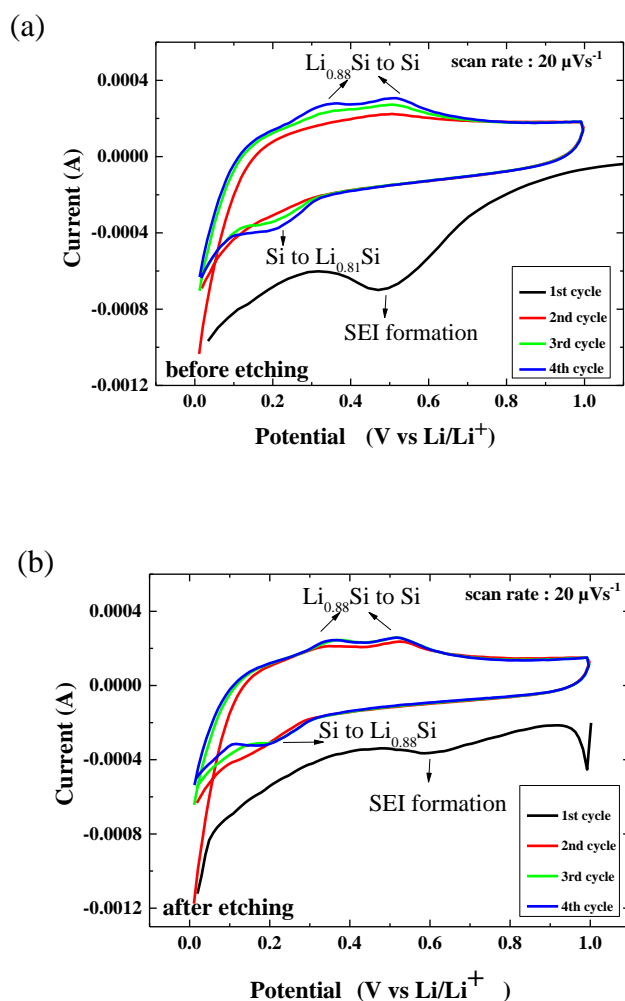
Figure 26. Cyclic voltammograms of Si/MC electrodes before (a) and after etching (b) at a scan rate of 20 μVs^{-1} over the potential window of (0.01-1) V vs. Li/Li+.

To assess the kinetics of Li absorption/desorption in mesoporous carbon in Si/MC electrodes, additional cyclic voltammetry tests on MC without Si were performed. Figure 27 shows the cyclic voltammograms of the synthesized mesoporous carbon electrode in a $LiPF_6$ 1M in EC:DMC 1:1. An increase of the cathodic current starting at 0.85 V vs. Li/Li+ is

observed in the first cycle of cathodic process and less pronounced also in subsequent cycles. This current indicates the irreversible capacity of SEI formation in inter-particles of mesoporous carbon [121]. A hump at 0.25 V vs. Li/Li+ corresponds to the reversible lithiation of amorphous graphitic structures. In anodic direction, the peak at 0.4 V vs. Li/Li+ can be attributed to the delithiation reaction of LiC_6 structures. This result confirms the results of the charge-discharge test that the as-synthesized mesoporous carbon is electroactive towards lithium.
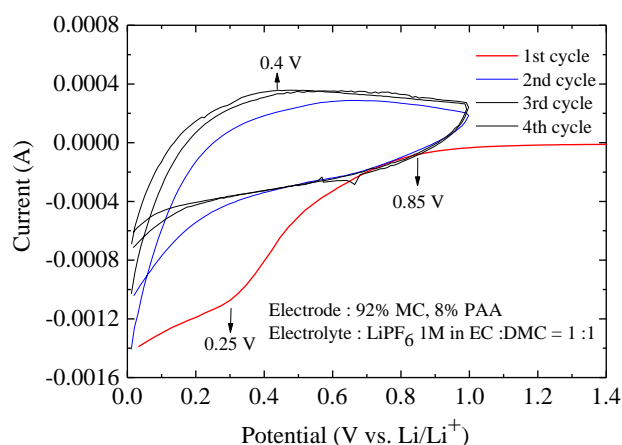
Figure 27. Cyclic voltammograms of synthesized mesoporous carbon in the potential window 0.01 – 1 (V vs. Li/Li+)

4.1.7 Galvanostatic charge/discharge cycles on Si/MC composite electrodes

The cycling performance of the Si/MC electrode before and after etching is compared in Figure 28. The non-etched Si/MC electrode shows a first discharge capacity of 3646 mAh g^{-1} with an initial CE of 18.26% (Figure 28a). The irreversible capacity loss of 81.74% during the first cycle can be assigned to intensive parasitic reactions between the active material and the electrolyte in forming the SEI layer. The reversible capacity decreases to 237 mAh g^{-1} after 135 cycles. The etched Si/MC composite electrode reveals an initial specific capacity of 4649 mAh g^{-1} with a CE of 29.14%. The initial specific capacity of the etched Si/MC is higher than the theoretical specific capacity of silicon (~4200 mAhg^{-1}). This excess can be explained by a contribution of mesoporous carbon matrix material to the overall capacity of the composite electrodes. It has been reported that mesoporous structure of carbon provided "cavities" to capture extra Li-ions [122]. The irreversible capacity loss of 70.86%

during the first cycle is lower than for the non–etched Si/MC electrode, indicating less side reaction from SEI formation. In addition, the CE profile of the non-etched Si/MC shows fluctuation. The reversible capacity of the etched Si/MC remains at 1027 mAh g^{-1} and 585 mAh g^{-1} after 50th and 135th cycles. Compared to the non-etched Si/MC, the cycling performance of the etched Si/MC is improved. The non-etched Si/MC showed an electrochemical performance better than previously reported RF coated Si anodes which have been synthesized using phenolic resolcinol precursor (700 mA h g^{-1} after 50 cycles) [123].
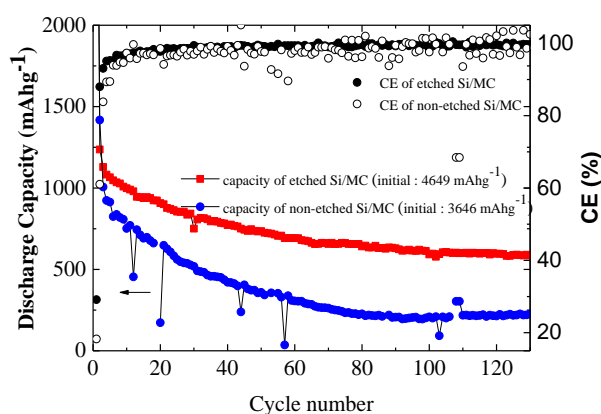
Figure 28. Cycling performance of the Si/MC electrodes before and after etching with a charge/discharge current of C/10 from 1 to 0.005 V.

To be noted that the etched Si/MC electrodes exhibited relatively good performance even without using conductive additive and electrolyte additives. The enhanced capacity of porous Si/MC can be explained by their highly accessible surfaces and short diffusion distances for Li ion. Thus, more SiNPs are involved in the reaction with Li ions. This improvement can be attributed to the reduced destruction of SiNPs during lithiation/delithiation. The pore structure plays a role in accomodating the stress that arises from volume expansion of the Si. The etched Si/MC was used as the base active material for the further optimizations.

4.1.8   Conclusions

Si/MC composites were synthesized by dispersing SiNPs into RF gel and subsequent carbonization. HF etching of the composites was conducted to remove passive layers and to produce a porous matrix between the Si and the carbon layer. The etched Si/MC electrode exhibits a reversible capacity of 585 mAh g^{-1} with Coulombic efficiency of 99.57% after 135

cycles. This material exhibits an improved lithium storage performance, capacity retention, and rate capability compared to a non-etched Si/MC electrode (237 mAh g^{-1} after 135 cycles). The improved cycling performance of the etched Si/MC composite can be attributed to its enhanced structural stability. The porous structure not only buffers the stress that arises from the volume change of Si but also facilitates the contact of the electrolyte with Si. In general, this preparation method is relatively simple and has a good potential for up-scaling.

4.2 Conductive additives and electrolyte additives for Si/MC electrodes

This second subchapter consists of the investigation of conductive additives for the as-prepared Si/MC electrodes. In order to improve the electrical conductivity of Si/MC anodes, the addition of proper conductive additives is necessary. In this study, three commercial conductive additives have been used: graphite, carbon black Super C65, carbon black Super C45, and the combination of graphite and Super C65. The main aspects for the investigations were: (i) the physicochemical and electrochemical properties of conductive additives, (ii) the effect of conductive additives on the morphology of Si/MC and (iii) the electrochemical performance of Si/MC anodes with different electrolyte additives. All the electrodes used for these experiments were prepared with equal overall compositions: Si/MC composites (75 wt%), conductive additive (15 wt%) and PAA (10 wt%) dissolved in NMP solvent. The composition of Si/MC electrodes with different conductive additives can be seen Table 4. The electrolyte used was LiPF$_6$ 1M in EC:DMC 1:1.

4.2.1 Physicochemical properties

Physicochemical properties of conductive graphite, Super C65, Super C45 were measured by using N$_2$ adsoprtion/desorption and presented in Table 11. The BET measurement shows that the specific surface area of Super C65 (62.062 m^2 g^{-1}) and Super C45 (43.547 m^2 g^{-1}) are higher than that of graphite (16.531 m^2 g^{-1}). According to the BJH calculation, the pore diameters were 2.735 nm, 2.741 nm, and 0.879 nm, for Super C65, Super C45, and conductive graphite, respectively. Super C65 has a size distribution that peaks at ~70 μm with a size range of 0.2 – 600 μm. The wide range in particle sizes of Super C65 may be caused by its structure which tends to aggregate. Super C45 has a size ditribution that peaks at ~2 μm with a size range of 0.04 – 15 μm. On the other hand, conductive graphite has a

size distribution that peaks at ~6 μm with a size of 0.4-20 μm. It can be seen that conductive graphite is more homogeneous in size compared to carbon black.

Table 11. The physicochemical properties of three commercial conductive additives: Conductive Graphite, Super C65, and Super C45.*

Name	Specific surface area (m^2 g^{-1})	Pore diameter (nm)	Particle size (μm)
Super C65	62.060	2.735	0.2 – 600
Super C45	43.547	2.741	0.04 - 15
Conductive Graphite	16.531	0.879	0.4-20

* The data were obtained from our measurement

4.2.2   Graphite vs. carbon black

First, it may be interesting to discuss the distinct properties of graphite and carbon black in terms of stucture, morphology and electrochemical properties.

4.2.2.1 Structural and morphology

Figure 29 shows X-Ray diffractograms of the three carbon samples ; Super C65, Super C45, and conductive graphite. The XRD pattern of conductive graphite exhibits three peaks at 25.6°, 44.2°, and 52.8°, which correspond to planes (002), (011), and (004), respectively, whereas the XRD pattern of Super C65 features broad peaks at 24° and 44.2°, which correspond to (002) and (011) planes, respectively [124]. The presence of a broad peak at 24°, instead of a narrow diffraction peak, is associated with the disordered structure of carbon black. Super C45 shows similar XRD pattern with that of Super C65. Conductive graphite has an ABABAB stacking arrangement, while carbon black is mainly amorphous and exhibits random rotations and translations as characteristic of turbostratic disorder. The degree of crystallinity was proven to influence the capacity, kinetics, and the first cycle irreversible capacity loss [125].
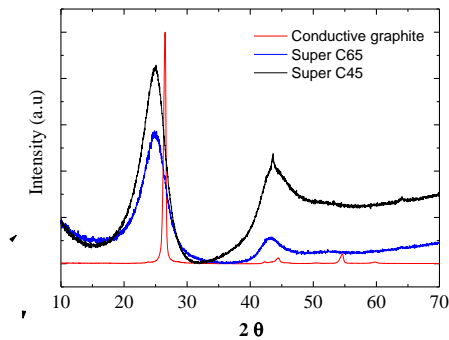
Figure 29. XRD patterns of three commercial conductive additives: Conductive Graphite (a), Super C65 (b), and Super C45 (c).

4.2.3 Electrochemical activity of conductive additives

The electrochemical lithiation/delithiation characteristics of carbon black (Super C65) and conductive graphite were determined using CV. Figure 30 presents CV curves for graphite and Super C65 at first cycle and fifth cycle. The CV curve (Figure 30a) shows a broad reduction peak at 0.8 V vs. Li/Li+ for conductive graphite and Super C65 at first cycle. This peak is attributed to the formation of an SEI layer during the first cycle, in which the ethylene carbonate (EC) based electrolyte decomposition normally takes place [126]. Due to the larger surface area of Super C65, the corresponding reduction peak is more pronounced (blue line), compared to that of graphite (red line). On graphite the SEI formation peak starting from 0.8 V vs. Li/Li+ looks slightly weaker, which indicates less electrolyte decomposition. Compared to Super C65, the low surface area of conductive graphite is depressing SEI growth. The CV curves for the fifth cycle (Figure 30b) show two reduction peaks at 0.2 V and 0.1 V vs. Li/Li+ for conductive grahite, which do not appear on Super C65 electrodes. The peaks correspond to the intercalation of Li into graphite, i.e. the formation of Li_xC_6 compounds [127]. The sharp oxidation peaks at 0.25 and 0.3 V vs. Li/Li+ correspond to lithium extraction. These peaks are hardly expressed on the curve of Super C65. Clearly, conductive graphite is involved in the electrochemical redox process. It not only improves electronic conductivity, but also contributes to the capacity and energy density of Si/MC composite electrodes.
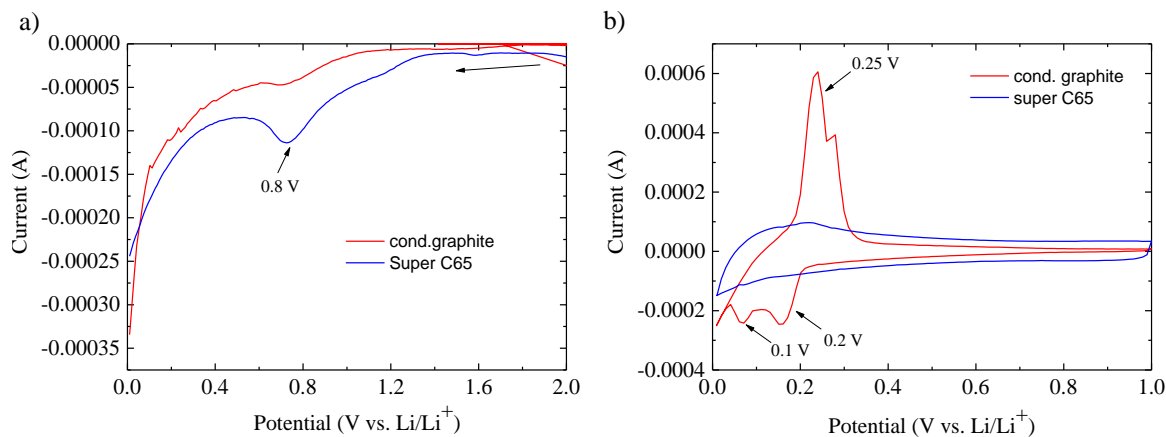
Figure 30. Cyclic voltammogram of conductive graphite and Super C65 at a scan rate of 20 µVs^{-1} over the potential window of (0.01–1)V vs. Li/Li$^+$ at 1st (a) and 5th cycle (b).

4.2.4   The effect of conductive additives (super C65 vs graphite) on the morphology of Si/MC electrodes

The morphology of the Si/MC/CB65 and Si/MC/G electrodes was compared by SEM analysis, presented in Figure 31. The fresh Si/MC/CB65 electrode exhibits an uneven and rough surface. The aggregates of Super C65 might result an inhomogeneous slurry which had an impact on the morphology of the electrodes. SEM analysis was also conducted on the electrodes after cycling in order to investigate any changes in the morphology of the particles during the intercalation and de-intercalation processes. It can be seen that Si/MC/CB65 after 200 cycles (Figure 31b) has similar morphology. The fresh Si/MC/G electrode (Figure 31c) has a more even and uniform surface than the fresh Si/MC/CB65 electrode. The smaller particle size range of the conductive graphite resulted a more homogeneous slurry and coating. After 200 cycles, the Si/MC/G (Figure 31d) electrode has bigger particles and white color. The white color appeared can be caused by a low conductivity of cycled Si/MC/G when it was scanned by electron beams. The less structure changes on Si/MC/CB can be explained by the chain-like, highly elastic structure of Super C65, which improves its cycling stability.

60
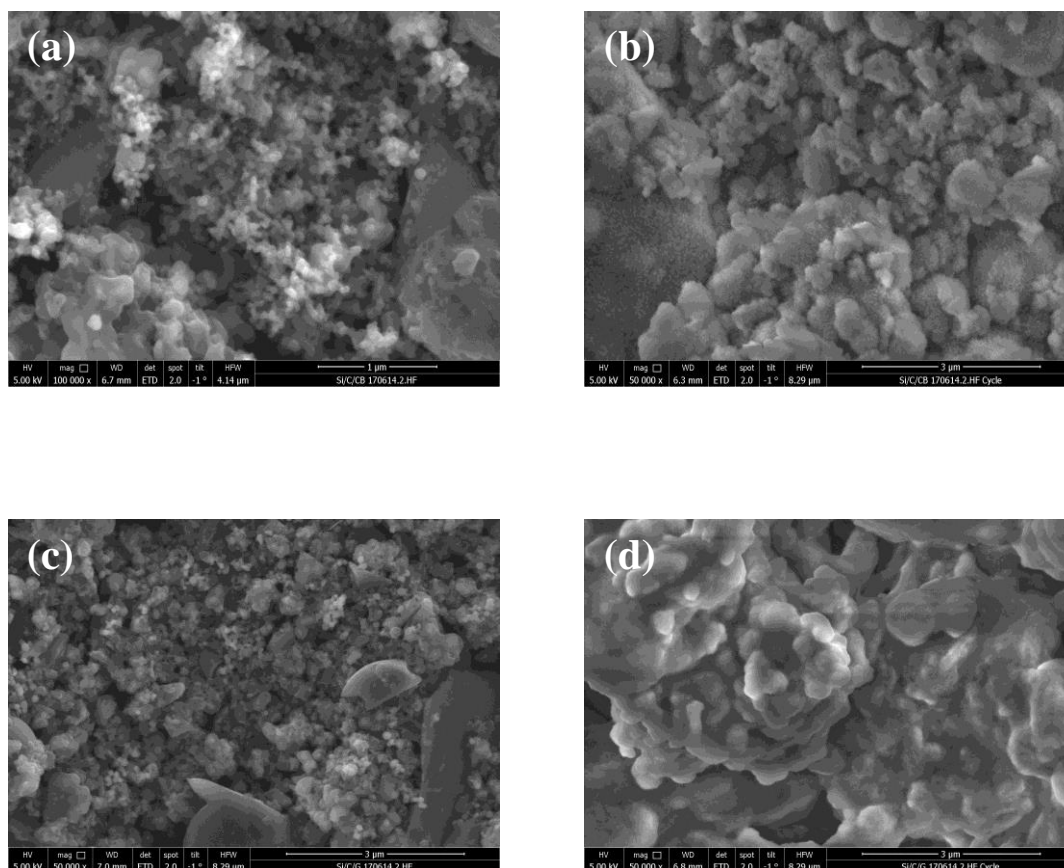
Figure 31. SEM images of the Si/MC/CB65 before cycling (a) and after cycling (b), Si/MC/G before cycling (c) and after cycling (d).

In-depth investigation of the effect of conductive additive structures on stress absorption during volume expansion and of the morphology of Si/MC/CB65 and Si/MC/G before and after cycling was carried out by TEM analysis, presented on Figure 32(a-d). TEM images were taken from thin film electrode samples which were prepared via FIB cross-section. According to Electro energy loss spectroscopy analysis, the Si/MC/CB65 electrode before cycling (Figure 32a) reveal that Si appears in dark grey with a size of 50 nm, the amorphous carbon layer in light grey and Super C65 in small dark dots. X-ray analysis revealed an amorphous structure of Si/MC/CB65 after cycling (Figure 32b), but the particles are still connected to each other. Fresh Si/MC/G electrodes (Figure 32c) look similar like Si/MC/CB65 in Figure 32a. However, the Si/MC/G electrode after cycling (Figure 32d) has more cracks. A stable SEI formed on the Si/MC/CB65 electrode is expected to prevent continual rupturing.
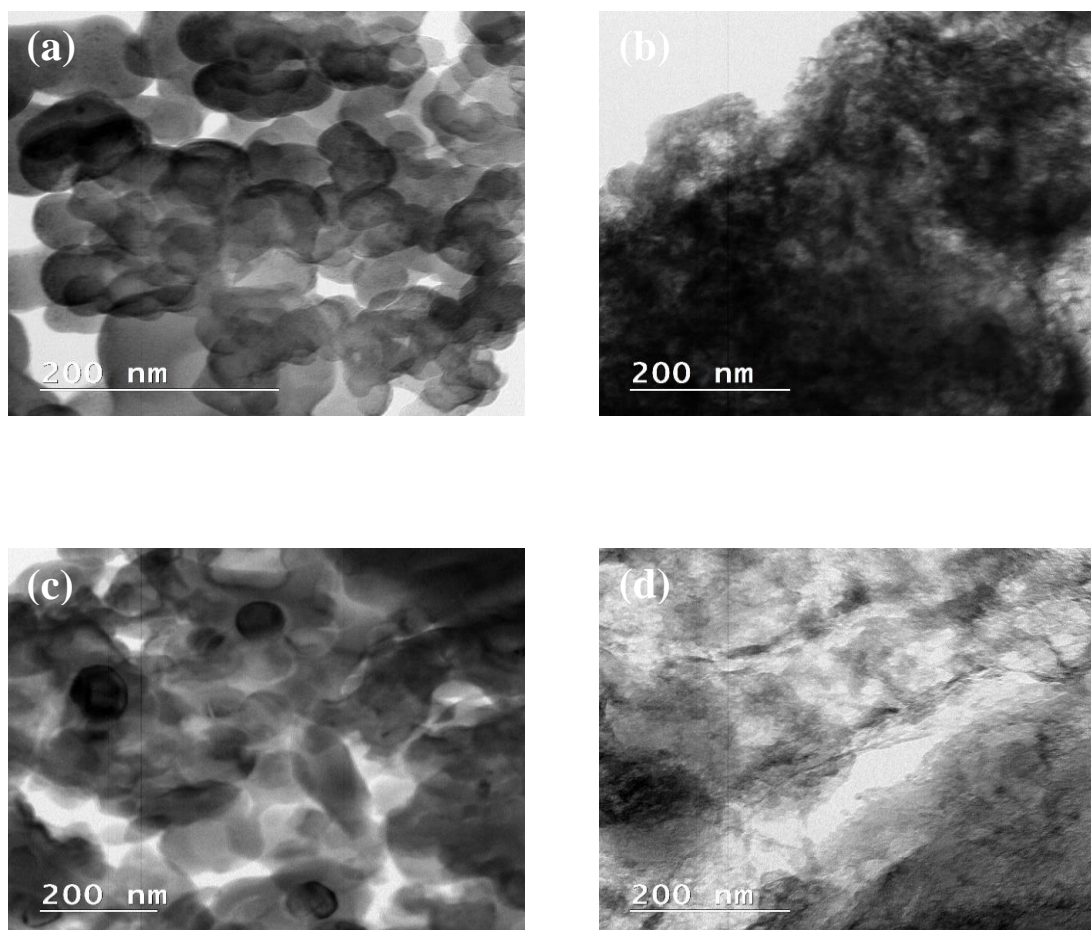
Figure 32. TEM images of a thin slice prepared via FIB cross-section of the Si/MC/CB65 before cycling (a) after cycling (b), Si/MC/G before etching (c) and after cycling (d).

Figure 33 shows the measured pore size distribution of the Si/MC/CB65 and Si/MC/G electrodes. A mean pore radius of 3.786 nm and 90.808 nm for Si/MC/CB65, 3.845 nm and 111.620 nm for Si/MC/G electrodes, was obtained. By integrating the area under the curve, the pore volumes of 0.244 cm^3g^{-1} for Si/MC/CB65 and 0.081 cm^3g^{-1} for Si/MC/G electrodes, respectively, were obtained.
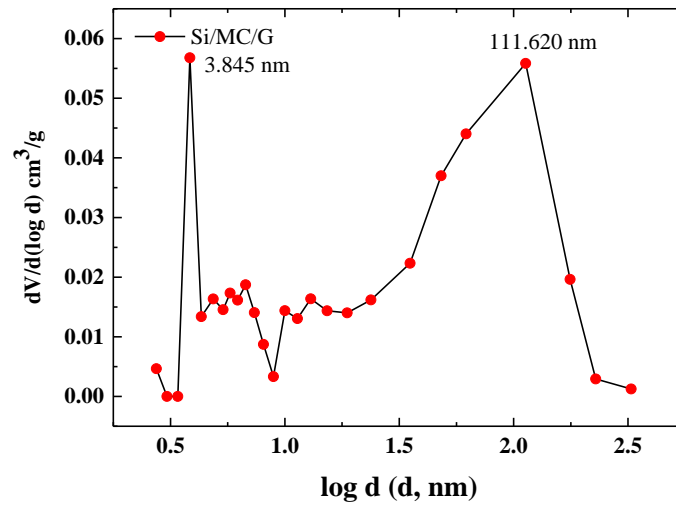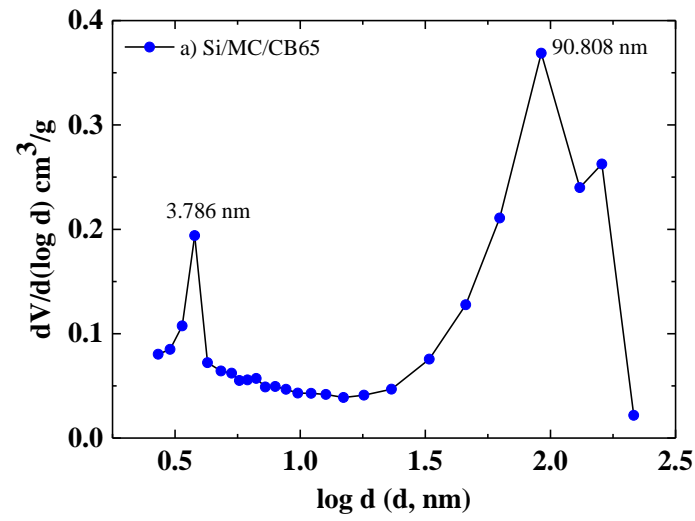
Figure 33. Pore size distribution of the Si/MC/CB and Si/MC/G electrodes.

The physicochemical properties of both electrodes were summarized in Table 12. Porosity of the electrodes was calculated by dividing measured pore volume by total volume by following equation:

$$\text{Porosity} = V_p/V_{total} \tag{16}$$

Vp is the pore volume measured by N_2 adsorption/desorption (in cm^3g^{-1}). V_{total} is calculated from the dimension of the electrode excluding the current collector (in cm^3), then divided by the mass of active material (in g). The Si/MC/CB and Si/MC/G electrodes have a porosity of 52.53% and 32.50%, respectively. Both values are higher than 30% which is typically applied in real cells. Lower porosity in Si/MC/G can be ascribed to the high crystallinity of conductive graphite which may cause the high compressibility of the electrodes.

Table 12. The physicochemical properties of Si/MC/CB65 and Si/MC/G electrodes

Electrode	Mean pore size diameter (nm)	Pore volume (cm^3g^{-1})	Porosity (%)
Si/MC/CB65	1.786 and 90.808	0.244	52.53
Si/MC/G	3.845 and 111.620	0.081	32.50

4.2.5 Electrochemical performance of Si/MC with conductive additive

The electrochemical lithiation/delithiation characteristics of the Si/MC electrodes with different conductive additives were assessed using CV. Figure 34 shows CV curves for Si/MC/CB45. A virtually constant reduction current starting from 1.0 V vs. Li/Li+ in the first cycle can be attributed to the formation of an SEI layer. The peak appearing at 0.2 V vs. Li/Li+ in the following cycles corresponds to the formation of Li_xSi alloys via a multi-stage mechanism. Obrovac et al. studied the lithiation and delithiation in crytalline silicon powder, shown in Table 13 [34].
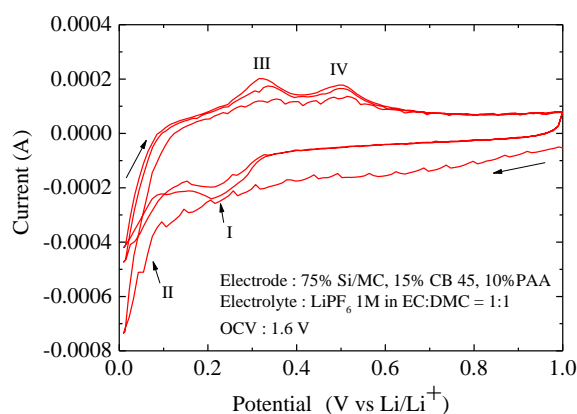
Figure 34. Cyclic voltammogram of Si/MC/CB45 at a scan rate of 20 μVs^{-1} over the potential window of (0.01–1) V vs. Li/Li+.

Table 13. The identification of peak in the voltage curve of silicon powder anode [34].

Lithiation	I (~0.2 V)	High-voltage lithiation of amorphous silicon (α-Si + x'Li $\rightarrow$ α-Li$_{x'}$Si)
	II (~ 0.1V)	Low-voltage lithiation of amorphous silicon (α-Li$_{x'}$Si + x''Li $\rightarrow$ α-Li$_{(x'+x'')}$Si
Delithiation	III (~0.35 V)	Low-voltage delithiation of amorphous silicon α-Li$_{(x'+x'')}$Si $\rightarrow$ α-Li$_{x'}$Si + x''Li
	IV (~0.5 V)	High-voltage delithiation of amorphous silicon α-Li$_{x'}$Si $\rightarrow$ α-Si + x'Li)

Figure 35a&b present CV curves for Si/C/CB65 and Si/MC/G. Compared to CV curves of Si/MC/CB45 (Figure 34), similar patterns can be seen for CV of Si/MC/CB65. On the other hand, the Si/MC/G electrode (Figure 35b) exhibited a different profile. However, a similar reduction current within the 1st cycle, starting from 1.0 V vs. Li/Li+, corresponds to the initial formation of an SEI layer. Two reduction peaks appear at 0.2 V and 0.1 V vs. Li/Li+. The peaks correspond to the intercalation of Li into graphite, i.e. the formation of Li$_x$C$_6$ compounds [127], and the intercalation of Li into silicon to Li$_x$Si alloys. Three peaks appear at 0.2 V, 0.3 V, and 0.5 V vs. Li/Li+ at oxidation process. At 0.2 and 0.3 V vs. Li/Li+, the lithium extraction from Li$_x$C$_6$ take place, as agreed with the CV of pure graphite on Figure 30b. While, the peaks 0.35 and 0.5 vs. Li/Li+ correspond to the lithium extraction from α-Li$_x$Si

a)

b)
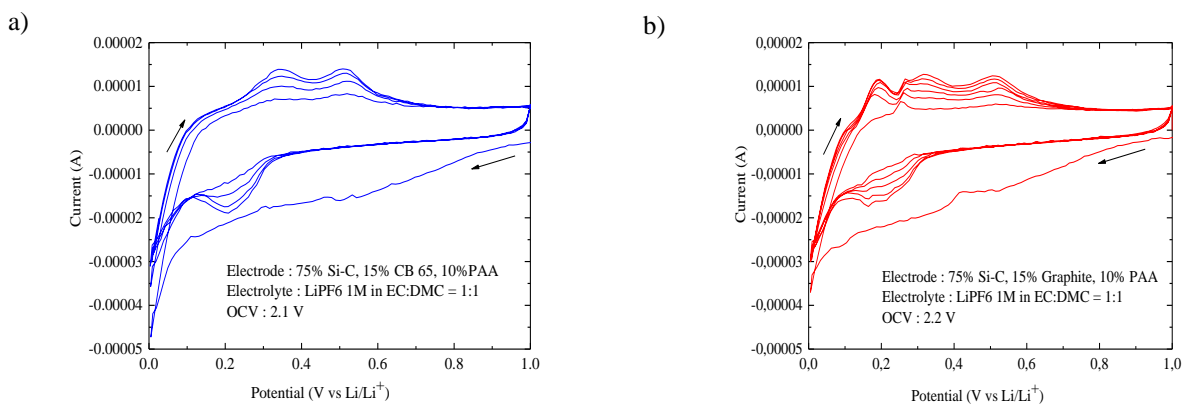
Figure 35. Cyclic voltammogram of Si/C/CB65 (a) and Si/MC/G (b) at a scan rate of 20 µVs^{-1} over the potential window of (0.01–1) V vs. Li/Li+.

In order to examine the cyclability performance of the electrodes, charge-discharge tests were conducted from 1 to 0.01 V at C/10 for the first cycle and 1C for the following cycles. Figure 36a shows the curves of gravimetric discharge capacity versus cycle number of Si/MC electrodes with different conductive additives. The Si/MC/G electrode reveals an initial reversible capacity of over ~3220 mAh g^{-1} and maintains a reversible capacity of 380 mAh g^{-1} after 100 cycles. The Si/MC/CB65 electrode reveals an initial reversible capacity of ~2900 mAh g^{-1} and maintains a high reversible capacity of ~ 760 mAh g^{-1} after 100 cycles. The capacity fading from cycle to cycle can be assigned to a successive destruction of the electrodes by longer cycling, which is confirmed by SEM and TEM images in Figure 32. The Si/MC/CB45 electrode exhibits an initial specific capacity of 3720 mAh g^{-1} and reversible capacity of 458 mAh g^{-1}. The Si/MC composite with the combination of conductive graphite and super C45 exhibited 2400 mAh g^{-1} and ~420 mAh g^{-1}.

Figure 36b shows the curves of columbic efficiency versus cycle number of Si/MC electrodes with different conductive additives. The Si/MC/G electrode reveals an initial coulombic efficiency of 52.99%. A significant amount of charge of 47.01% was consumed for the SEI formation during the 1st cycle, which took place at potential < 0.85 V. The CE of Si/MC/G electrode decreases after first cycle until 50 cycles and increases gradually during the following cycles. The Si/MC/G exhibits the average CE of 96.95% over 100 cycles. The initial coulombic efficiency of Si/MC/CB65 and Si/MC/CB45 is 20.60% and 40.87%, respectively. In general, a higher amount of charge has been consumed for SEI formation in the Si/MC electrode with carbon black compared to the Si/MC with conductive graphite. This is because carbon black have higher specific surface area than graphite. Compared to the specific surface area on Table 11 (Super C65 > Super C45 > graphite), differences in the specific surface areas cause an increasing initial capacity loss of the electrodes (Si/MC/CB65 > Si/MC/CB45 > Si/MC/G).

The Si/MC/CB65 and Si/MC/CB45 maintain the average CE of 97.44% and 98.76%, respectively. Carbon black particles which are attached at the surface of the active material can absorb and retain electrolyte. This attachment may allow an intimate contact between the lithium ions and Si nanoparticles. The Si/MC/CB45 electrode exhibits both a higher initial and average coulombic efficiency over 100 cycles. The stability of the SEI layer helps the Si/MC with carbon blacks electrode to achieve higher average coulombic efficiency.

A Si/MC composite with the combination of conductive graphite and super C45 was also investigated. The electrode exhibited an initial columbic efficiency of 49.26% and average CE of 97.84% over 100 cycles. Carbon black improves the contact between particles of active material, whereas graphite creates the conductive path through the electrode. It is observed that some CEs in Figure 36b sometimes exceed 100%. Which may be due to "accumulated" lithium from preceeding cycles. This means that some residual Li stored in the previous cycles can be extracted additionally. These phenomena can be due to the continous changes of SiNPs which cause some fluctuation in ionic and electric conductivities from cycle to cycle. Thus, the varying arrangement of Si nanoparticles also can cause fluctuations in the capacities leading to a "virtual" CE greater than 100%. The summary of the electrochemical performance of Si/MC electrodes with different conductive addtives is given in Table 14.

Table 14. The electrochemical performance of Si/MC with different conductive additives.

Electrode	Initial discharge capacity	Discharge capacity at 100th cycles	Initial CE	Average CE over 100 cycles (without 1st cycle)
Si/MC/G	3220 mAhg^{-1}	381 mAhg^{-1}	52.99%	96.95%
Si/MC/CB65	2899 mAhg^{-1}	764 mAhg^{-1}	20.60%	97.44%
Si/MC/CB45	3088 mAhg^{-1}	459 mAhg^{-1}	40.87%	98.76%
Si/MC/C&G	2401 mAhg^{-1}	428 mAhg^{-1}	49.26%	97.84%
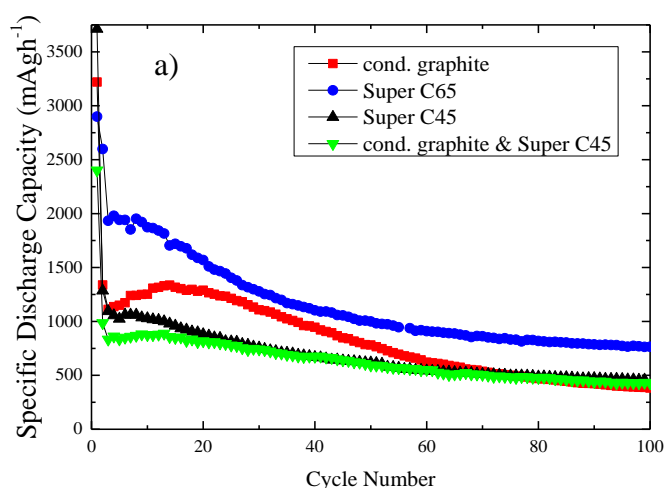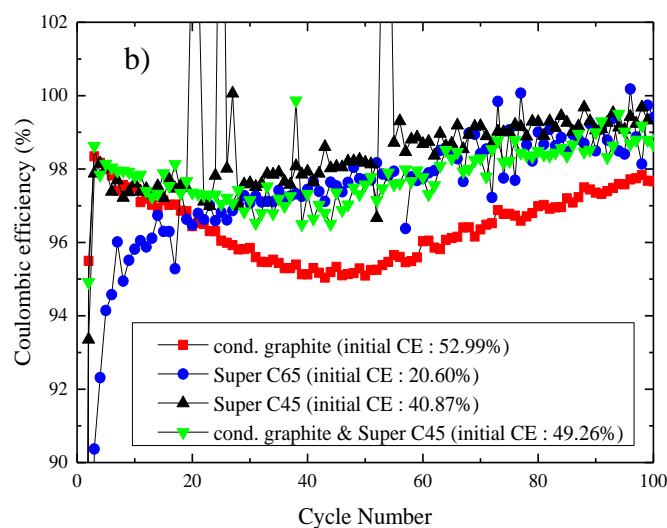
Figure 36. Charge/discharge test (a) and columbic efficiency (b) of Si/MC with different conductive additives under charge/discharge cycles from 1 to 0.01 V with a charge/discharge current of 1C.

4.2.6 Electrochemical Impedance Spectroscopy (EIS)

To verify the effect of the conductive additives on the charge transfer resistance, EIS has been carried out for all electrodes at 0.05 V vs. Li/Li+ after the first lithiation. As presented in Figure 37, the EIS curve is composed of small intercept in the high frequency region (500 kHz), a semicircle at the medium frequency region (100 kHz to 200 mHz), and a straight sloping line at the low frequency (<200 mHz). Such a pattern of EIS can be fitted by an equivalent circuit as shown in Figure 37b. The small intercept corresponds to the ohmic resistance, representing electrolyte resistance (Re), as well as any contact resistances of the current collectors and electrode materials [128]. The semicircles appearing in the medium frequency represents charge–transfer resistance (Rct) and double-layer capacitance (Cdl). The straight sloping line is related to Warburg impedance (W) which is associated with lithium ion diffusion in the active particles.

The proposed fitting results of each EIS parameter are presented in Table 16. It can be seen that the electrodes have distinct Re and Rct. Re which is related to the ohmic drop depends on the current distribution in the electrolyte and the geometry of the electrode. The larger Re of Si/MC/CB65 can be assigned to the less homogeneous surface, which is agreed well

68

with SEM image in Figure 37a. Guo et al. proposed that the value of Rct for the anode of a lithium ion batteries reflects the compaction of particles in the composite anodes or inter-particle contacts [129]. Compared to other electrodes, the Si/MC/CB65&G has smallest first depressed semi circle which correspond to the smallest Rct. It is attributed by the combination of both super C65 and graphite. The small particle size of carbon black may improve the charge transfer interparticles and graphite improves the compaction of the particles of the electrode.
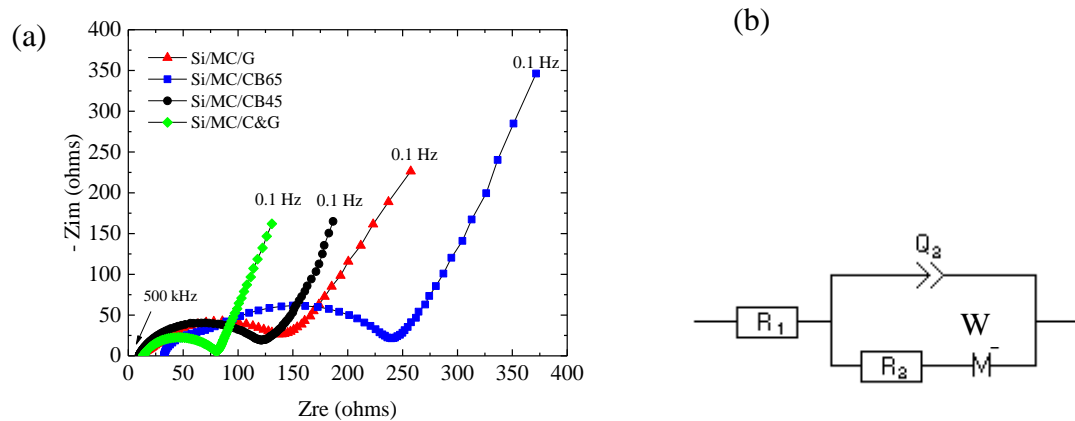
Figure 37. Nyquist plot of Si/MC with different conductive additives at discharged potential of 0.005 V vs. Li/Li+ from the first cycle from 500 kHz to 100 mHz (a) electrical circuit (b).

Table 15. Re andn Rct of Si/MC with different conductive additives at discharged potential of 0.005 V vs. Li/Li+ from the first cycle.

Electrode	Si/MC/G	Si/MC/CB65	Si/MC/CB45	Si/MC/C&G
Re (ohms)	13.5	28.2	9.8	13.9
Rct (ohms)	65.04	193.4	98.3	61.5

In addition to the electronic conductivity, high ionic conductivity is required for building a better cell. Solid state diffusion and migration of lithium ions are the keys to advancing Li ion batteries [130]. Thus, it is interesting to compare Li-ion diffusion coefficient (D_{Li}) in Si/MC with different conductivities. Ding et al. determined D_{Li} in nano-Si by using cyclic voltammetry (CV), electrochemical impedance spectroscopy (EIS), galvanostatic intermittent titration technique (GITT) [131]. While Dokko et al. applied CV and EIS on mesocarbon microbead [132]. So far, there is limited study on the Li-ion diffusion in silicon/mesoporous carbon. In this work, the D_{Li} was examined by using EIS method from the Warburg part according to equation (17) proposed by Ho et al. [133]:

69

$$D_{Li^+} = \frac{1}{2}\left[\left(\frac{V_M}{SFA}\right)\left(\frac{\delta E}{\delta x}\right)\right]^2 \qquad (17)$$

Where V_M is the mole volume of silicon, S is the surface area of the electrode (1.766 cm² was calculated from the area of the electrode for simplicity), F is the Faraday constant (96,486 C mol⁻¹), A is the plot slope of imaginary resistance (Z_{im}) vs. inverse square root of angular frequency $(1/\sqrt{2\eta f})$ which is obtained from the Warburg impedance, and ($\delta E/\delta x$) is the slope of galvanostatic charge-discharge curves, x is the composition in Li_xSi. Figure 38 shows the galvanostatic charge-discharge curves of Si/MC with different conductive additives. The presence of two regions indicates that x in α-Li_xSi does not change smoothly.
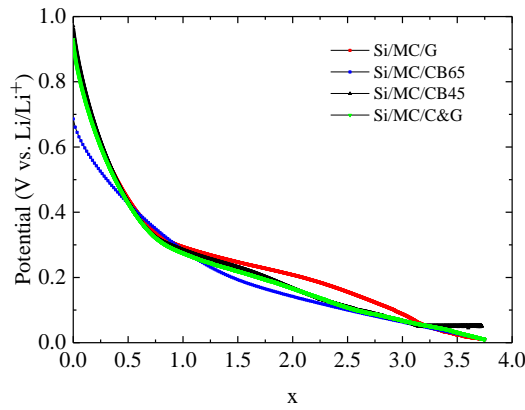
Figure 38. The galvanostatic discharge curves of Si/MC with different conductive additives.

From the XRD analysis, Si nanoparticles are found to be crystalline. The lattice distance of Si nanoparticles (111) can be calculated from the diffraction pattern to be 3.13 Å. While silicon has a cubic symmetry (Z = 8), the unit cell parameter can be calculated by (V_{cell} = $\sqrt{3}\,(3.13\text{Å}) = \sqrt{3}\,(3.13\text{Å}) = 5.42$ Å). Molar volume (V_M = 11.99 cm³mol⁻¹) was calculated by following equation :

$$V_M = \frac{N_A V_{cell}}{Z} \qquad (18)$$

To obtain the Warburg coefficient (A), the linear fitting of Zim vs. $\omega^{-1/2}$ in the low frequency region was done, which can be seen in Figure 39.
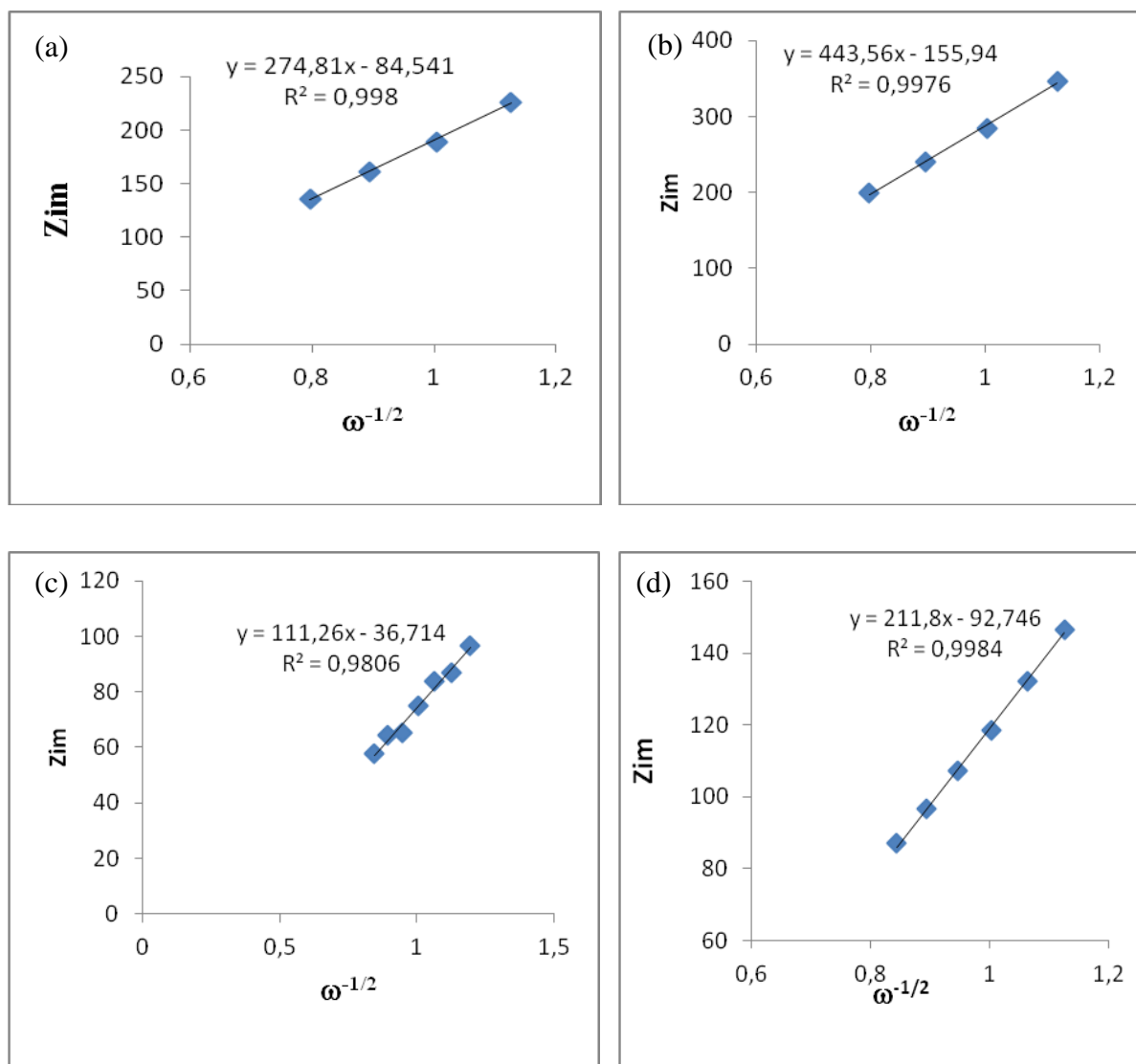
Figure 39. The relationship between Zim and $\omega^{-1/2}$ at low-frequency region of the Si/MC/G (a), Si/MC/CB65 (b), Si/MC/CB45 (c), and Si/MC/G&CB (d).

Table 16. Warburg coefficient (A) and diffusion coefficient of Si/MC with different conductive additives.

Electrode	Si/MC/G	Si/MC/CB65	Si/MC/CB45	Si/MC/C&G
δ	274.81	443.56	111.26	211.8
D_{Li} (cm^2 s^{-1})	3.30 10^{-16}	1.26 10^{-16}	1.97 10^{-15}	5.56 10^{-16}

All values of the calculated diffusion coefficient of lithium ions are lower than the reported diffusion coefficient of lithium ions in SiNPs (10^{-14}–10^{-13} cm²s⁻¹) [131]. To be noted that this calculation is based on the 1st cycle, thus, it gives much lower than the reported the diffusion coefficient. However, these results can be taken as additional consideration for selecting the proper conductive additive for Si/MC electrodes. The higher D_{Li} of Si/MC/CB45 electrode, compared another electrodes, indicates faster kinetics of the cell reactions. In the composite electrode, the Li-ion diffusion is governed mostly by the pore distribution which controls electrolyte access to the active material [131]. One of the barriers to calculate the D_{Li} is the difficulty to measure the real surface area of the active material on the electrodes. The Si/MC/CB45 electrode was used for further optimization due to its higher coulombic efficiency over 100 cycles and faster kinetics.

4.2.7 Conclusion

An investigation of various conductive additives for Si/MC electrodes was performed. Structural, morphological, and electrochemical characterization of the electrodes indicated several differences between Si/MC with conductive graphite and with carbon black (Super C65 and Super C45). The morphological characterization showed that the smaller particles of Super C65 combined with the complex aggregate structure resulted in an Si/MC/CB65 electrode with less homogeneous surface compared to the Si/MC/G electrode. Electrochemical tests showed that the highly structured conductive additive had a double function: as an enhancer of conductivity and as an active electrode component. In spite of its higher specific area, Super C65 presented the Si/MC electrodes with better cyclability than conductive graphite. However, the use of Super C45 can minimize the initial charge loss of Si/MC electrode better than Super C65.

4.3 The selection of electrolyte additives for Si/MC anodes

Although volume expansion can be minimized by the dispersion of nanostructured Si in the carbon network and the conductivity problem can be overcome by the conductive additives, some issues related to the initial capacity loss are still present. A prevalent strategy for dealing with this problem is the use of electrolyte additives. This third subchapter will focus on the investigation of the electrolyte additives for Si/MC electrodes. Despite the high performance of vinyl carbonate (VC) which have been reported [24], [87]–[92], however, VC is difficult to synthesize and expensive (~416 EUR/25 grams). Thus, succinic anhydride (SA) (~14 EUR/25 grams) and lithium bis(oxalato)borate (LiBOB) (~120 EUR/25 grams) were investigated as electrolyte additive and compared with VC. The beneficial roles of those aforementioned electrolyte additives on the Si electrode/electrolyte interfaces have been demonstrated [96][134]. However, there is no comparative study on the effects of LiBOB,

SA, and VC so far. In addition, most previous studies regarding these electrolyte additives focus on the Si thin film which might behave differently from Si nanoparticles-based anodes.

The study was divided into; (i) electrochemical performance of Si/MC electrodes with different electrolyte additives, (ii) dV/dQ analysis and (iii) XPS analysis of SEI layer on Si/MC anodes with electrolyte additives. The electrodes were prepared by mixing the Si/MC composites (75 wt%), Super C45 (15 wt%), PAA (10 wt%) and dissolved in NMP solvent. The previous results showed that the electrodes with this composition exhibited the least initial charge loss of Si/MC electrode and performed faster Li-ion diffusion. 1M LiPF$_6$ in 1:1 vol mixture EC and DMC without additive was used as standard electrolyte. The composition of the standard electrolyte and electrolyte with different electrolyte additives can be seen in Table 5.

The composition of the standard electrolyte and electrolyte with different concentrations of VC additive is given in Table 6.

4.3.1 Electrochemical performance of Si/MC electrodes with different electrolyte additives

The discharge capacity versus cycle number curve of Si/MC electrodes with different electrolyte additives is presented in Figure 40a. The experiment with standard electrolyte (red curve) shows an initial discharge capacity of 3487 mAhg^{-1} which decreases to 692 mAhg^{-1} at 100 cycles. The decrease in capacity at the first several cycles is attributed to the decomposition of electrolytes and the formation of the SEI. Over cycles the discharge capacity shows fluctuations which can be due to some changes in ionic and electric conductivities. On the other hand, the Si/MC electrodes with electrolyte additives show distinct SEI formation cycles and deliver a discharge capacity higher than the one with standard electrolyte. The electrode with 5wt% SA shows a decreasing discharge capacity from 3796 mAhg^{-1} to 807 mAhg^{-1} after 100 cycles. With the addition of 5wt% LiBOB, the electrode exhibits a higher initial charge loss of ~2461 mAhg^{-1}. However, it shows a stable discharge capacity after 20 cycles (~970 mAhg^{-1}). A previous study proposed that the decomposition reaction of LiBOB was relatively fast with respect to LiPF$_6$ and inhibited the continuous reactions of lithiated Si with the electrolyte [134]. Thus, LiBOB is more effective in forming a stable SEI layer.

Compared with other electrodes, the electrode with 5wt% VC has a more stable performance with a discharge capacity of 1100 mAhg^{-1} after 20 cycles which remains stable in the subsequent cycles. This distinct electrochemical performance may be related to the particular composition of SEI which is later discussed based on XPS analysis.

73

To check the irreversible capacity loss of the electrodes, columbic efficiency is compared in Figure 40b. The initial columbic efficiency of the electrode in standard electrolyte is 44.79% and shows fluctuations over the cycles. The electrode with standard electrolyte, SA, and LiBOB reach the stable CE of over 99% after 80 cycles. Meanwhile, the electrode with the VC additive reaches CE over 99% after around 20 cycles. It can be seen that with LiBOB, the discharge capacity decreases but the CE increases. This phenomenon can be explained by the thickening SEI layer which increases the internal resistance of the cell. Table 17 summarizes the discharge capacity and coulombic efficiency at the 1st and the 20th cycle for Si/MC electrodes with different electrolytes. The electrode with 5wt% VC exhibits a relatively high capacity retention and CE at 20th cycle.
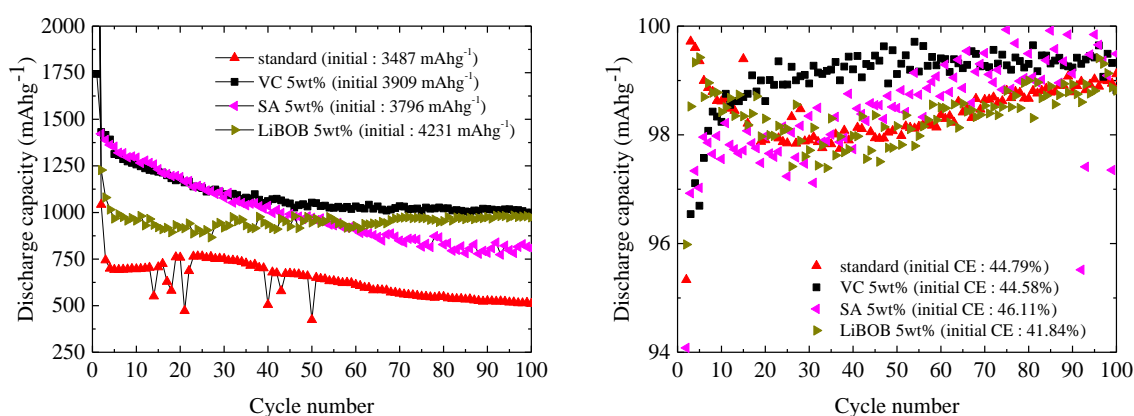
Figure 40. Electrochemical discharge capacity (a) and coulombic efficiency (b) vs cycle number of Si/MC electrodes with different electrolyte additives under charge/discharge cycles from 1 to 0.01 V with a charge/discharge current of C/10.

Table 17. Electrochemical performance of Si/MC electrodes with different electrolytes at 1st and 20th cycles.

Electrolyte additive	Discharge capacity 20th cycle	Capacity retention at 20th cycle	Coulombic efficiency at 20th cycle
standard	758 mAhg^{-1}	21.73%	97.91%
5wt% VC	1193 mAhg^{-1}	30.52%	98.62%
5wt % SA	1189 mAhg^{-1}	31.32%	97.98%
5wt% LiBOB	919 mAhg^{-1}	21.72%	98.30%

The stability of the electrodes was assessed by rate capability tests. Figure 41 shows the capacity vs. cycle number at various C-rates. The average discharge capacity for this test can be seen in Table 18. Discharge capacity gradually decreases with increasing C-rate from C/10 to 2C and increases again when C-rate is lower. Upon cycling, the experiment with the standard electrolyte shows a relatively poor rate capability. At C/10, the discharge capacity of the electrode is ~1880 mAh.g^{-1} and 750 mAh.g^{-1} for 2nd and 110th cycle, respectively. On the other hand, the addition of 5wt% VC affected a higher rate capability than SA and LiBOB. The experiment with 5wt% VC shows ~1500 mAh.g^{-1} at 2nd cycle and maintains at ~1100 mAh.g^{-1} at 110th cycle.

The columbic efficiency at various C-rate was also calculated and depicted in Figure 41b. After 20 cycles, all electrodes reach a high CE of >96%. After 110 cycles at C/10, the CE of the electrodes with standard electrolyte, VC, SA, and LiBOB reaches 97.34%, 99.34%, 98.98%, and 98.50%, respectively. These results confirm that the addition of 5wt% VC improves the electrochemical performance more than the other electrolyte additives. It is interesting that some CE`s are greater than 100% for the electrode with standard electrolyte. These phenomena can be due to the continuous changes of SiNPs which cause some fluctuation in ionic and electric conductivities from cycle to cycle. Thus, the varying arrangement of Si nanoparticles also can cause fluctuations in the capacities by casual charge retention or release leading to a "virtual" CE greater than 100%. It other words, some residual Li stored in the previous cycles can be released additionally in following cycles. This noticeable phenomenon was also observed in the Si nanoparticles wrapped by a carbon shell by Hwang et al [41].

Figure 41. Rate capability (a) and columbic efficiency (b) vs. cycle number of Si/MC electrode with different electrolyte additives at various C-rate (C/10, C/5, C/2, C/3, 1C, 2C).

Table 18. Average capacity of Si/MC electrode with different electrolyte additives at various C-rate (C/10, C/5, C/2, C/3, 1C, 2C).

Electrolyte additive	Average discharge capacity (mAhg^{-1})						
	C/10	C/5	C/3	C/2	1C	2C	C/10
standard	1881	1375	1106	925	753	567	812
5 wt% VC	1718	1332	1164	1032	903	683	1082
5wt % SA	1777	1235	985	830	616	448	957
5wt% LiBOB	1657	1184	995	859	645	508	928

In order to investigate the electrochemical behavior in more detail, differential capacity (dQ/dV) analysis has been performed. The dQ/dV vs. voltage plots for Si/MC electrodes with various electrolytes at 1st, 2nd, 110th cycles are presented in Figure 42. In particular, the peaks at 1st cycle indicate the potential at which the additives initially are reduced. The broad cathodic peak at ~0.6 V vs. Li/Li+ during 1st cycle (Figure 42a) which disappears on 2nd and 110th cycles (Figure 42b&c) may be attributed to the electrolyte decomposition and SEI formation. The reduction of the standard electrolyte starts at 1.0 V vs. Li/Li+ and shows a cathodic maximum at ~ 0.6V vs Li/Li+. This reduction starts at a different potential with SA (1.15 V vs Li/Li+) and LiBOB (1.2 V vs. Li/Li+). With VC as an additive, the starting potential is slightly shifted to a lower value (0.8 V vs. Li/Li+). This indicates a higher overpotential which is attributed to increased resistance in the SEI [135]. For the LiBOB containing electrolyte, another reduction peak appears at a much more positive potential of 1.7 V vs. Li/Li+. Previous study demonstrated that the reduction of the BOB-anion to oxalate occurred at a high potential (> 1V) and did not contribute to the formation of SEI layer on the graphite anode [136]. This reduction may explain why the electrode with LiBOB exhibited an initial charge loss higher than those with other electrolyte additives (~2461 mAhg^{-1} at first cycle).

The cathodic peak at ~0.1 V can correspond to the lithiation of crystalline Si. Obravac et al. reported that the anodic peak at ~0.45 V vs. Li/Li+ is the dQ/dV signature of Li$_{15}$Si$_4$ phase during delithiation [34]. The presence of the Li$_{15}$Si$_4$ was originally identified by XRD, and then confirmed by in situ HRTEM [40]. The presence of Li$_{15}$Si$_4$ was associated with capacity fading due to inhomogeneous volume changes. While, Chevrier et al. suggested that the

magnitude and the sharpness of the peak could be a measure of the $Li_{15}Si_4$ phase at full lithiation [137]. In Figure 42a, the presence of $Li_{15}Si_4$ (anodic peak at ~0.45 V vs. Li/Li+) is easily identifiable by dQ/dV, especially for the Si/MC electrode with standard electrolyte. It can be noted that the electrode with 5wt% VC shows a slight shift of the peaks to a less positive potential for lithiation and to a more positive potential for delithiation which gives a hint to some kinetic hindrance.

The dQ/dV plots for the following cycles are different from the first cycle. During the 2nd cycle (Figure 42b), all the electrodes have two peaks at 0.25 V vs. Li/Li+ and 0.1 V vs. Li/Li+. These peaks correspond to the stepwise lithium insertion into amorphous silicon forming amorphous Li_xSi ((α-Si + x'Li → α-$Li_{x'}$Si) and (α-Li_xSi + x''Li → α-$Li_{(x'+x'')}$Si) [34]. At 110th cycle after applying high C-rate (Figure 42c), the intensity of the peaks at 0.25 V at lithiation and 0.5 V vs. Li/Li+ at delithiation significantly decreased. This indicates the $Li_{15}Si_4$ phase gradually decomposes with cycling. All electrodes show the decreasing intensity of the peaks at 0.25 V vs. Li/Li+ and 0.1 V vs. Li/Li+ during lithiation which means the less insertion of lithium into amorphous silicon. In addition, compared to the 2nd cycle, the electrodes at the 110th cycle show significant peak shifts towards lower voltage for the lithiation and towards higher voltage for the process of delithiation which can be assigned the increasing overpotential. The increasing overpotential between delithiation and lithiation voltages with during the cycling is assigned to a loss of kinetic activity. Contrary to the electrode with standard electrolyte which shows the highest overpotential, the electrode with 5wt% VC exhibits lowest overpotential.
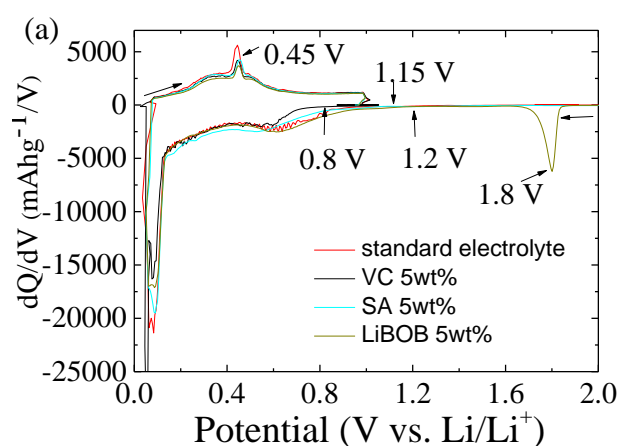
Figure 42. Differential capacity (dQ/dV) vs. potential plots of Si/MC electrodes with different electrolytes at (a)1st, (b) 2nd, and (c) 110th cycle.

4.3.2 Electrochemical performance of Si/MC electrodes with different concentrations of VC

Compared to LiBOB and SA, VC improved the electrochemical performance of Si/MC electrodes more effectively. As VC is relatively difficult to synthesize and expensive, the effective amount of VC is also interesting to investigate. Figure 43a shows the electrochemical discharge capacity vs. cycle number of the Si/MC electrodes with different amounts of VC. It shows that electrodes with VC additives regardless the concentrations exhibit a discharge capacity higher compared to that with standard electrolyte. It is interesting to see that increasing the amount of VC does not necessarily increase the discharge capacity. In fact, the electrode with 5wt% VC still shows the best electrochemical performance. However, the coulombic efficiency profile (Figure 43b) shows that the

electrode with 10wt% VC reaches ≥99% after 5 cycles. So far, there is no study about the effect of different concentrations of VC on Si/C-based composites.

(a)　　　　　　　　　　　　　　　　　　　　(b)
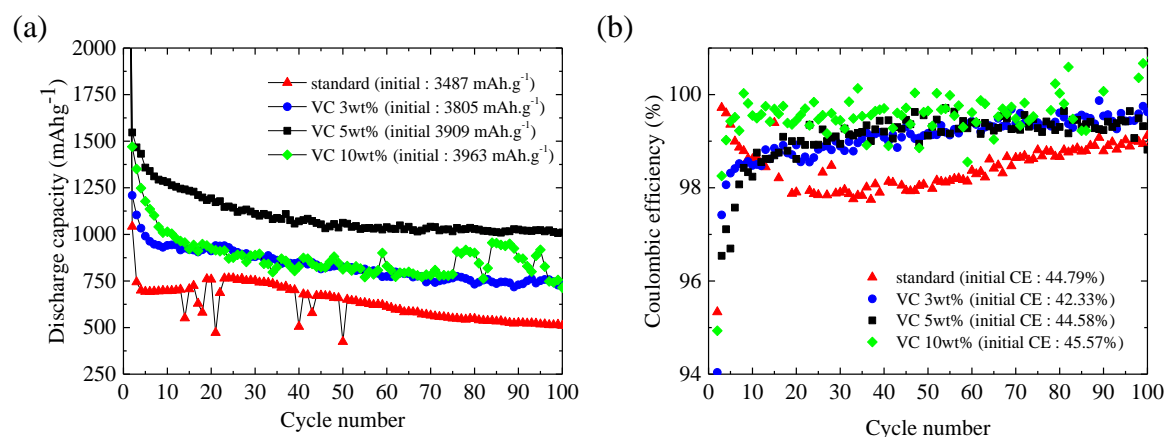
Figure 43. Electrochemical discharge capacity (a) and coulombic efficiency (b) vs cycle number of Si/MC electrodes with different amounts of VC under charge/discharge cycles from 1 to 0.01 V with a charge/discharge current of C/10.

Table 19. Electrochemical performance of Si/MC electrodes with different concentrations of VC at 1st and 20th cycles

Electrolyte additive	Discharge capacity 20th cycle	Capacity retention at 20th cycle	CE at 20th cycle
standard	758 mAhg^{-1}	21.73%	97.91%
3 wt% VC	911 mAhg^{-1}	23.94%	98.92 %
5 wt% VC	1193 mAhg^{-1}	30.52%	98.62%
10 wt% VC	918 mAhg^{-1}	23.16%	99.45%

Rate capability tests for the Si/MC electrodes with different concentrations of VC were also performed and can be seen in Figure 44a. The average discharge capacity from this rate capability test can be seen in Table 20. At C/10, the electrode with VC 3wt% exhibits ~1300 and ~750 for the 2nd and 110th cycles, respectively, while the electrode with 10wt% VC exhibits 1300 and 1000 mAhg^{-1} for the 2nd and 110th cycles, respectively. Compared to the electrode with 5wt% VC (1718 mAhg^{-1} and 1082 mAhg^{-1} for the 2nd and 110th cycles), the electrodes with 3wt% and 10wt% of VC showed less stable performance. The rate capability tests confirm previous results that the electrolyte with 5wt%VC shows better electrochemical performance than at other concentrations (3wt% and 10wt%). To be noted also from Figure 44b that the electrodes with VC additives reach CE values >98% after 20

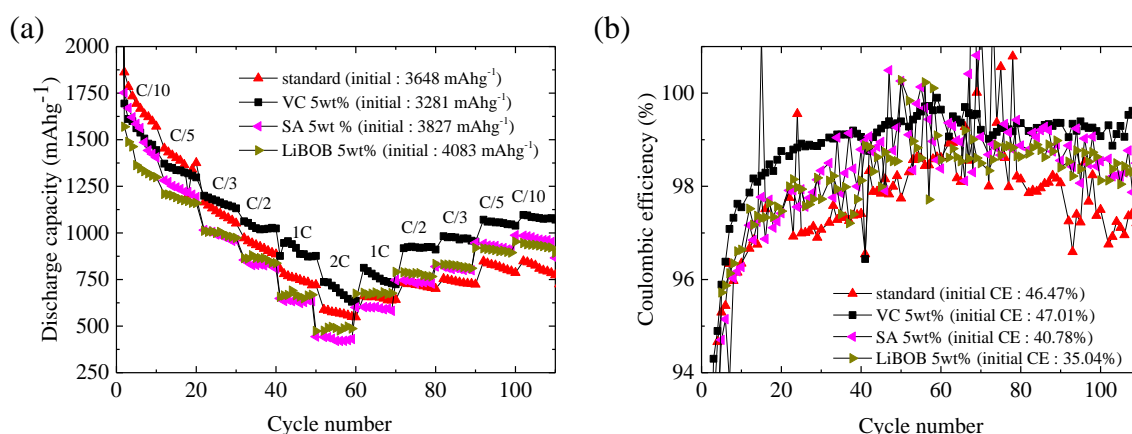cycles, while that with standard electrode shows coulombic efficiency below 98% upon cycling.
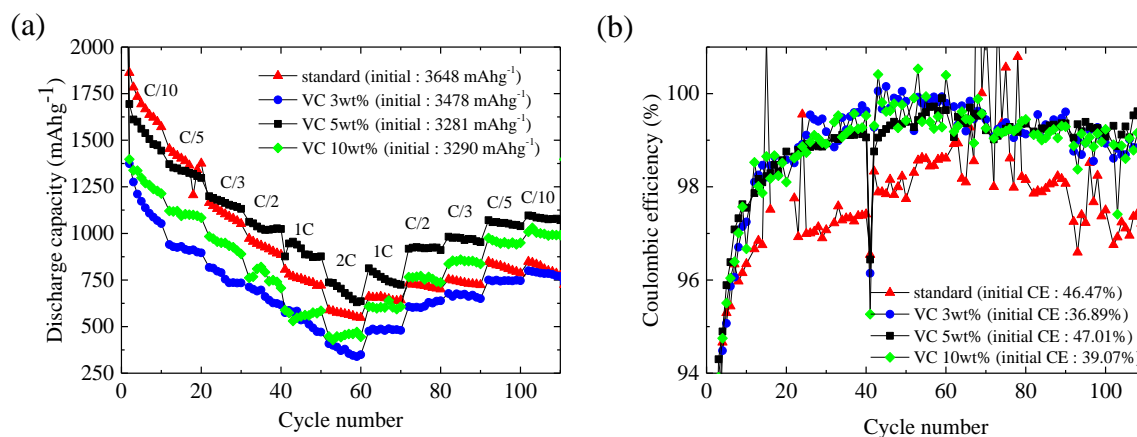
Figure 44. Rate capability (a) and columbic efficiency (b) vs. cycle number of Si/MC electrode with different concentrations of VC at various C-rate (C/10, C/5, C/2, C/3, 1C, 2C).

Table 20. Average capacity of Si/MC electrode with different concentrations of VC at various C-rate (C/10, C/5, C/2, C/3, 1C, 2C).

Electrolyte additive	Average discharge capacity (mAhg⁻¹)						
	C/10	C/5	C/3	C/2	1C	2C	C/10
standard	1881	1375	1106	925	753	567	812
3 wt% VC	1396	917	768	663	534	370	785
5 wt% VC	1718	1332	1164	1032	903	683	1082
10 wt% VC	1487	1103	940	765	564	450	1000

Differential capacity (dQ/dV) vs. potential plots of Si/MC electrodes with different concentrations of VC can be seen in Figure 45. The electrode with the VC 3wt% and 5wt% showed the initial decomposition starting at 0.8V vs. Li/Li+, lower than those with the standard electrolyte and VC 10wt% (0.9V vs. Li/Li+).

From the 2nd cycle (Figure 45b) to 110th cycle (Figure 45c), Si/MC electrode with standard electrolyte shows a shift of the reduction potential from 0.25 V vs. Li/Li+ to 0.2 V vs. Li/Li+. On the other hand, the electrodes with VC additives show no reduction potential shift. Their

reduction peaks remain at 0.25 V vs. Li/Li+. At 110th cycle, the peaks are less pronounced for the electrode with standard electrode and most pronounced with 5wt% VC. Hausbrand et al. reviewed that the degradation can be characterized by the irreversible capacity loss, voltage loss and increase in cell impedance [138]. Thus, it is concluded that the addition of 5wt% VC delivered the most stable electrochemical performance.
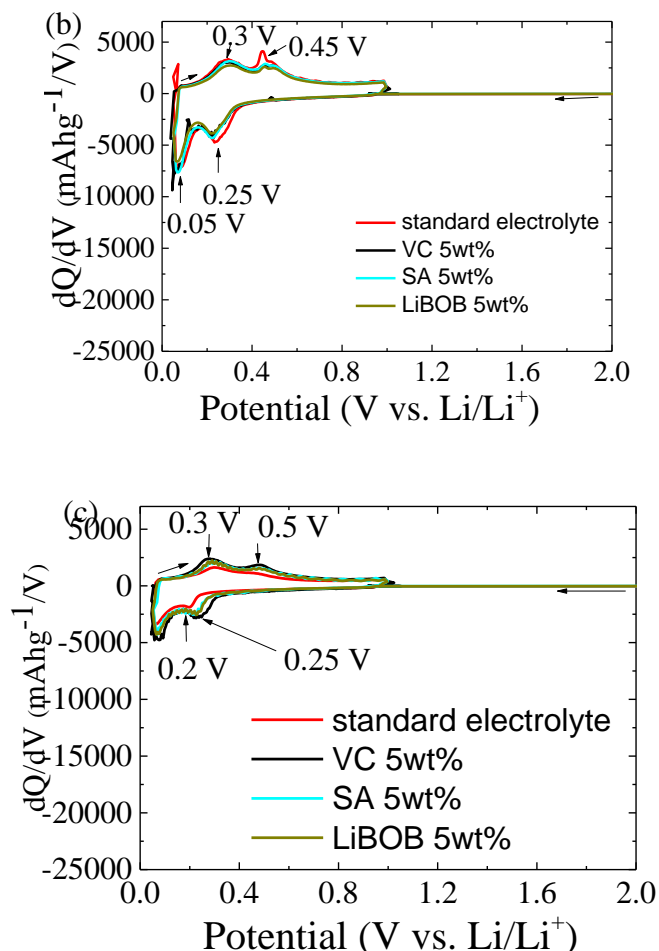
(c)
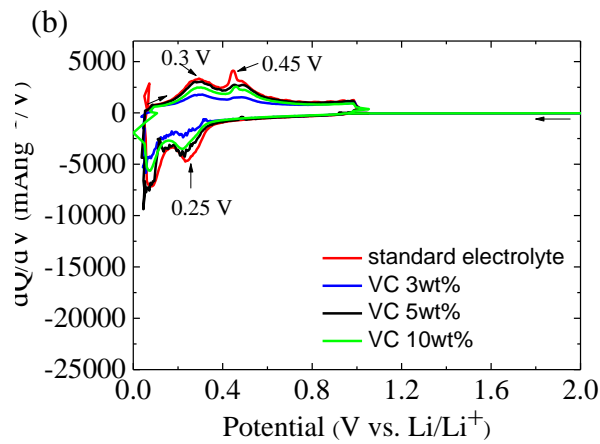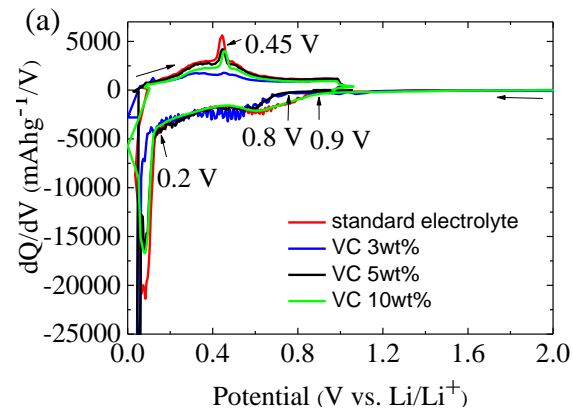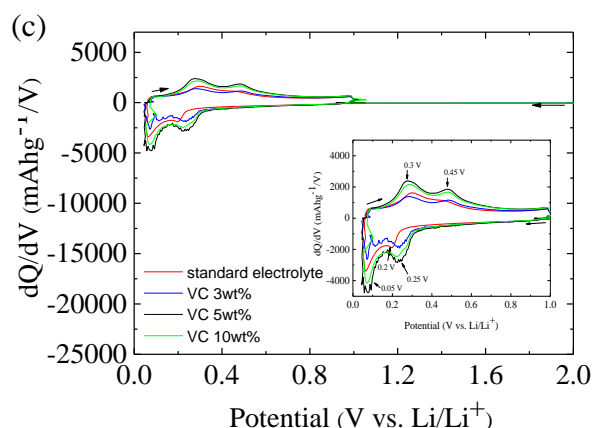
Figure 45. Differential capacity (dQ/dV) vs. potential plots of Si/MC electrodes with different concentrations of VC at (a)1st, (b) 2nd, and (c) 110th cycle.

4.3.3 XPS analysis on SEI modifications

The detailed mechanism of the SEI layer formation is difficult to understand due to complicated nature of SEI layers. However, XPS is conducted as an effort to understand the composition differences between SEI layers on the Si/MC/CB45 electrodes with and without additives.

4.3.3.1 SEI modification on Si/MC electrodes with different electrolyte additives

XPS analysis was conducted in this work as an effort to understand the compositions of SEI layers on the cycled Si/MC electrodes with different electrolytes. Figure 46 shows the XPS spectra with the regions used for quantification for different samples with standard electrolyte (a), 5wt% VC (b), 5wt% LiBOB (c), and 5wt% SA (d). The relative contents (in %) of the samples are depicted in Figure 47. In comparison to the electrode with standard electrolyte, those with electrolyte additives show an increased C and O concentrations. This can be related to the increasing concentration of Li_2CO_3 which is confirmed by the XPS C1s and O1s spectra (discussed below). The electrode with standard electrolyte shows a higher F and Li, which are significantly lower on the samples with LiBOB and SA. The sample with VC shows a higher P content than other additives. The distinct concentrations of Li, F, and P can be related to the decomposition of the $LiPF_6$ electrolyte. No Si content is found on the samples with LiBOB and SA which may due to a thicker layer of SEI.

82
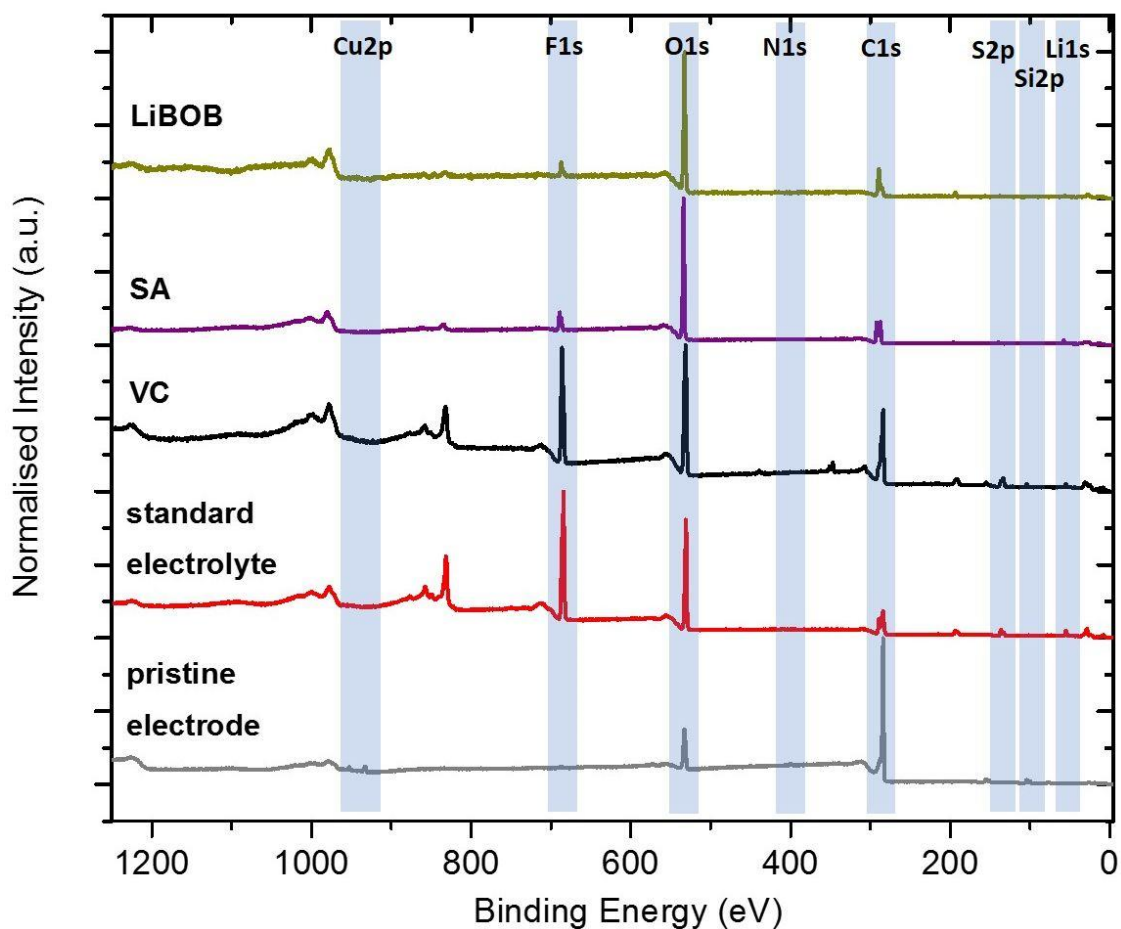
Figure 46. XPS survey spectra of the cycled electrodes with standard electrolyte (a), VC (b), LiBOB (c), SA (d). The light blue areas represent the regions, which have been used for quantification.

.
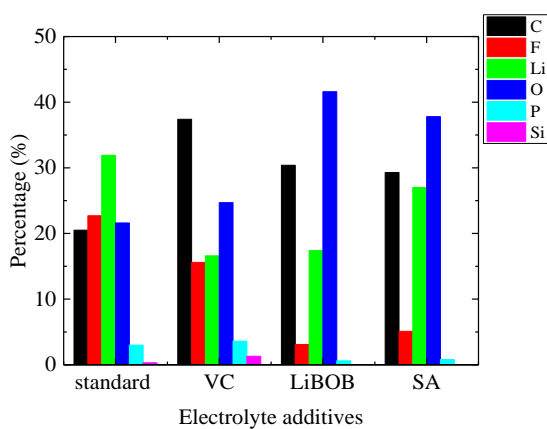
Figure 47. Relative contents of C, F, Li, O, P and Si (in %) for the samples with different electrolyte additives.

Figure 48 shows the XPS C 1s (a), F 1s (b) and P 2p (c) detail spectra of all samples. Several different species can be assigned to the C 1s spectra (dashed lines in Figure 48a).

The C1s spectra (Figure 48a) show 3 to 4 distinct peaks which can be assigned to chemical states as follows. The peak at 284.4 eV can be assigned to C-C and C-H bonds from the carbon substrates. The peak at 286.6 eV is characteristic for CO- and at 285.5 eV is characteristic for CO_2-. The peak at 289.5 eV corresponds to O-C=O/CO_3. The samples with standard electrolyte as well as with VC show a high amount of C-C and C-H bonds. However, the addition of VC increased the amount of CO- and decreased the amount of CO_3. In contrast, the samples with SA and LiBOB show a higher abundance of O-C=O/CO_3 contributions. This can be explained by the presence of SA and LiBOB additives which both contain these bonding environments pointing to deposition of these additives on the SEI during cycling processes. These results confirm the formation of different concentrations of carbonaceous species at the electrode/electrolyte interface. The component of CO_2- at 289.5 eV reveals the decomposition of species like lithium carbonate (Li_2CO_3), and/or lithium alkyl carbonates ($ROCO_2Li$) on the electrode surface [139]. Li_2CO_3 and $ROCO_2Li$ are the result of the degradation of EC following these chemical reactions:

$$EC + 2e^- \rightarrow Li_2CO_3 + CH_2 = CH_2 \qquad\qquad [\,v\,]$$
$$2EC + 2e- + 2Li^+ \rightarrow (CH_2OCO_2Li)_2 + CH_2{=}CH_2 \qquad\qquad [\,vi\,]$$
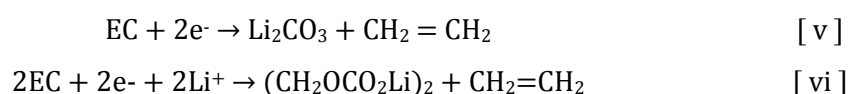
It can be noted that compared to another electrolytes, electrodes with standard electrolyte and VC show less intense of peak at 289.5 eV which means they contain less Li_2CO_3 and $ROCO_2Li$. According to reaction [vi], producing more $ROCO_2Li$ consumes the lithium ion which is supposed to be cycled. This can explain why the electrode with VC 5wt% shows a higher discharge capacity, compared to those with other electrolytes.

The O1s spectra (Figure 48b) show 2 distinct peaks in all samples. The peak at 531.5 eV can be assigned to CO_2 and CO_3- like oxygen environment, while the peak at 533 eV can be assigned to CO-. It can be noted that the sample with VC shows a higher CO/ CO_3 ratio in comparison to the sample with standard electrolyte. The CO-like oxygen environment can correspond to poly(VC). Poly(VC) is formed on the electrode surface when VC is added in the electrolyte [90]. While, the sample with LiBOB shows even much stronger peak intensity of CO-, indicating LiBOB increases the content of semicarbonate ($ROCO_2Li$) in SEI layer. In the case of the sample with SA, the CO-like oxygen environment is significantly low which can be the cause of capacity fading.

The F1s and P2p spectra which allow for the investigation of electrolyte are presented on Figure 48b&c. The F1s spectra (Figure 48c) shows two peaks at 687 eV and 685 eV which can be attributed to $LiPF_6$ and LiF, respectively. Larger amounts of LiF detected in the sample with standard electrolyte suggest significant decomposition of $LiPF_6$ occurring. On the other hand, the samples with VC and LiBOB show a higher amount of $LiPF_6$. The degradation mechanism for $LiPF_6$ is suggested to be [140] :

$$LiPF_6 \leftrightarrow LiF + PF_5 \qquad\qquad [\ vii\ ]$$

$$PF_5 + H_2O \leftrightarrow POF_3 + 2HF \qquad\qquad [\ viii\ ]$$

The P2p spectra (Figure 48b) show two peaks for all cycled electrodes. These two peaks correspond to the $LiPF_6$ at 137.2 eV and phosphate compounds at 133.9 eV. Phosphate compound is the decomposition product which is found on $LiPF_6$-based electrolyte. It can be noted that the sample with SA has a higher content of $LiPF_6$. The relative abundance of the components found in each spectra can be seen in Table 21 - Table 28 (see Appendix).
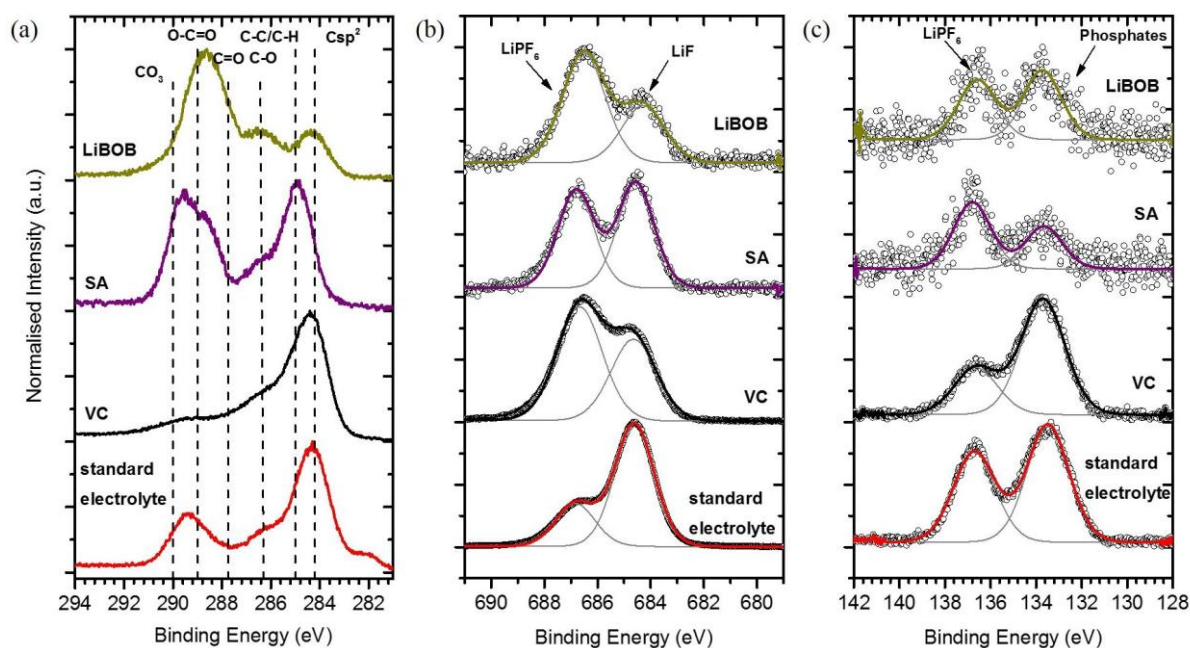
Figure 48. Normalised C1s (a), F1s (b) and P2p (c) XPS detail spectra of cycled Si/MC electrodes with different electrolytes. Dashed lines in (a) show the positions of different C/O components. Gaussian-Lorentzian line fits in (b) and (c) represent the F and P components as noted on top.

XPS analysis for the Si/MC with and without 5wt% VC additive for 20 and 50 cycles were also performed to see the generation of the compounds in SEI layer over the cycles.

Figure 49 shows the XPS spectra of the samples. The relative contents (at %) of samples with and without 5wt% VC additive can be seen in Figure 50 a&b. During XPS measurements, the pristine sample has been found to be conducting, while the cycled samples showed an insulating behaviour due to organic material found on the surface. A non-conducting sample was detected when all peaks are broadened and shifted to higher binding energies from their expected positions.

Figure 50 shows the pristine sample shows C, O, Si contents. Compared to the pristine sample, the cycled samples show a higher content of Li, F, O, and P which were generated from the electrolyte decomposition. The F and P contents increase with the number of cycles in the samples with VC, while they have behaved opposite in the samples without VC. Ca has been found in both samples where VC has been used in the electrolyte (0.8 – 0.9%). This impurity may come from the VC because it is not found in the samples with LiBOB and SA.
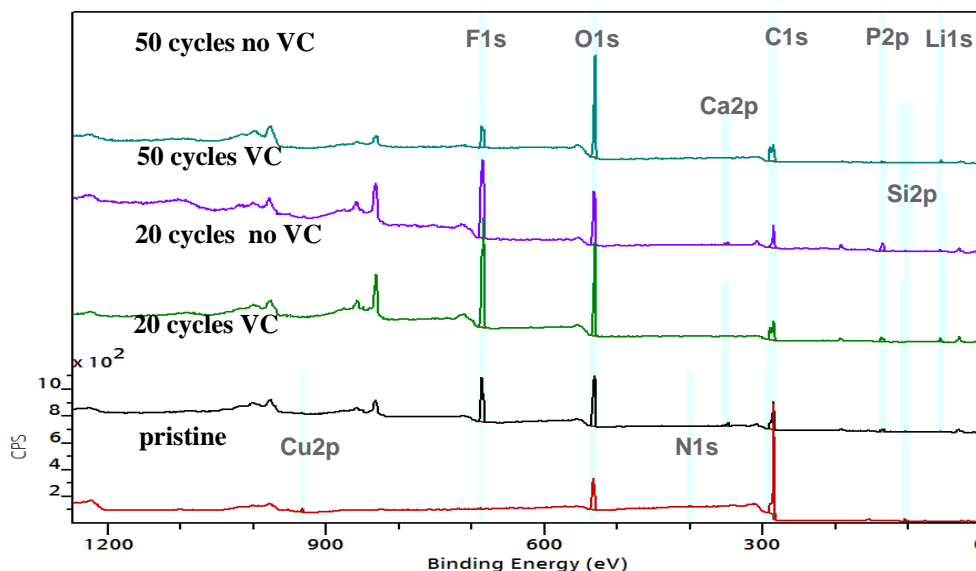
Figure 49. XPS survey spectra of samples ; pristine (red), 20 cycles VC (black), 20 cycles NO VC (green), 50 cycles VC (purple) and 50 cycles NO VC (turquoise). The blue areas represent the regions, which have been used for quantification.
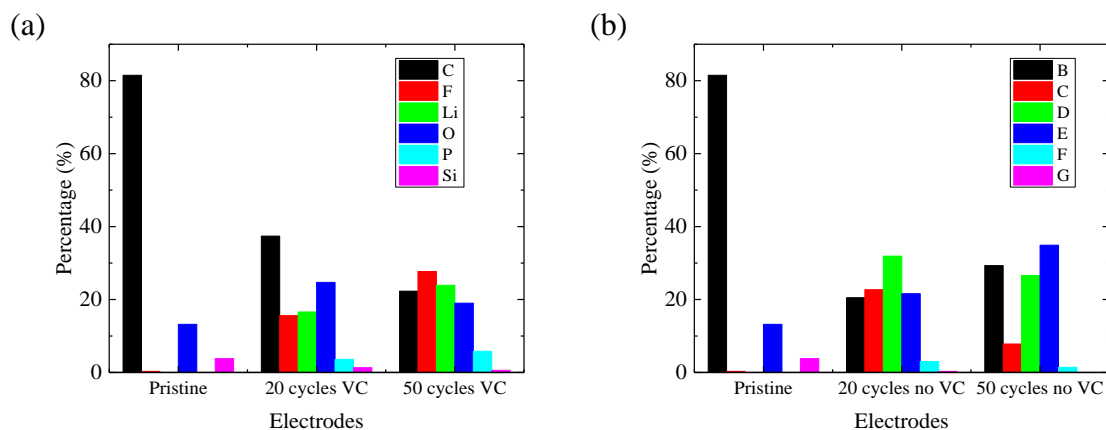
Figure 50. Relative C, F, Li, O, P and Si contents (in %) on the pristine electrode, the cycled electrodes (a) with VC and (b) without VC.

All spectra have been corrected in binding energy according to the oxygen and carbon signals. Table 25-27 summarize the results of this analysis showing the relative abundance (in %) of the components found in C, O, F, and P spectra.

The C1s spectra (Figure 51a) show 3 distinct peaks. As discussed before, the large peak at 284.4 eV can be assigned to C-C and C-H bonds from the carbon substrate. The peak at 286.6 eV can be assigned to CO-, while the peak at 290.0 eV is characteristic of CO_2. The component at 290.0 eV reveals the decomposition of species like lithium carbonate Li_2CO_3, and/or lithium alkyl carbonates $ROCO_2Li$ on the electrode surface [50]. To explain the stronger peak detection of C-C/C-H at the electrode with VC, it is assumed that the SEI layer remains stable without any thickening.

The O1s spectra (Figure 51b) show 2 distinct peaks in all samples. A peak is observed at 531.7 eV and corresponds to CO_2 and CO_3-like oxygen environment. A peak at 534 eV can be assigned to CO- which corresponds to poly(VC). The instability of sp[2] orbital on VC triggers the ring-opening reactions. The presence of vinyl group allows polymerization and produces a stable protective layer [141]. It can be seen that the samples without VC show a CO_3/CO ratio higher than in the one with VC.

87
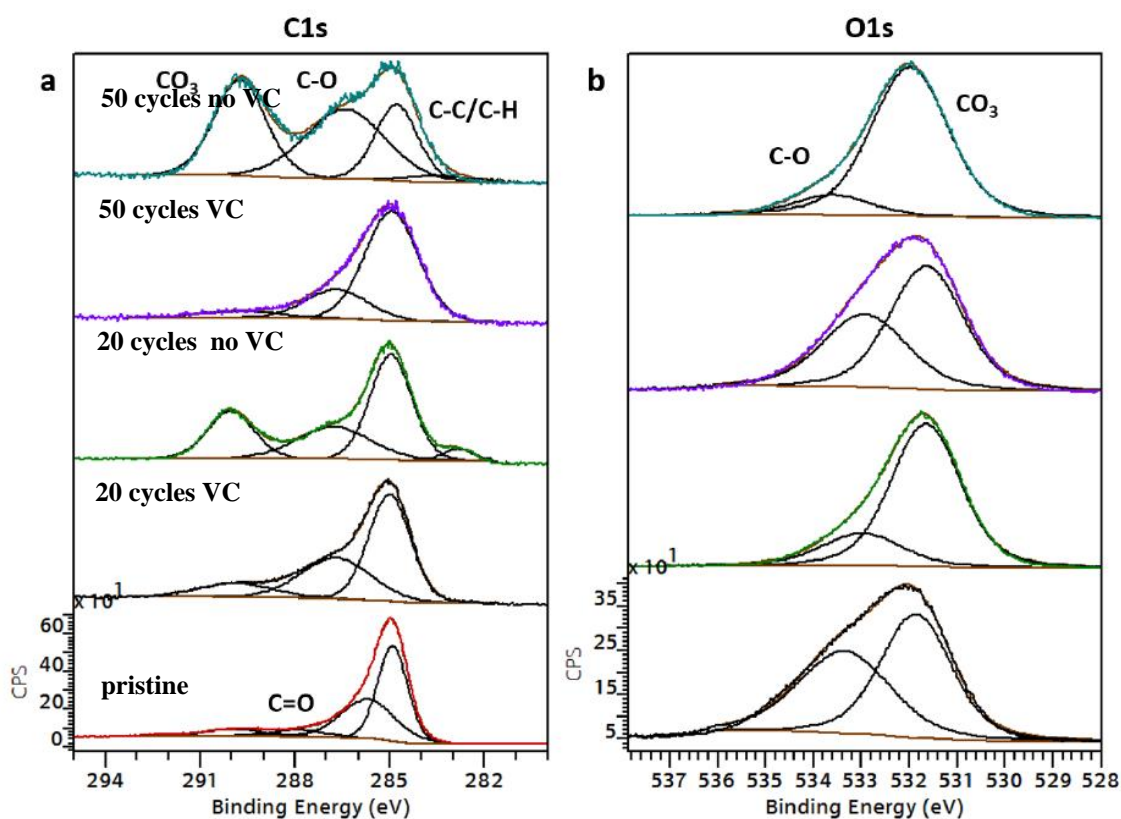
Figure 51. XPS C1s (a) and O1s (b) detail spectra of samples pristine (red), 20 cycles VC (black), 20 cycles NO VC (green), 50 cycles VC (purple) and 50 cycles NO VC (turquoise).

The F spectra (Figure 52a) show two peaks at 687 eV and 685 eV which are attributed to $LiPF_6$ and LiF, respectively, as seen also before on Figure 48. The sample with VC shows a lower ratio of $LiPF_6$/LiF. It means less significant decomposition of $LiPF_6$ is occurring on the samples with VC. On the other hand, the samples with VC show a larger amount of $LiPF_6$.

The P_2p spectra (Figure 52b) also show two peaks for all cycled electrodes. These two peaks correspond to the $LiPF_6$ at 137.2 eV and phosphate compounds at 133.9 eV. Phosphates which are the decomposition products of $LiPF_6$ are found higher on the samples with VC. This result is contrary to the previous one that presumed less decomposition on the samples with VC. Thus, it is assumed that the decomposition product of $LiPF_6$ with VC additive is in the LiF form instead of phosphates.
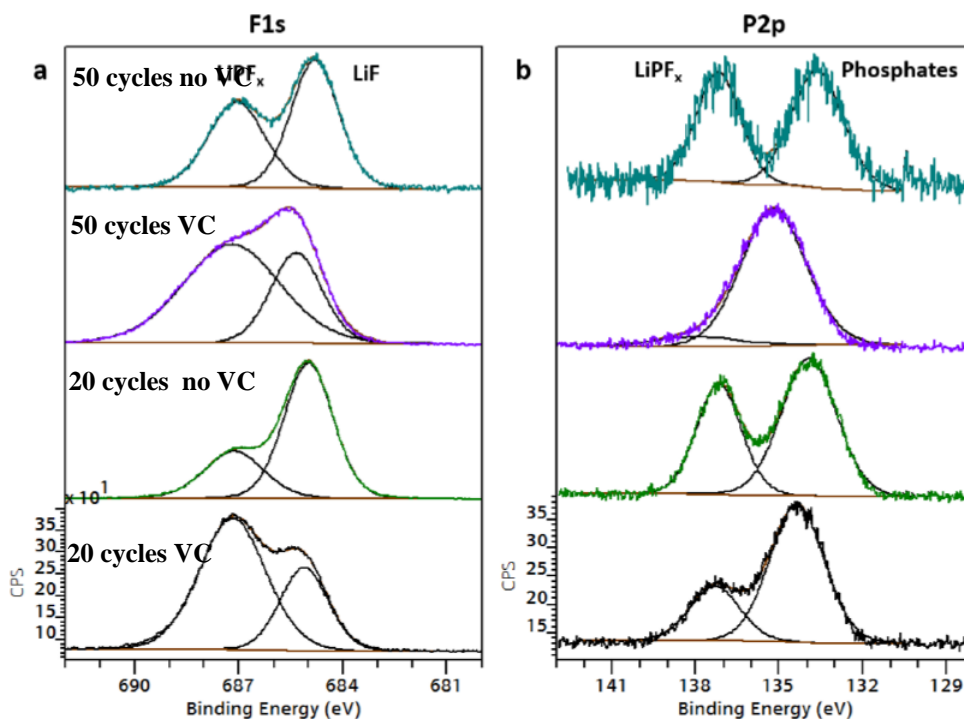
Figure 52. XPS F1s (a) and P2p (b) detail spectra of samples 20 cycles VC (black), 20 cycles NO VC (green), 50 cycles VC (purple) and 50 cycles NO VC (turquoise).

4.3.4 SEM analysis

The SEM images of Si/MC with different electrolytes after 20 cycles are depicted in Figure 53. The electrode with standard electrolyte shows agglomerate particles. A similar morphology can be seen for the electrodes with different electrolytes. Meanwhile, the electrodes with electrolyte additives show white colors which can be assigned to deposited Li-salts. This white color is more pronounced on the electrode with LiBOB which also explain the more decomposition of electrolytes.
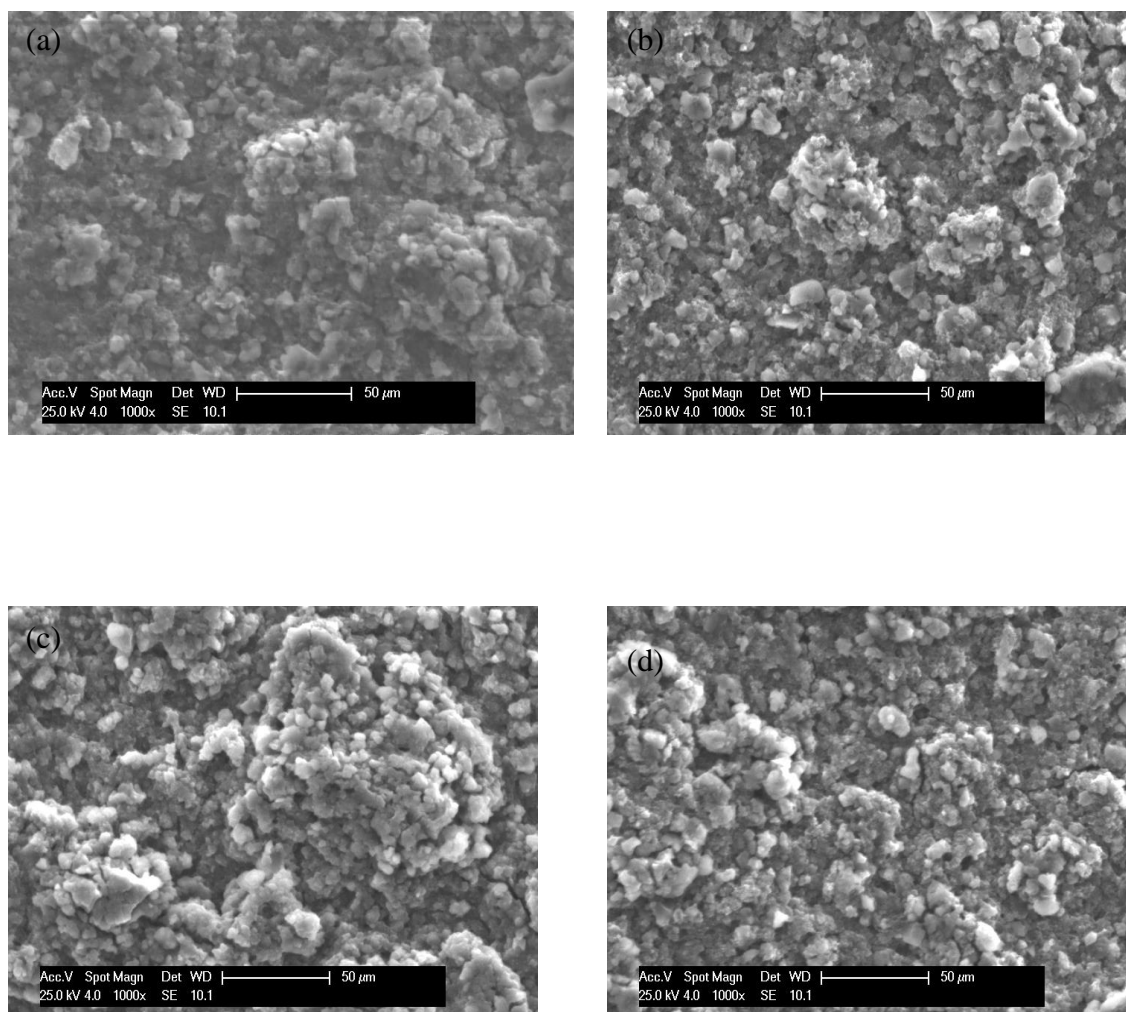
Figure 53. SEM images of Si/MC electrodes after cycling with standard electrolyte (a), VC 5wt% (b), SA 5wt%, (c), LiBOB 5wt% (d)

The SEM images of the Si/MC with VC additive with concentration after 20 cycles are depicted in Figure 54.
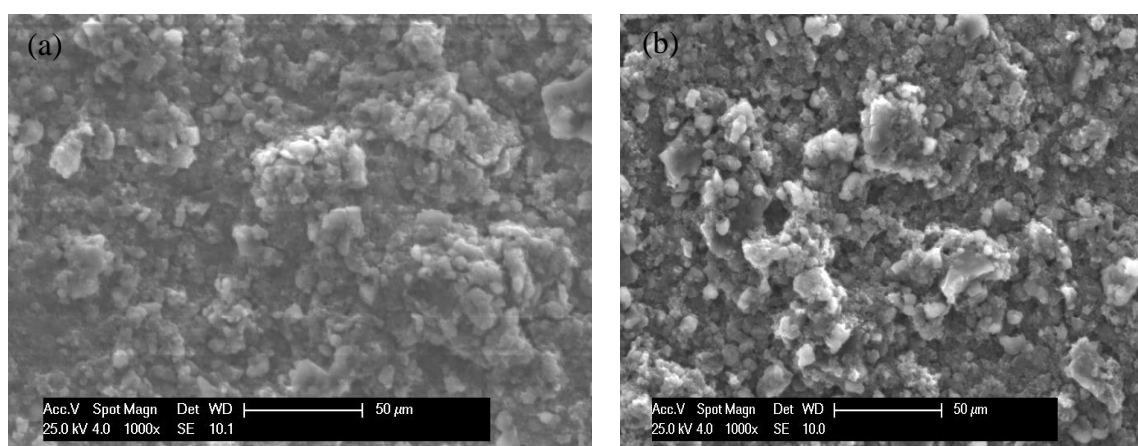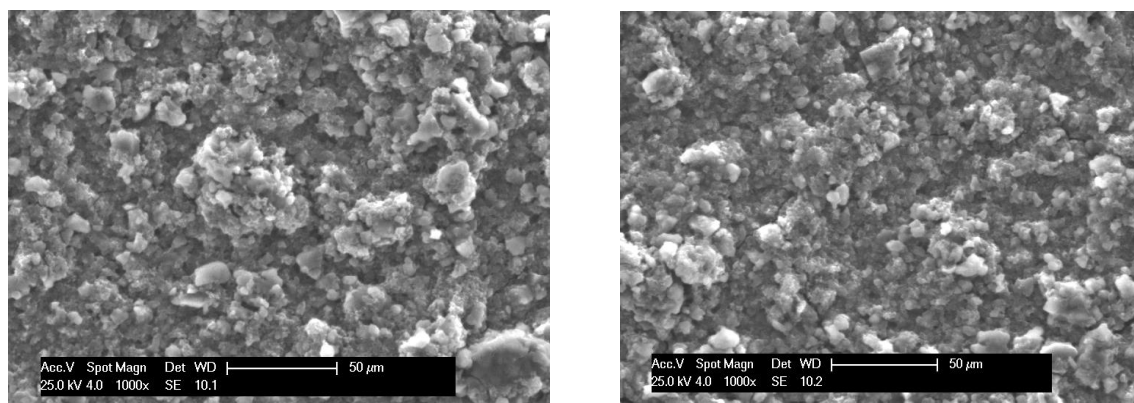
Figure 54. SEM images of Si/MC : standard electrolyte (a), cycled with VC 3wt% (b), VC 5wt% (c), VC 10wt% (d)

4.3.5   Conclusions

A comparative study has been conducted for the Si/MC electrodes with different electrolyte additives: VC, SA, and LiBOB with the same concentration (5wt%). The electrochemical test showed that the electrode with VC showed the best reversible capacity and rate capability, compared to that with SA and LiBOB and standard electrolyte. The electrode with 5wt% VC delivered a stable capacitiy of 1100 mAhg^{-1} up to 100 cycles. At 1C and 2C, the electrode exhibited a high discharge capacity of 903 mAhg^{-1} and 683 mAhg^{-1}. Ex-situ XPS analysis showed distinct differences of SEI chemical composition on Si/MC electrode with different electrolyte additives. With standard electrolyte, the SEI contains more LiF and less amount of Li_2CO_3 and lithium alkyl carbonate. With VC additive, the generation of poly(VC), Li_2CO_3 and $ROCO_2Li$ on the surface and the reduced LiF content improved the cycling performance of Si/MC electrode. The addition of LiBOB increased the content of semi-carbonate in SEI layer. With SA, the sample showed less $LiPF_6$ which means less decomposition of the electrolyte.

4.4   Towards realistic design of Si/MC-based anodes

As discussed above, the Si/MC electrode with the addition of Super C45 in the electrode and 5wt% VC in the electrolyte exhibits a relatively stable electrochemical performance. As shown in Figure 55, the Si/MC/CB45 electrode exhibited ~800 mAh g^{-1} for 400 cycles. Rate capability tests on Figure 44a showed that the electrode retained a discharge capacity of 877 mAg h^{-1} at 2C. This electrode performs better than the reported mesoporous C/Si with 1 M $LiPF_6$ in a mixture of FEC–DMC (1 : 1 by volume) which exhibited 1018 mAh g^{-1} after 100 cycles [56].

91
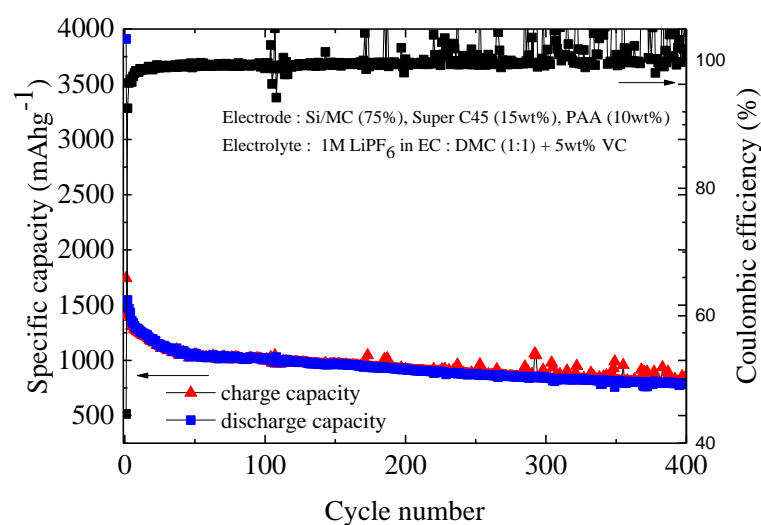
Figure 55. Electrochemical performance of the as-synthesized Si/MC with super C45 additive with 1M in a mixture of EC–DMC (1 : 1 by volume) with 5wt% VC.

From the synthesis point of view, the precursors used (Si nanoparticles, resorcinol, formaldehyde, ammonia, and HF) are produced industrially at relatively low costs. Second, the conversion of mesoporous carbon was done by a single heating step at 650°C to save the energy. Third, HF etching was used to create the voids without using additional template. Thus, this synthesis route has a good potential for mass production. The next question is, does this meet the realistic design for commercial Li-ion batteries?

4.4.1 Reliability of the as-prepared Si-based anode realistic for commercial Li-ion battery anode

The ratio of silicon nanoparticles in the prepared Si/MC/CB45 electrode is ~12.98 wt%. This value is close to the theoretical threshold values of Si in silicon carbon composite based anode, calculated by Dash et al. [100]. The reported threshold value of Si amount to maximize the volumetric energy density was determined to be 11.68 wt%. The maximum capacity of the silicon carbon composite anode with no volume expansion constraint was determined to be ~712 mAh g^{-1}. In comparison to the aforementioned study, the prepared Si/MC/CB45 electrode has a potential to be applied in the Li-ion batteries systems.

In addition, according to a review reported by Lee et al. [99], a specific capacity of the anode up to about 800-1000 mAhg^{-1} could increase total specific capacity up to 21–25% higher

than graphite-based Li-ion batteries, when coupled with cathodes with specific capacity of 140–170 mAh g^{-1}.

4.4.2   Study of the diffusion coefficient of lithium ions in Si/MC electrode

The diffusion coefficient of lithium ions is a common physical quantity to characterize mobility of Li-ion batteries. Of course, lithium ion's mobility changes depending on many parameters, such as the electrode's geometry and the cycling rate. However, assessing the diffusion coefficient of lithium ions on the prepared Si/MC/CB45 can be useful to see the perfomance. In this work, EIS and CV techniques have been used to estimate macroscopic chemical Li-ion diffusion. The results from both techniques are compared. Figure 56a shows Nyquist plot of Si/MC/CB45 with 5wt% VC additive at 1.0 V vs Li/Li$^+$. With the assistance of the relationship Zim and square root of angular frequency (Figure 56b), the diffusion coefficient was calculated by following equation (19), giving 5.68 x 10^{-14} cm^{2}s^{-1}. This value is still considered high in the range of the reported diffusion coefficient of Li$^+$ in Si (10^{-14} – 10^{-17} cm^{2}s^{-1}) [131]. The difference comes from the area of electrode used in the calculation. In this electrode, the real contact area should be higher than the one used in the calculation. Thus, this calculated diffusion coefficient is considered as "apparent diffusion coefficient".
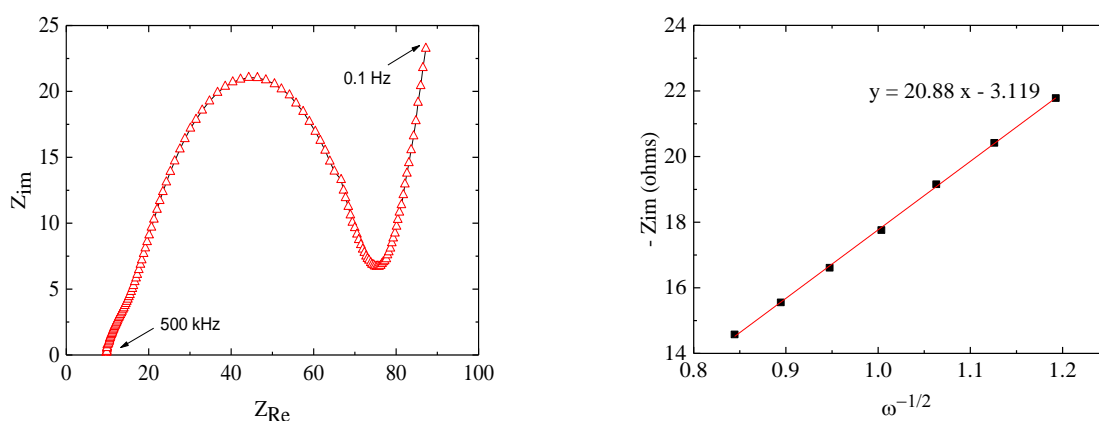
Figure 56. Nyquist plot of Si/MC/CB45 with 5wt% VC additive after 20 cycles (a) and the relationship of Zim vs $\omega^{-1/2}$ (b)

CV measurements with varying scan rates of 0.02 mVs^{-1}, 0.05 mVs^{-1}, 0.2 mVs^{-1}, and 0.5 mVs^{-1} were performed on the Si/MC/CB45 electrode with 5wt% VC. The CV curves are shown in Figure 57. As already discussed, the reduction peak at 0.2 V vs. Li/Li$^+$ corresponds to lithium

93

insertion into amorphous silicon. The peak current increases with the increasing scan rates which can be a sign for fast electron transfer process with diffusion limitation.
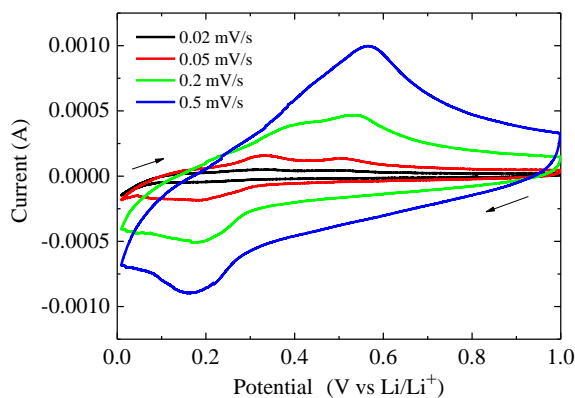
Figure 57. Cyclic voltammetry curves of Si/MC/CB45 with 5wt% VC in LiPF$_6$ in EC:DMC 1:1 with different scan rates: 0.02, 0.05, 0.2 and 0.5 mVs^{-1}.

Figure 58 shows that the peak current increases linearly with the square root of scan rates which confirms it is a reversible system.
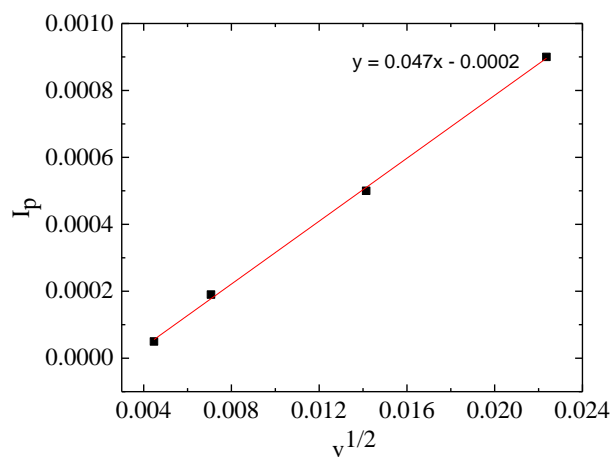
Figure 58. The relationship of the peak current and square root of scan rate from cyclic voltammetry curves of Si/MC/CB45 with 5wt% VC in LiPF$_6$ in EC:DMC 1:1 with different scan rates: 0.02, 0.05, 0.2 and 0.5 mVs^{-1}.

Afterwards, the diffusion coefficient was calculated by using linear regression from the peak current and the square root of scan rates and following Randles-Sevcik equation [142]:

$$i_p = (2.69 \ x \ 10^5)n^{3/2}AD_{Li^+}^{1/2}C_{Li}v^{1/2} \hspace{3cm} (\ 19\ )$$

Where i_p is the peak current (A), n is the charge concentration in Li_xSi (n = 2.2), A is the contact area between Si and electrolyte (calculated from the geometric area of the electrode, 1.766 cm², C_{Li} is the bulk concentration of lithium in electrode (0.0753 mol.cm⁻³, calculated from Li_7Si_3), and v is the scan rate. The diffusion coefficient was calculated and giving 1.62 x 10⁻¹³ cm²s⁻¹. This value is higher than the one calculated with EIS.

4.4.3   Conclusion

Looking at the composition of the Si nanoparticles in the Si/MC/CB45 electrode (~12.98 wt%), the cycling stability of the electrode (~800 mAh g⁻¹ for 400 cycles), and the diffusion coefficient of lithium ions in silicon (5.68 x 10⁻¹⁴ cm²s⁻¹ based on EIS and 1.62 x 10⁻¹³ cm²s⁻¹ based on CV), this electrode configuration meet the rational design for anodes for Li-ion batteries application.

4.5   Full cells containing Si/MC/CB45 anode and commercial NMC cathode

To assess the electrochemical performance of Si/MC/CB45 in a full cell, the Si/MC/CB45 anode was coupled with a commercial NMC cathode in a pouch cell configuration. The cell chemistry used in this study can be seen in

Table 8. The discharge capacity is given in electrode areal capacity (mAh.cm⁻²) to easily balance both electrodes.

4.5.1   Electrochemical performance of commercial NMC cathode

$LiNi_{1/3}Co_{1/3}Mn_{1/3}O_2$ (NMC) is common and widely used as a cathode material in the Li-ion battery market. Besides, it is a strong alternative of cathode materials for electrical vehicle application. Figure 59a&b show the discharge profile and dV/dQ curve for a NMC electrode half cell during the first cycle at C/10. The NMC electrode delivers an initial discharge capacity of 0.8 mAh.cm⁻². Essentially, any slopes in the voltage profile during charge or discharge will yield a peak in the dV/dQ curve. Figure 59b shows a broad hump for a capacity of 0.1 mAh.cm⁻² which is the representative of the initial slope in the potential vs. capacity curve.

(a)

(b)
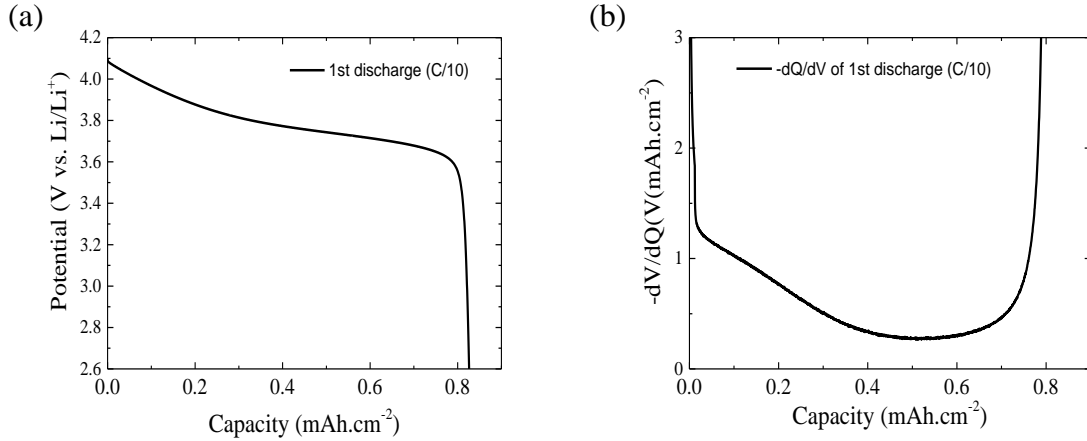
Figure 59. Discharge profile (a) and dV/dQ (b) vs. capacity curves of first discharge from NMC half cell with a voltage range 2.6 - 4.1 V vs Li/Li+.

To monitor at which voltage the lithiation and delithiation takes place, the dQ/dV curve is also plotted. Figure 60 shows the potential profile and dQ/dV from the first lithiation and delithiation of the NMC half cell. In this case, the plateus in the potential profile will be presented as peaks in the dQ/dV curve. The peak at ~ 3.8 V is due to the oxidation of Ni^{2+} to Ni^{4+} [143].

(a)

(b)
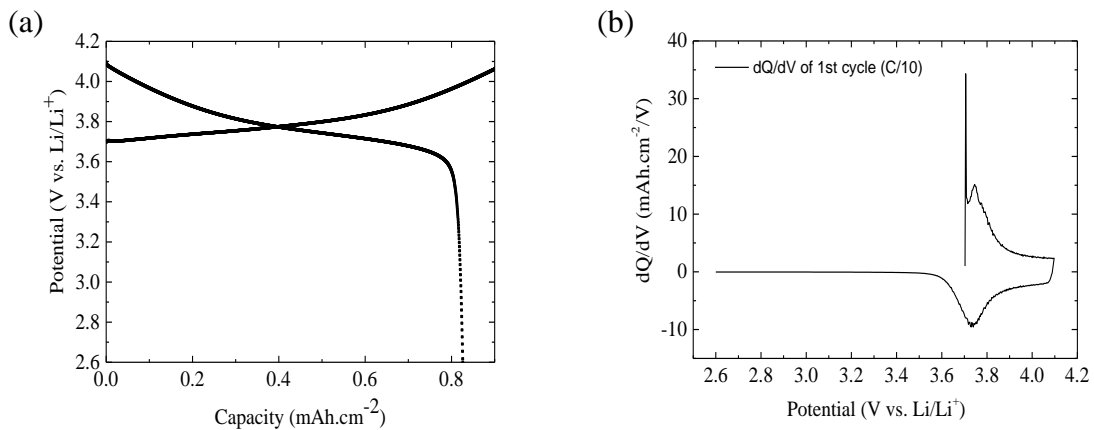
Figure 60. Cell potential (a) and dQ/dV vs. cell potential (b) curves of first charge-discharge from NMC half cell with a voltage range 2.6 - 4.1 V vs Li/Li+.

4.5.2 Electrochemical performance of a full cell containing a Si/MC anode and a NMC cathode

The Si/MC/CB45 half cell was built using the pouch configuration and 1 M LiPF$_6$ in EC:DEC in a 1:1 weight ratio (LP40) electrolyte to easily compare with the results from the full cell. The charge-discharge profiles for C/10 for the first four cycles and 1C for subsequent cycles (1st and 20th after resting) are presented in Figure 61a&b, respectively. During the first cycle, an amount of 0.8 mAh.cm^{-2} was consumed for SEI formation. At C/10, the Si/MC/CB45 electrode exhibits a reversible discharge capacity of 0.6 mAh.cm^{-2}. At 1C, the discharge capacity decreases up to 0.2 mAh.cm^{-2}.

(a)   (b)
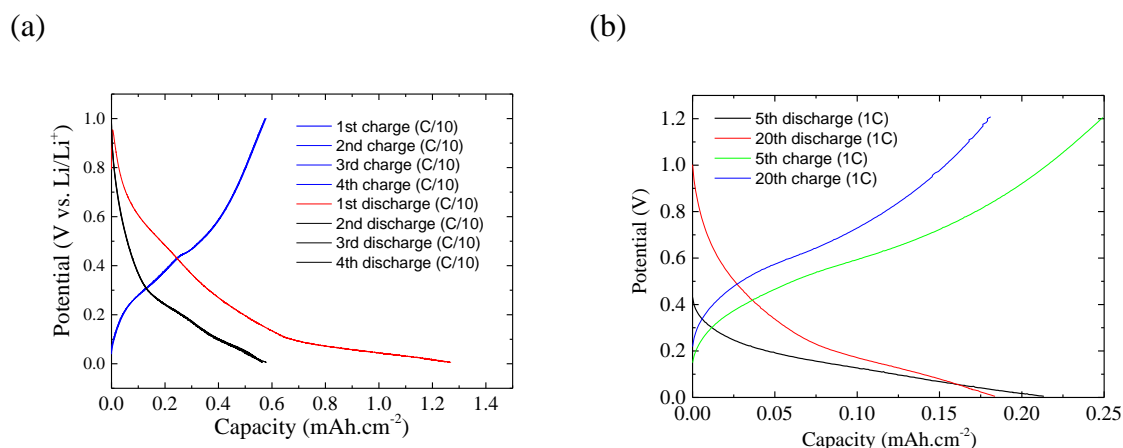
Figure 61. Charge-discharge profile of Si/MC half cell with a voltage range 0.005 - 1 V vs Li/Li+ at C/10 (a) and 1C (b).

Figure 62 shows the dV/dQ curve of the first delithiation from full cell which is plotted against the first delithiation of the NMC half cell and the first lithiation of the Si/MC/CB45 half cell at C/10. These curves can be used to determine the operating potential range for the cell. The peaks of the full cell are assumed to be the sum of both half cells. Since the NMC half cell shows no significant peak, the contributions of the peaks can be assigned mostly from the Si/MC/CB45 half cell. However, there is an additional peak at the capacity of 0.15 mAh.cm^{-2} which may correspond to the hump of NMC half cell at 0.1 mAh.cm^{-2} (Figure 59b).
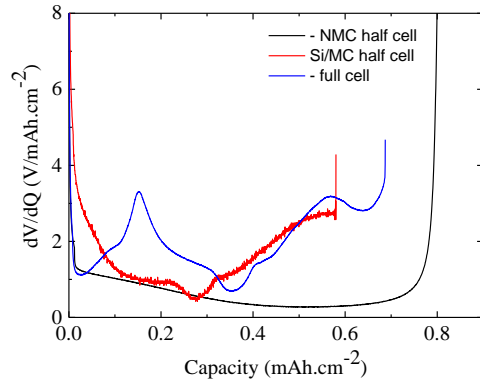
Figure 62. dV/dQ vs. capacity density curves of first delithiation of half cells and full cell with C/10.

Figure 63a shows the initial charge-discharge profiles of the full cell at C/10. The cell exhibited a charge capacity of 1.4 mAh.cm^{-2} and discharge capacity of 0.7 mAh.cm^{-2} during the first cycle. Discharge capacity and columbic efficiency (CE) for different cycles can be seen in Figure 63b. The cell showed a decreasing discharge capacity to ~0.2 mAh.cm^{-2} up to 80 cycles. To be noted that the cell was cycled at high rate (1C) and no electrolyte additive was used for this measurement. The electrochemical performance may be improved by using vinyl carbonate additive. Figure 63b shows that the discharge capacity decreases, however, CE increases over the cycles. The reason can be that the SEI layer thicken and parasitic reactions between the electrode and the electrolyte slow down, as investigated by Fathi et al [144].
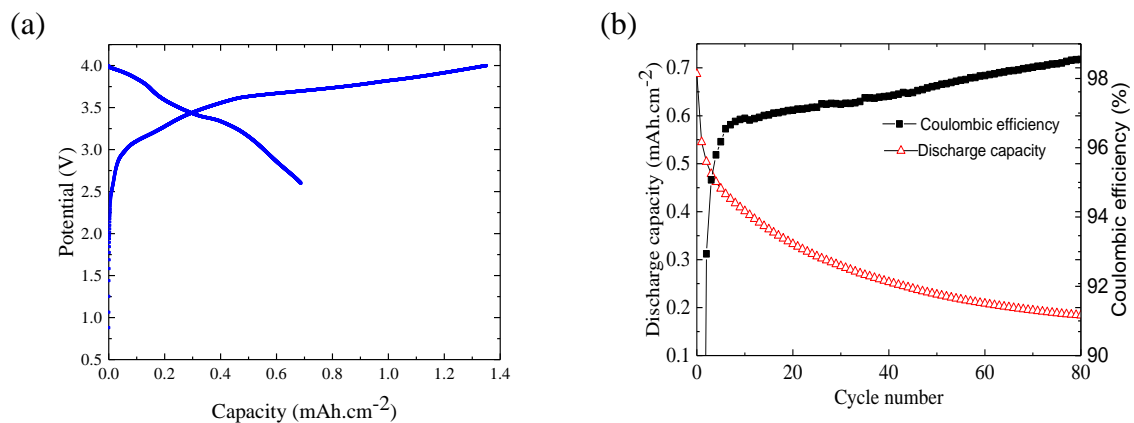
Figure 63. Charge-discharge profile of the first cycle at a rate of C/10 (a) and discharge capacity vs. cycle number profile at a rate of 1C (b) from a full cell containing Si/MC anode and NMC cathode with a voltage range 2.6 – 4.0 V.

To get some information about the capacity fading, the capacity variation can be monitored by visualizing the dQ/dV curves. Figure 64 shows the differential capacity curves of the full cell for 1st, 2nd, and 80th cycles. First cycle shows three distinct peaks around 2.75 V, 3.4 V, and 4.0 V during delithiation. The intensity of the peaks weaken over the cycles. This indicates that the active materials are less active because of the thickening of SEI formation. The peaks shift to the higher voltage in the lithiation and the lower voltage in the delithiation can be assigned to increasing cell impedance upon cycling. This phenomena can be explained by the contact loss of active materials due to the electrode material degradation since a relatively high C-rate was applied. However, it is difficult to distinguish the contributions from which electrode with the two-electrode set-up.
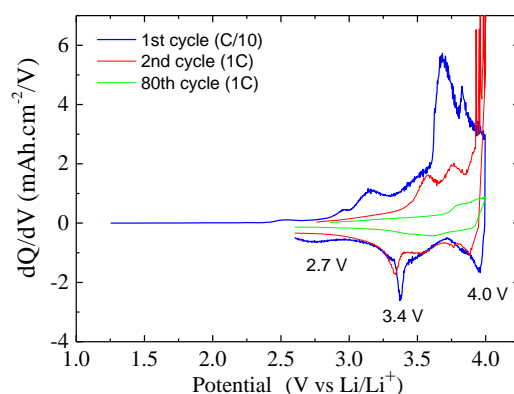
Figure 64. dQ/dV vs. potential for the 1st, 2nd and the 80th cycles for the NMC/Si-MC full cell with C/10 (first cycle) and 1C (subsequent cycles).

4.5.3   Conclusions

A full cell containing a Si/MC/CB45 anode and a commercial NMC cathode was assembled in a pouch cell configuration. The full cell exhibited a discharge capacity of 0.7 mAh.cm^{-2} in the first cycle at a rate of C/10 and 0.5 mAh.cm^{-2} at a rate of 1C between 2.6 – 4.0 V. To investigate the reason of capacity fading of the full cell, the electrochemical performance of each half cell should be looked and analyzed more. In addition, further investigations on different cut-off voltage and mass balance of the electrodes could improve the electrochemical performance of a NMC and Si/MC full cell.

Chapter V

Summary

Si/MC composites were successfully synthesized by dispersing silicon nanoparticles into a Resorcinol-Formaldehyde (RF) gel and by subsequent carbonization. HF etching of the composites was conducted to remove passive oxide layers from commercial Si nanoparticles and produce a porous matrix between the Si and the carbon layer. This synthesis route has been chosen due to three advantages. First, the precursors (Si nanoparticles, resorcinol, formaldehyde, ammonia, and HF) are produced industrially at relatively low costs which has a good potential for mass production. Second, the conversion of mesoporous carbon was done by one single heating step at 650°C to save the energy. Third, HF etching was used to create the voids without using additional template.

The etched Si/MC electrode exhibits a reversible capacity of 585 mAhg^{-1} with a Coulombic efficiency of 99.57% after 135 cycles, which is better compared to the non-etched Si/MC electrode (237 mAhg^{-1} after 135 cycles). The improved cycling performance of the etched Si/MC composite can be attributed to its enhanced structural stability. The additional pores which were proven by BET and TEM analysis could buffer the mechanical stress that arises from the volume change of Si.

The effect of the conductive additives on the electrochemical performance of Si/MC anodes was also investigated. Electrochemical tests showed that the highly structured conductive graphite had a double function: as conductivity enhancer and as an active material for electrode component. In spite of its higher specific area, Super C65 improved Si/MC electrodes better than conductive graphite. Meanwhile, Super C45 can minimize the initial charge loss of Si/MC electrode better than Super C65.

As further step to decrease the initial charge loss of the Si/MC/CB45 electrode, electrolyte additives have been used: VC, SA, LiBOB. The electrochemical tests showed that the electrode working with the electrolyte with VC showed the best reversible capacity and rate capability, compared to that with SA and LiBOB and standard electrolyte. The electrode with 5wt% VC delivered a relatively stable electrochemical performance, better than those with 3wt% VC and 10wt% VC. The XPS investigations exhibit distinct differences of SEI chemical composition between Si/MC electrodes with and without VC. Without additives, the SEI

contains more LiF and less Li_2CO_3 and lithium alkyl carbonate. When VC is added, the generation of poly(VC), Li_2CO_3 and $ROCO_2Li$ on the surface and a reduced LiF content cause an improvement in cycling performance. The addition of VC in 1M $LiPF_6$ in EC:DMC (1:1) electrolyte can improve the performance of Si/MC-based electrodes.

The Si/MC/CB45 electrode which contains ~12.98 wt% Si from the total electrode working with 5wt% VC showed an excellent performance. The electrode exhibited a discharge capacity of 1100 $mAhg^{-1}$ up to 100 cycles. At 1C and 2C, the electrode exhibited a high discharge capacity of 903 $mAhg^{-1}$ and 683 $mAhg^{-1}$, respectively.

A full cell containing Si/MC/CB45 combined with a commercial NMC cathode was also assembled. The full cell exhibited a discharge capacity of 0.7 $mAh.cm^{-2}$ (736 $mAhg^{-1}$) in the first cycle at a rate of C/10 and ~0.5 $mAh.cm^{-2}$ (526 $mAhg^{-1}$) at a rate of 1C between 2.6 – 4.0 V.

In summary, these findings hopefully bring a significant improvement in selecting appropriate synthesis methods, conductive binders, and electrolyte additives for fabricating Si-based anodes with a rational design to be used in commercial Li-ion batteries for electrical vehicle application.

Appendix

Table 21. Relative abundance (at %) of the components found in C spectra

Sample	Component (%)			
	C-C/C-H (at 284.8 eV)	C-O (at 286.3 eV)	C=O (at 288.5 eV)	O-C=O/CO_3 (at 289.5 eV)
Standard electrolyte	45.3	26.6	-	22.6
VC 5wt%	51.0	39.6	-	9.4
LiBOB 5wt%	18.3	17.9	37.4	26.4
SA 5wt%	37.9	12.9	19.5	29.7

Table 22. Relative abundance (at %) of the components found in O spectra

Sample	Component (%)	
	CO_3 (at 531.5 eV)	CO (at 533 eV)
Standard electrolyte	80.1	19.9
VC 5wt%	51.5	48.6
LiBOB 5wt%	16.9	83.1
SA 5wt%	90.5	9.5

Table 23. Relative abundance (at %) of the components found in F spectra

Sample	Component (%)	
	$LiPF_6$ (at 686.6 eV)	LiF (at 684.4 eV)
Standard electrolyte	29.3	70.7
VC 5wt%	68.5	31.3
LiBOB 5wt%	75.2	24.8
SA 5wt%	54.9	45.1

Table 24. Relative abundance (at %) of the components found in P spectra

Sample	Component (%)	
	Phosphates (at 133.5 eV)	$LiPF_6$ (at 136.7 eV)
Standard electrolyte	59.4	40.6
VC 5wt%	74.2	25.8
LiBOB 5wt%	60.1	39.9
SA 5wt%	53.2	46.8

Table 25. Relative abundance (at %) of the components found in C spectra

Sample	Component (at %)			
	C-C	C-O	CO_3	C=O
pristine	68.0	18.6	2.3	11.1
20 cycles with VC	51.0	39.6	9.4	
20 cycles without VC	45.3	26.6	22.6	
50 cycles with VC	74.0	21.3	4.7	
50 cycles without VC	21.1	42.8	36.1	

Table 26. Relative abundance (at %) of the components found in O spectra

Sample	Component (at %)	
	CO_3	CO
20 cycles with VC	51.5	48.6
20 cycles without VC	80.1	19.9
50 cycles with VC	56.1	43.9
50 cycles without VC	89.0	11.0

Table 27. Relative abundance (at %) of the components found in F spectra

Sample	Component (at %)	
	$LiPF_6$	LiF
20 cycles with VC	68.5	31.3
20 cycles without VC	29.3	70.7
50 cycles with VC	66.6	33.4
50 cycles without VC	44.7	55.3

Table 28. Relative abundance (at %) of the components found in P spectra

Sample	Component (at %)	
	Phosphates	LiPF$_6$
20 cycles with VC	74.2	25.8
20 cycles without VC	59.4	40.6
50 cycles with VC	(92.9)	(7.6)
50 cycles without VC	52.0	48.0

References

[1]   X.-P. Gao and H.-X. Yang, "Multi-electron reaction materials for high energy density batteries," *Energy Environ. Sci.*, vol. 3, no. 2, p. 174, 2010.

[2]   B. Philippe, *Insights in Li-ion Battery Interfaces through Photoelectron Spectroscopy Depth Profiling*. 2013.

[3]   J. Xu, S. Dou, H. Liu, and L. Dai, "Cathode materials for next generation lithium ion batteries," *Nano Energy*, vol. 2, no. 4, pp. 439–442, 2013.

[4]   M. S. Whittingham, "Lithium batteries and cathode materials," *Chem. Rev.*, vol. 104, no. 10, pp. 4271–4301, 2004.

[5]   M. Lazzari and B. Scrosati, "A cyclable lithium organic electrolyte cell based on two intercalation electrodes," *J. Electrochem. Soc.*, vol. 127, no. 3, pp. 773–774, 1980.

[6]   R. Yazami and P. Touzain, "A reversible graphite-lithium negative electrode for electrochemical generators," *J. Power Sources*, vol. 9, no. 3, pp. 365–371, 1983.

[7]   Z. Chen, L. Christensen, and J. R. Dahn, "Large-volume-change electrodes for Li-ion batteries of amorphous alloy particles held by elastomeric tethers," *Electrochem. commun.*, vol. 5, no. 11, pp. 919–923, 2003.

[8]   D. Linden and T. B. Reddy, *Handbook of Batteries*, 3d ed. McGraw-Hil.

[9]   K. Hayashi, Y. Nemoto, S. Tobishima, and J. Yamaki, "Mixed solvent electrolyte for high voltage lithium metal secondary cells," *Electrochim. Acta*, vol. 44, pp. 2337–2344, 1999.

[10]   X. Zhang, R. Kostecki, T. J. Richardson, J. K. Pugh, and P. N. Ross, "Electrochemical and infrared studies of the reduction of organic carbonates," *J. Electrochem. Soc.*, vol. 148, no. 12, pp. A1341–A1345, 2001.

[11]   J. R. Dahn, "Studies of Lithium Intercalation into Carbons Using Nonaqueous Electrochemical Cells," *J. Electrochem. Soc.*, vol. 137, no. 7, pp. 3–7, 2009.

[12]   A. Abouimrane, J. Ding, and I. J. Davidson, "Liquid electrolyte based on lithium bis-fluorosulfonyl imide salt: Aluminum corrosion studies and lithium ion battery investigations," *J. Power Sources*, vol. 189, no. 1, pp. 693–696, 2009.

[13]   K. Edström, M. Herstedt, and D. P. Abraham, "A new look at the solid electrolyte interphase on graphite anodes in Li-ion batteries," *J. Power Sources*, vol. 153, no. 2, pp. 380–384, 2006.

[14]   P. Verma, P. Maire, and P. Novák, "A review of the features and analyses of the solid electrolyte interphase in Li-ion batteries," *Electrochim. Acta*, vol. 55, no. 22, pp. 6332–6341, 2010.

[15]   D. Aurbach, "The Study of Li-Graphite Intercalation Processes in Several Electrolyte Systems Using In Situ X-Ray Diffraction," *J. Electrochem. Soc.*, vol. 142, no. 6, p. 1746, 1995.

[16]   J. Zheng, H. Zheng, R. Wang, L. Ben, W. Lu, L. L. Chen, L. L. Chen, and H. Li, "3D visualization of inhomogeneous multi-layered structure and Young's modulus of the solid electrolyte interphase (SEI) on silicon anodes for lithium ion batteries.," *Phys. Chem. Chem. Phys.*, vol. 16, no. 26, pp. 13229–38, 2014.

[17]   S. S. Zhang, K. Xu, and T. R. Jow, "EIS study on the formation of solid electrolyte interface in Li-ion battery," *Electrochim. Acta*, vol. 51, no. 8–9, pp. 1636–1640, 2006.

[18]   B. La, L. Eude, J. Pereira-ramos, and C. Sorin, "Silicon nanowires as negative electrode for lithium-ion microbatteries," *Electrochim. Acta*, vol. 53, pp. 5528–5532, 2008.

[19]   J. K. Lee, C. Oh, N. Kim, J.-Y. Hwang, and Y.-K. Sun, "Rational design of silicon-based composites for high-energy storage devices," *J. Mater. Chem. A*, vol. 4, no. 15, pp. 5366–5384, 2016.

[20]   C. J. Wen and R. A. Huggins, "Chemical Diffusion in Intermediate Phases in the Lithium-Silicon System Department of Materials Science and Engineering , Stanford University ," vol. 278, pp. 271–278, 1981.

[21]   P. Limthongkul, Y.-I. Jang, N. J. Dudney, and Y.-M. Chiang, "Electrochemically-driven solid-state amorphization in lithium–metal anodes," *J. Power Sources*, vol. 119–121, pp. 604–609, Jun. 2003.

[22]   P. Limthongkul, Y.-I. Jang, N. J. Dudney, and Y.-M. Chiang, "Electrochemically-driven

solid-state amorphization in lithium–metal anodes," *J. Power Sources*, vol. 119–121, pp. 604–609, Jun. 2003.

[23] C. K. Chan, H. Peng, G. A. O. Liu, K. Mcilwrath, X. F. Zhang, R. A. Huggins, and Y. I. Cui, "High-performance lithium battery anodes using silicon nanowires," pp. 31–35, 2008.

[24] G. Ji, Y. Ma, and J. Y. Lee, "Mitigating the initial capacity loss (ICL) problem in high-capacity lithium ion battery anode materials," *J. Mater. Chem.*, vol. 21, no. 27, pp. 9819–9824, 2011.

[25] M. J. Chon, V. A. Sethuraman, A. McCormick, V. Srinivasan, and P. R. Guduru, "Real-Time Measurement of Stress and Damage Evolution during Initial Lithiation of Crystalline Silicon," *Phys. Rev. Lett.*, vol. 107, no. 4, pp. 45503-1-45503–4, Jul. 2011.

[26] X. H. Liu, J. W. Wang, S. Huang, F. Fan, X. Huang, Y. Liu, S. Krylyuk, J. Yoo, S. a Dayeh, A. V Davydov, S. X. Mao, S. T. Picraux, S. Zhang, J. Li, T. Zhu, and J. Y. Huang, "In situ atomic-scale imaging of electrochemical lithiation in silicon.," *Nat. Nanotechnol.*, vol. 7, no. 11, pp. 749–56, Nov. 2012.

[27] M. N. Obrovac and L. Christensen, "Structural Changes in Silicon Anodes during Lithium Insertion/Extraction," *Electrochem. Solid-State Lett.*, vol. 7, no. 5, p. A93, 2004.

[28] T. D. Hatchard and J. R. Dahn, "In Situ XRD and Electrochemical Study of the Reaction of Lithium with Amorphous Silicon," *J. Electrochem. Soc.*, vol. 151, no. 6, p. A838, 2004.

[29] H. Wu and Y. Cui, "Designing nanostructured Si anodes for high energy lithium ion batteries," *Nano Today*, vol. 7, no. 5, pp. 414–429, Oct. 2012.

[30] H. Wu, G. Chan, J. W. Choi, I. Ryu, Y. Yao, M. T. McDowell, S. W. Lee, A. Jackson, Y. Yang, L. Hu, and Y. Cui, "Stable cycling of double-walled silicon nanotube battery anodes through solid-electrolyte interphase control.," *Nat. Nanotechnol.*, vol. 7, no. 5, pp. 310–5, May 2012.

[31] U. Kasavajjula, C. Wang, and A. J. Appleby, "Nano- and bulk-silicon-based insertion anodes for lithium-ion secondary cells," *J. Power Sources*, vol. 163, no. 2, pp. 1003–1039, Jan. 2007.

[32] H. Jung, M. Park, Y. G. Yoon, G. B. Kim, and S. K. Joo, "Amorphous silicon anode for

lithium-ion rechargeable batteries," *J. Power Sources*, vol. 115, no. 2, pp. 346–351, 2003.

[33]   J. Li and J. R. Dahn, "An In Situ X-Ray Diffraction Study of the Reaction of Li with Crystalline Si," *J. Electrochem. Soc.*, vol. 154, no. 3, pp. A156–A161, 2007.

[34]   M. N. Obrovac and L. J. Krause, "Reversible Cycling of Crystalline Silicon Powder," *J. Electrochem. Soc.*, vol. 154, no. 2, pp. A103–A108, 2007.

[35]   J. Yang, M. Winter, and J. O. Besenhard, "Small particle size multiphase Li-alloy anodes for lithium-ion- batteries," vol. 90, pp. 281–287, 1996.

[36]   M. Pharr, K. Zhao, X. Wang, Z. Suo, and J. J. Vlassak, "Kinetics of initial lithiation of crystalline silicon electrodes of lithium-ion batteries.," *Nano Lett.*, vol. 12, no. 9, pp. 5039–47, Sep. 2012.

[37]   H. Li, "A High Capacity Nano-Si Composite Anode Material for Lithium Rechargeable Batteries," *Electrochem. Solid-State Lett.*, vol. 2, no. 11, p. 547, 1999.

[38]   J. O. Besenhard, J. Yang, and M. Winter, "Will advanced lithium-alloy anodes have a chance in lithium-ion batteries?," *J. Power Sources*, vol. 68, no. 1, pp. 87–90, Sep. 1997.

[39]   H. Gleiter, "Nanocystalline Materials," *Prog. Mater. Sci.*, vol. 33, pp. 223–315, 1990.

[40]   X. H. Liu, L. Zhong, S. Huang, S. X. Mao, T. Zhu, and J. Y. Huang, "Size-Dependent Fracture of Silicon," *ACS Nano*, vol. 6, no. 2, pp. 1522–1531, 2012.

[41]   T. H. Hwang, Y. M. Lee, B.-S. Kong, J.-S. Seo, and J. W. Choi, "Electrospun core-shell fibers for robust silicon nanoparticle-based lithium ion battery anodes.," *Nano Lett.*, vol. 12, no. 2, pp. 802–807, Feb. 2012.

[42]   J.-S. Bridel, T. Azaïs, M. Morcrette, J.-M. Tarascon, and D. Larcher, "Key Parameters Governing the Reversibility of Si/Carbon/CMC Electrodes for Li-Ion Batteries †," *Chem. Mater.*, vol. 22, no. 3, pp. 1229–1241, Feb. 2010.

[43]   I. Ryu, J. W. Choi, Y. Cui, and W. D. Nix, "Size-dependent fracture of Si nanowire battery anodes," *J. Mech. Phys. Solids*, vol. 59, no. 9, pp. 1717–1730, Sep. 2011.

[44]   T. Song, J. Xia, J.-H. Lee, D. H. Lee, M.-S. Kwon, J.-M. Choi, J. Wu, S. K. Doo, H. Chang, W.

Il Park, D. S. Zang, H. Kim, Y. Huang, K.-C. Hwang, J. a Rogers, and U. Paik, "Arrays of sealed silicon nanotubes as anodes for lithium ion batteries.," *Nano Lett.*, vol. 10, no. 5, pp. 1710–6, May 2010.

[45]   M.-H. Park, M. G. Kim, J. Joo, K. Kim, J. Kim, S. Ahn, Y. Cui, and J. Cho, "Silicon nanotube battery anodes.," *Nano Lett.*, vol. 9, no. 11, pp. 3844–3847, Nov. 2009.

[46]   J. Graetz, C. C. Ahn, R. Yazami, and B. Fultz, "Highly Reversible Lithium Storage in Nanostructured Silicon," *Electrochem. Solid-State Lett.*, vol. 6, no. 9, p. A194, 2003.

[47]   S. Bourderau, T. Brousse, and D. M. Schleich, "Amorphous silicon as a possible anode material for Li-ion batteries," *J. Power Sources*, vol. 81–82, no. 1–2, pp. 233–236, 1999.

[48]   M. Ge, J. Rong, X. Fang, A. Zhang, Y. Lu, and C. Zhou, "Scalable preparation of porous silicon nanoparticles and their application for lithium-ion battery anodes," *Nano Res.*, vol. 6, no. 3, pp. 174–181, Feb. 2013.

[49]   J. Zhu, C. Gladden, N. Liu, Y. Cui, and X. Zhang, "Nanoporous silicon networks as anodes for lithium ion batteries.," *Phys. Chem. Chem. Phys.*, vol. 15, no. 2, pp. 440–3, Jan. 2013.

[50]   H. Kim, B. Han, J. Choo, and J. Cho, "Three-Dimensional Porous Silicon Particles for Use in High-Performance Lithium Secondary Batteries," *Angew. Chemie*, vol. 120, no. 52, pp. 10305–10308, Dec. 2008.

[51]   B. M. Bang, J.-I. Lee, H. Kim, J. Cho, and S. Park, "High-Performance Macroporous Bulk Silicon Anodes Synthesized by Template-Free Chemical Etching," *Adv. Energy Mater.*, vol. 2, no. 7, pp. 878–883, Jul. 2012.

[52]   H.-C. Shin, J. a. Corno, J. L. Gole, and M. Liu, "Porous silicon negative electrodes for rechargeable lithium batteries," *J. Power Sources*, vol. 139, no. 1–2, pp. 314–320, 2005.

[53]   J. Cho, "Porous Si anode materials for lithium rechargeable batteries," *J. Mater. Chem.*, vol. 20, no. 20, p. 4009, 2010.

[54]   M. Thakur, S. L. Sinsabaugh, M. J. Isaacson, M. S. Wong, and S. L. Biswal, "Inexpensive method for producing macroporous silicon particulates (MPSPs) with pyrolyzed polyacrylonitrile for lithium ion batteries.," *Sci. Rep.*, vol. 2, p. 795, Jan. 2012.

[55] J. Park, G.-P. Kim, I. Nam, S. Park, and J. Yi, "One-pot synthesis of silicon nanoparticles trapped in ordered mesoporous carbon for use as an anode material in lithium-ion batteries.," *Nanotechnology*, vol. 24, no. 2, pp. 1–7, Jan. 2013.

[56] Y. Xu, Y. Zhu, and C. Wang, "Mesoporous carbon/silicon composite anodes with enhanced performance for lithium-ion batteries," *J. Mater. Chem. A*, vol. 2, no. 25, pp. 9751–9757, 2014.

[57] Q. Zhang, Z. Yu, P. Du, and C. Su, "Carbon Nanomaterials Used as Conductive Additives in Lithium Ion Batteries," *Recent Pat. Nanotechnol.*, vol. 4, no. 2, pp. 100–110, Jun. 2010.

[58] B. Marinho, M. Ghislandi, E. Tkalya, C. E. Koning, and G. de With, "Electrical conductivity of compacts of graphene, multi-wall carbon nanotubes, carbon black, and graphite powder," *Powder Technol.*, vol. 221, pp. 351–358, 2012.

[59] Y.-C. Yen, S.-C. Chao, H.-C. Wu, and N.-L. Wu, "Study on Solid-Electrolyte-Interphase of Si and C-Coated Si Electrodes in Lithium Cells," *J. Electrochem. Soc.*, vol. 156, no. 2, pp. A95–A102, 2009.

[60] A. M. Wilson and J. R. Dahn, "Lithium Insertion in Carbons Containing Nanodispersed Silicon," vol. 142, no. 2, 1995.

[61] G. X. Wang, J. Yao, and H. K. Liu, "Characterization of Nanocrystalline Si-MCMB Composite Anode Materials," *Electrochem. Solid-State Lett.*, vol. 7, no. 8, p. A250, 2004.

[62] Y. Kwon, G.-S. Park, and J. Cho, "Synthesis and electrochemical properties of lithium-electroactive surface-stabilized silicon quantum dots," *Electrochim. Acta*, vol. 52, no. 14, pp. 4663–4668, Apr. 2007.

[63] A. Magasinski, P. Dixon, B. Hertzberg, A. Kvit, J. Ayala, and G. Yushin, "High-performance lithium-ion anodes using a hierarchical bottom-up approach.," *Nat. Mater.*, vol. 9, no. 4, pp. 353–358, Apr. 2010.

[64] J. Deng, H. Ji, C. Yan, J. Zhang, W. Si, S. Baunack, S. Oswald, Y. Mei, and O. G. Schmidt, "Naturally Rolled-Up C/Si/C Trilayer Nanomembranes as Stable Anodes for Lithium-Ion Batteries with Remarkable Cycling Performance," *Angew. Chemie*, vol. 125, no. 8, pp. 2382–2386, Feb. 2013.

[65] T. D. Bogart, D. Oka, X. Lu, M. Gu, C. Wang, B. A. Korgel, and B. E. T. Al, "Lithium Ion Battery Peformance of Silicon Nanowires with Carbon Skin," no. 1, pp. 915–922, 2014.

[66] J. K. Lee, K. B. Smith, C. M. Hayner, and H. H. Kung, "Silicon nanoparticles-graphene paper composites for Li ion battery anodes.," *Chem. Commun. (Camb).*, vol. 46, no. 12, pp. 2025–7, Mar. 2010.

[67] S. Zhu, C. Zhu, J. Ma, Q. Meng, Z. Guo, Z. Yu, T. Lu, Y. Li, D. Zhang, and W. M. Lau, "Controlled fabrication of Si nanoparticles on graphene sheets for Li-ion batteries," *RSC Adv.*, vol. 3, no. 17, p. 6141, 2013.

[68] J.-G. Ren, Q.-H. Wu, G. Hong, W.-J. Zhang, H. Wu, K. Amine, J. Yang, and S.-T. Lee, "Silicon-Graphene Composite Anodes for High-Energy Lithium Batteries," *Energy Technol.*, vol. 1, no. 1, pp. 77–84, Jan. 2013.

[69] R. Yi, J. Zai, F. Dai, M. L. Gordin, and D. Wang, "Dual conductive network-enabled graphene/Si–C composite anode with high areal capacity for lithium-ion batteries," *Nano Energy*, vol. 6, pp. 211–218, May 2014.

[70] D. P. Wong, R. Suriyaprabha, R. Yuvakumar, V. Rajendran, Y.-T. Chen, B.-J. Hwang, L.-C. Chen, and K.-H. Chen, "Binder-free rice husk-based silicon–graphene composite as energy efficient Li-ion battery anodes," *J. Mater. Chem. A*, vol. 2, no. 33, p. 13437, Jun. 2014.

[71] X.-L. Wang and W.-Q. Han, "Graphene enhances Li storage capacity of porous single-crystalline silicon nanowires," *ACS Appl. Mater. Interfaces*, vol. 2, no. 12, pp. 3709–13, Dec. 2010.

[72] K. Evanoff, J. Benson, M. Schauer, I. Kovalenko, D. Lashmore, and W. J. Ready, "Ultra Strong Silicon-Coated Carbon Nanotube Nonwoven Fabric as a Battery Anode," no. 11, pp. 9837–9845, 2012.

[73] K.-S. Park, K.-M. Min, S.-D. Seo, G.-H. Lee, H.-W. Shim, and D.-W. Kim, "Self-supported multi-walled carbon nanotube-embedded silicon nanoparticle films for anodes of Li-ion batteries," *Mater. Res. Bull.*, vol. 48, no. 4, pp. 1732–1736, Apr. 2013.

[74] A. Gohier, B. Laïk, K.-H. Kim, J.-L. Maurice, J.-P. Pereira-Ramos, C. S. Cojocaru, and P. Van Tran, "High-rate capability silicon decorated vertically aligned carbon nanotubes

for Li-ion batteries.," *Adv. Mater.*, vol. 24, no. 19, pp. 2592–7, May 2012.

[75]   L. Cui, Y. Yang, C. Hsu, and Y. Cui, "Carbon - Silicon Core - Shell Nanowires as High Capacity Electrode for Lithium Ion Batteries," *Nano Lett.*, vol. 9, pp. 1–5, 2009.

[76]   J. L. Gómez-Cámer, J. Morales, and L. Sánchez, "Anchoring Si nanoparticles to carbon nanofibers: an efficient procedure for improving Si performance in Li batteries," *J. Mater. Chem.*, vol. 21, no. 3, p. 811, 2011.

[77]   S. A. Klankowski, R. A. Rojeski, B. A. Cruden, J. Liu, J. Wu, and J. Li, "A high-performance lithium-ion battery anode based on the core–shell heterostructure of silicon-coated vertically aligned carbon nanofibers," *J. Mater. Chem. A*, vol. 1, no. 4, p. 1055, 2013.

[78]   Y. Yao, K. Huo, L. Hu, N. Liu, J. J. Cha, M. T. McDowell, P. K. Chu, and Y. Cui, "Highly Conductive , Mechanically Robust , and Electrochemically Inactive," *ACS Nano*, vol. 5, pp. 8346–8351, 2011.

[79]   A. Magasinski, B. Zdyrko, I. Kovalenko, B. Hertzberg, R. Burtovyy, C. F. Huebner, T. F. Fuller, I. Luzinov, and G. Yushin, "Toward efficient binders for Li-ion battery Si-based anodes: polyacrylic acid.," *ACS Appl. Mater. Interfaces*, vol. 2, no. 11, pp. 3004–10, Nov. 2010.

[80]   J. Li, L. Christensen, M. N. Obrovac, K. C. Hewitt, and J. R. Dahn, "Effect of Heat Treatment on Si Electrodes Using Polyvinylidene Fluoride Binder," *J. Electrochem. Soc.*, vol. 155, no. 3, p. A234, 2008.

[81]   J. Li, R. B. Lewis, and J. R. Dahn, "Sodium Carboxymethyl Cellulose : A Potential Binder for Si Negative Electrodes for Li-Ion Batteries Jing," *Electrochem. Solid-State Lett.*, vol. 10, no. 2, p. A17, 2007.

[82]   L. Chen, X. Xie, J. Xie, K. Wang, and J. Yang, "Binder effect on cycling performance of silicon/carbon composite anodes for lithium ion batteries," *J. Appl. Electrochem.*, vol. 36, no. 10, pp. 1099–1104, Aug. 2006.

[83]   Y. Park, S. Lee, S.-H. Kim, B. Y. Jang, J. S. Kim, S. M. Oh, J.-Y. Kim, N.-S. Choi, K. T. Lee, and B.-S. Kim, "A photo-cross-linkable polymeric binder for silicon anodes in lithium ion batteries," *RSC Adv.*, vol. 3, no. 31, p. 12625, 2013.

[84]   M. Murase, N. Yabuuchi, Z. Han, J. Son, Y. Cui, and H. Oji, "Crop-Derived

Polysaccharides as Binders for High-Capacity Silicon / Graphite-Based Electrodes in Lithium-Ion Batteries," *ChemSusChem*, vol. 5198, pp. 2307–2311, 2012.

[85]   I. Kovalenko, B. Zdyrko, A. Magasinski, B. Hertzberg, Z. Milicev, R. Burtovyy, I. Luzinov, and G. Yushin, "A major constituent of brown algae for use in high-capacity Li-ion batteries.," *Science*, vol. 334, no. 6052, pp. 75–9, Oct. 2011.

[86]   S. S. Zhang, "A review on electrolyte additives for lithium-ion batteries," *J. Power Sources*, vol. 162, no. 2, pp. 1379–1394, Nov. 2006.

[87]   S. Dalavi, P. Guduru, and B. L. Lucht, "Performance Enhancing Electrolyte Additives for Lithium Ion Batteries with Silicon Anodes," *J. Electrochem. Soc.*, vol. 159, no. 5, pp. A642–A646, 2012.

[88]   I. A. Profatilova, C. Stock, A. Schmitz, S. Passerini, and M. Winter, "Enhanced thermal stability of a lithiated nano-silicon electrode by fluoroethylene carbonate and vinylene carbonate," *J. Power Sources*, vol. 222, pp. 140–149, 2013.

[89]   C. C. Nguyen and B. L. Lucht, "Comparative Study of Fluoroethylene Carbonate and Vinylene Carbonate for Silicon Anodes in Lithium Ion Batteries," *J. Electrochem. Soc.*, vol. 161, no. 12, pp. A1933–A1938, 2014.

[90]   L. Martin, H. Martinez, M. Ulldemolins, B. Pecquenard, and F. Le Cras, "Evolution of the Si electrode/electrolyte interface in lithium batteries characterized by XPS and AFM techniques: The influence of vinylene carbonate additive," *Solid State Ionics*, vol. 215, pp. 36–44, 2012.

[91]   M. Ulldemolins, F. Le Cras, B. Pecquenard, V. P. Phan, L. Martin, and H. Martinez, "Investigation on the part played by the solid electrolyte interphase on the electrochemical performances of the silicon electrode for lithium-ion batteries," *J. Power Sources*, vol. 206, pp. 245–252, May 2012.

[92]   C. Xu, F. Lindgren, B. Philippe, M. Gorgoi, F. Björefors, K. Edstrom, and T. Gustafsson, "Improved Performance of Silicon Anode for Li-Ion Batteries: Understanding the Surface Modification Mechanism of Fluoroethylene Carbonate as an Effective Electrolyte Additive," *Chem. Mater.*, 2015.

[93]   X. Chen, X. Li, D. Mei, J. Feng, M. Y. Hu, J. Hu, M. Engelhard, J. Zheng, W. Xu, J. Xiao, J. Liu, and J. G. Zhang, "Reduction mechanism of fluoroethylene carbonate for stable

solid-electrolyte interphase film on silicon anode," *ChemSusChem*, vol. 7, no. 2, pp. 549–554, 2014.

[94]   M.-Q. Li, M.-Z. Qu, X.-Y. He, and Z.-L. Yu, "Electrochemical Performance of Si/Graphite/Carbon Composite Electrode in Mixed Electrolytes Containing LiBOB and LiPF," *J. Electrochem. Soc.*, vol. 156, no. 4, pp. A294–A298, 2009.

[95]   G. B. Han, M. H. Ryou, K. Y. Cho, Y. M. Lee, and J. K. Park, "Effect of succinic anhydride as an electrolyte additive on electrochemical characteristics of silicon thin-film electrode," *J. Power Sources*, vol. 195, no. 11, pp. 3709–3714, 2010.

[96]   Y. Li, G. Xu, Y. Yao, L. Xue, S. Zhang, Y. Lu, O. Toprakci, and X. Zhang, "Improvement of cyclability of silicon-containing carbon nanofiber anodes for lithium-ion batteries by employing succinic anhydride as an electrolyte additive," *J. Solid State Electrochem.*, vol. 17, no. 5, pp. 1393–1399, 2013.

[97]   G.-B. Han, J.-N. Lee, J. W. Choi, and J.-K. Park, "Tris(pentafluorophenyl) borane as an electrolyte additive for high performance silicon thin film electrodes in lithium ion batteries," *Electrochim. Acta*, vol. 56, no. 24, pp. 8997–9003, 2011.

[98]   K. Xu, U. Lee, S. S. Zhang, and T. R. Jow, "Graphite/Electrolyte Interface Formed in LiBOB-Based Electrolytes," *J. Electrochem. Soc.*, vol. 151, no. 12, pp. A144–A148, 2004.

[99]   J. K. Lee, C. Oh, N. Kim, J.-Y. Hwang, and Y.-K. Sun, "Rational design of silicon-based composites for high-energy storage devices," *J. Mater. Chem. A*, vol. 4, no. 15, pp. 5366–5384, 2016.

[100]   R. Dash and S. Pannala, "Theoretical Limits of Energy Density in Silicon-Carbon Composite Anode Based Lithium Ion Batteries," *Sci. Rep.*, vol. 6, no. February, p. 27449, 2016.

[101]   H. Yang, P. Fu, H. Zhang, Y. Song, Z. Zhou, M. Wu, L. Huang, and G. Xu, "Amorphous Si film anode coupled with LiCoO2 cathode in Li-ion cell," *J. Power Sources*, vol. 174, no. 2, pp. 533–537, Dec. 2007.

[102]   J. Yin, M. Wada, K. Yamamoto, Y. Kitano, S. Tanase, and T. Sakai, "Micrometer-Scale Amorphous Si Thin-Film Electrodes Fabricated by Electron-Beam Deposition for Li-Ion Batteries," *J. Electrochem. Soc.*, vol. 153, no. 3, pp. 472–477, 2006.

[103] R. Kataoka, T. Mukai, A. Yoshizawa, and T. Sakai, "Development of Li-Ion Rechargeable Battery Using SnC2O4-Coated Si Anode Material and Its Safety Evaluation," *J. Electrochem. Soc.*, vol. 160, no. 10, pp. A1684–A1689, 2013.

[104] L. Ji, H. Zheng, A. Ismach, Z. Tan, S. Xun, E. Lin, V. Battaglia, V. Srinivasan, and Y. Zhang, "Graphene/Si multilayer structure anodes for advanced half and full lithium-ion cells," *Nano Energy*, vol. 1, no. 1, pp. 164–171, 2012.

[105] J.-G. Ren, Q.-H. Wu, G. Hong, W.-J. Zhang, H. Wu, K. Amine, J. Yang, and S.-T. Lee, "Silicon-Graphene Composite Anodes for High-Energy Lithium Batteries," *Energy Technol.*, vol. 1, no. 1, pp. 77–84, Jan. 2013.

[106] W. Sun, R. Hu, H. Liu, M. Zeng, L. Yang, H. Wang, and M. Zhu, "Embedding nano-silicon in graphene nanosheets by plasma assisted milling for high capacity anode materials in lithium ion batteries," *J. Power Sources*, vol. 268, pp. 610–618, 2014.

[107] G. . Wang, J. . Ahn, J. Yao, S. Bewlay, and H. . Liu, "Nanostructured Si–C composite anodes for lithium-ion batteries," *Electrochem. commun.*, vol. 6, no. 7, pp. 689–692, Jul. 2004.

[108] C. Lin and J. a. Ritter, "Effect of synthesis pH on the structure of carbon xerogels," *Carbon N. Y.*, vol. 35, no. 9, pp. 1271–1278, 1997.

[109] S. A. Al-Muhtaseb and J. A. Ritter, "Preparation and Properties of Resorcinol-Formaldehyde Organic and Carbon Gels," *Adv. Mater.*, vol. 15, no. 2, pp. 101–114, Jan. 2003.

[110] C. Chartier, S. Bastide, and C. Levy-Clement, "Metal-assisted chemical etching of silicon in HF-H2O2," *Electrochim. Acta*, vol. 53, no. 17, pp. 5509–5516, 2008.

[111] Françoise Rouquerol, J. Rouquerol, and K. Sing, "Assessment of Mesoporosity," 1994.

[112] S. Tougaard, "Universality Classes of Inelastic Electron Scattering Cross-sections," *Surf. Interface Anal.*, vol. 25, no. November 1996, pp. 137–154, 1997.

[113] S. Komaba, K. Shimomura, N. Yabuuchi, T. Ozeki, H. Yui, and K. Konno, "Study on polymer binders for high-capacity SiO negative electrode of Li-Ion batteries," *J. Phys. Chem. C*, vol. 115, no. 27, pp. 13487–13495, 2011.

[114] A. P. Belen Molina-Concha, N. Murer, and J.-P. Diard, "Z Fit and multiple impedance

diagrams fitting," vol. 1. pp. 31–34, 2013.

[115] I. Bloom, L. K. Walker, J. K. Basco, D. P. Abraham, J. P. Christophersen, and C. D. Ho, "Differential voltage analyses of high-power lithium-ion cells. 4. Cells containing NMC," *J. Power Sources*, vol. 195, no. 3, pp. 877–882, 2010.

[116] Y.-S. Hu, R. Demir-Cakan, M.-M. Titirici, J.-O. Müller, R. Schlögl, M. Antonietti, and J. Maier, "Superior storage performance of a Si@SiOx/C nanocomposite as anode material for lithium-ion batteries.," *Angew. Chem. Int. Ed. Engl.*, vol. 47, no. 9, pp. 1645–1649, Jan. 2008.

[117] H. Yang, Y. Yan, Y. Liu, F. Zhang, R. Zhang, Y. Meng, M. Li, S. Xie, B. Tu, and D. Zhao, "A Simple Melt Impregnation Method to Synthesize Ordered Mesoporous Carbon and Carbon Nanofiber Bundles with Graphitized Structure from Pitches," *J. Phys. Chem*, pp. 17320–17328, 2004.

[118] C. Pérez-padrón, E. Lorenzo, N. E. Capuj, Z. Gaburro, C. J. Oton, and L. Pavesi, "Chemical etching effects in porous silicon layers," *Proc. SPIE*, vol. 5118, pp. 109–116, 2003.

[119] G. Beamson and Briggs D., *High Resolution XPS of Organic Polymers The Scienta ESCA300 Database*, no. January. Wiley, 1992.

[120] B. Guo, X. Wang, P. F. Fulvio, M. Chi, S. M. Mahurin, X. G. Sun, and S. Dai, "Soft-templated mesoporous carbon-carbon nanotube composites for high performance lithium-ion batteries," *Adv. Mater.*, vol. 23, no. 40, pp. 4661–4666, 2011.

[121] P.-Y. Chang, K. Bindumadhavan, and R.-A. Doong, "Size Effect of Ordered Mesoporous Carbon Nanospheres for Anodes in Li-Ion Battery," *Nanomaterials*, vol. 5, no. 4, pp. 2348–2358, 2015.

[122] Y. Fang, Y. Y. Lv, R. C. Che, H. Y. Wu, X. H. Zhang, D. Gu, G. F. Zheng, and D. Y. Zhao, "Two-Dimensional Mesoporous Carbon Nanosheets and Their Derived Graphene Nanosheets: Synthesis and Efficient Lithium Ion Storage," *J. Am. Chem. Soc.*, vol. 135, no. 4, pp. 1524–1530, 2013.

[123] J. Park, G.-P. Kim, I. Nam, S. Park, and J. Yi, "One-pot synthesis of silicon nanoparticles trapped in ordered mesoporous carbon for use as an anode material in lithium-ion batteries.," *Nanotechnology*, vol. 24, no. 2, Jan. 2013.

[124] B. E. Warren, "X-Ray Diffraction Study of Carbon Black," *J. Chem. Phys.*, vol. 2, no. 1934, pp. 551–555, 1934.

[125] J. R. Dahn, A. K. Sleigh, H. Shi, J. N. Reimers, Q. Zhong, and B. M. Way, "Dependence of the electrochemical intercalation of lithium in carbons on the crystal structure of the carbon," *Electrochim. Acta*, vol. 38, no. 9, pp. 1179–1191, 1993.

[126] M. Winter, R. Imhof, F. Joho, and P. Novák, "FTIR and DEMS investigations on the electroreduction of chloroethylene carbonate-based electrolyte solutions for lithium-ion cells," *J. Power Sources*, vol. 81–82, pp. 818–823, 1999.

[127] M. D. Levi, C. Wang, J. S. Gnanaraj, and D. Aurbach, "Electrochemical behavior of graphite anode at elevated temperatures in organic carbonate solutions," *J. Power Sources*, vol. 119–121, pp. 538–542, 2003.

[128] D. Dees, E. Gunen, D. Abraham, A. Jansen, and J. Prakash, "Electrochemical Modeling of Lithium-Ion Positive Electrodes during Hybrid Pulse Power Characterization Tests," *J. Electrochem. Soc.*, vol. 155, no. 8, pp. A1409–A1417, 2008.

[129] Z. P. Guo, Z. W. Zhao, H. K. Liu, and S. X. Dou, "Electrochemical lithiation and de-lithiation of MWNT-Sn/SnNi nanocomposites," *Carbon N. Y.*, vol. 43, no. 7, pp. 1392–1399, 2005.

[130] K. T. Lee and J. Cho, "Roles of nanosize in lithium reactive nanomaterials for lithium ion batteries," *Nano Today*, vol. 6, no. 1, pp. 28–41, 2011.

[131] N. Ding, J. Xu, Y. X. Yao, G. Wegner, X. Fang, C. H. Chen, and I. Lieberwirth, "Determination of the diffusion coefficient of lithium ions in nano-Si," *Solid State Ionics*, vol. 180, no. 2–3, pp. 222–225, Mar. 2009.

[132] K. Dokko, Y. Fujita, M. Mohamedi, M. Umeda, I. Uchida, and J. R. Selman, "Electrochemical impedance study of Li-ion insertion into mesocarbon microbead single particle electrode Part II . Disordered carbon," *Electrochim. Acta*, vol. 47, pp. 933–938, 2001.

[133] C. Ho, "Application of A-C Techniques to the Study of Lithium Diffusion in Tungsten Trioxide Thin Films," *J. Electrochem. Soc.*, vol. 127, no. 2, pp. 343–350, 1980.

[134] N. S. Choi, K. H. Yew, H. Kim, S. S. Kim, and W. U. Choi, "Surface layer formed on silicon thin-film electrode in lithium bis(oxalato) borate-based electrolyte," *J. Power*

Sources, vol. 172, no. 1, pp. 404–409, 2007.

[135] K. W. Schroder, J. Alvarado, T. A. Yersak, J. Li, N. Dudney, L. J. Webb, Y. S. Meng, and K. J. Stevenson, "The Effect of Fluoroethylene Carbonate as an Additive on the Solid Electrolyte Interphase on Silicon Lithium-ion Electrodes," *Chem. Mater.*, p. A-L, 2015.

[136] K. Xu, S. S. Zhang, U. Lee, J. L. Allen, and T. R. Jow, "LiBOB: Is it an alternative salt for lithium ion chemistry?," *J. Power Sources*, vol. 146, no. 1–2, pp. 79–85, 2005.

[137] V. L. Chevrier, L. Liu, D. B. Le, J. Lund, B. Molla, K. Reimer, L. J. Krause, L. D. Jensen, E. Figgemeier, and K. W. Eberman, "Evaluating Si-Based Materials for Li-Ion Batteries in Commercially Relevant Negative Electrodes," *J. Electrochem. Soc.*, vol. 161, no. 5, pp. A783–A791, 2014.

[138] R. Hausbrand, G. Cherkashinin, H. Ehrenberg, M. Gröting, K. Albe, C. Hess, and W. Jaegermann, "Fundamental degradation mechanisms of layered oxide Li-ion battery cathode materials: Methodology, insights and novel approaches," *Mater. Sci. Eng. B Solid-State Mater. Adv. Technol.*, vol. 192, no. C, pp. 3–25, 2015.

[139] R. Dedryvère, L. Gireaud, S. Grugeon, S. Laruelle, J. M. Tarascon, and D. Gonbeau, "Characterization of lithium alkyl carbonates by X-ray photoelectron spectroscopy: Experimental and theoretical study," *J. Phys. Chem. B*, vol. 109, no. 33, pp. 15868–15875, 2005.

[140] D. Aurbach, B. Markovsky, A. Shechter, and Y. Ein-Eli, "A Comparative Study of Synthetic Graphite and Li Electrodes in Electrolyte Solutions Based on Ethylene Carbonate-Dimethyl Carbonate Mixtures," *J. Electrochem. Soc.*, vol. 143, no. 12, pp. 3809–3820, 1996.

[141] F. A. Soto, Y. Ma, J. M. Martinez De La Hoz, J. M. Seminario, and P. B. Balbuena, "Formation and Growth Mechanisms of Solid-Electrolyte Interphase Layers in Rechargeable Batteries," *Chem. Mater.*, vol. 27, no. 23, pp. 7990–8000, 2015.

[142] A. J. Bard, L. R. Faulkner, N. York, C. @bullet, W. Brisbane, and S. E. Toronto, *Electrochemical Methods Fundamentals and Applications*. 1944.

[143] M. Y. Son, J. H. Kim, and Y. C. Kang, "Electrochemical Properties of 0.6Li2MnO3-0.4Li(Ni1/3Mn1/3Co1/3)O2 Composite Cathode Powders with Spherical Shape and Fine Size," *Int. J. Electrochem. Sci.*, vol. 8, pp. 2417–2429, 2013.

[144] R. Fathi, J. C. Burns, D. A. Stevens, H. Ye, C. Hu, G. Jain, E. Scott, C. Schmidt, and J. R. Dahn, "Ultra High-Precision Studies of Degradation Mechanisms in Aged LiCoO2/Graphite Li-Ion Cells," *J. Electrochem. Soc.*, vol. 161, no. 10, pp. A1572–A1579, 2014.

This work has been presented in the following:

Poster presentation

- "Embedded nano-Si in an Inactive Carbon Matrix as Anode Material for Li-ion Batteries" in Advanced Li-Battery Research Workshop, Liverpool, UK (April 2014)
- "Effects of HF etching on Electrochemical Performance of Silicon/Mesocarbon Composite" in 7th Advanced Battery Power, Aachen, Germany (April 2015)
- "Comparative study of Commercial Conductive Additive : Graphite and Super C65 for Si-based anode for Li-ion Batteries" in 7th European Summer School of Electrochemical Engineering, Leeuwarden, Netherlands (June 2015)
- "Stable Silicon/Mesoporous Carbon (Si/MC) Anode for Efficient Li-ion Batteries" in Greenlion Public Workshop, San Sebastian, Spain (October 2015)
- "Towards Si-based Anode for Li-ion Batteries for EV" in Flanders Make Symposium, Mechelen, Belgium (November 2016)

Oral presentation

- "Conductive Additive for Si/Mesoporous Carbon (Si/MC) Anode for Li-ion Batteries : Conductive Graphite vs Super C65" in 227th Electrochemical Society Conference, Chicago, USA (May 2015)
- "The effect of electrolyte additives on electrochemical performance of Silicon/Mesoporous Carbon (Si/MC) anode for LIB" in European Materials Research Society (EMRS) 2016 Fall meeting, Warsaw, Poland (September 2016)

Journal publications

- A. Rezqita, R. Hamid, S. Schwarz, H. Kronberger, A. Trifonova, Conductive Additive for Si/Mesoporous Carbon Anode for Li-Ion Batteries: Commercial Graphite vs Super C65, ECS Trans. 66 (2015) 17–27 (published).
- A. Rezqita, H. Vasilchina, M. Sauer, A. Foelske, H. Kronberger, A. Trifonova, Effect of HF etching on the properties of Si/mesoporous carbon (Si/MC) composite as anode material for Lithium ion Batteries, Ionics (under review).
- A. Rezqita, M. Sauer, A. Foelske, H. Kronberger, A. Trifonova, The effect of electrolyte additives on electrochemical performance of Silicon Mesoporous Carbon (Si/MC) anode for LIB, Electrochemical Acta (submitted).

Chapter of book :

A. Rezqita, H. Kronberger, and A. Trifonova, "Si-based Anode for Li-ion Batteries for Electrical Vehicle Applications," in *"EMVeM" –Energy efficiency management for Vehicles and Machines*, Katholieke Universiteit Leuven - Faculty of Engineering, 2016.

Arlavinda Rezqita

Personal Data

Place and Date of Birth:	Cirebon, Indonesia | 24 December 1989
Address:	Vorgartenstrasse 67/41, 1200 Vienna, Austria
email:	arlavinda.rezqita@gmail.com

Work Experience

Nov 2016 – present	Junior Scientist at AIT Austrian Institute of Technology GmbH, Vienna, Austria
Nov 2013 – Oct 2016	PhD fellow at AIT Austrian Institute of Technology GmbH, Vienna, Austria
May 2016	Visiting Researcher at KTH Royal Institute of Technology, Stockholm, Sweden
Feb – August 2013	Research Intern at Laboratoire de Réactivité et Chimie des Solides (Amiens, France) and Laboratoire de Recherche en Nanosciences (Reims, France)
July – August 2011	Process Engineer intern at PT. Petro Oxo Nusantara, Gresik, Indonesia
Aug 2009 - Jan 2010	Teaching Assistant at Bandung Institute of Technology, Bandung, Indonesia

Education

Nov 2013 – Oct 2016	Doctorate degree in Technical Chemistry, Vienna University of Technology , Austria

	Thesis: *"Efiicient Si-based anode for Li-ion batteries for electrical vehicles"* | Advisor: Prof. Trifonova Atanaska and Prof. Hermann Kronberger
Sept 2011 – Sept 2013	Master degree in Erasmus Mundus "Material Energy Storage and Conversion" program at Universite de Picardie Jules Verne, Amiens, France Universite Paul Sabatier III Toulouse, France (1st semester) Warsaw University of Technology, Poland (2nd semester) Universidad de Cordoba, Spain (3rd semester) Thesis *: "Elaboration of Si thin film for anode Li-ion microbatteries using electrodeposition in Ionic Liquids"* | Advisor: Dr. Claude Guery, M. Mathieu Morcrette, Dr. Jérémy Mallet
August 2007 – July 2011	Bachelor degree in Chemical Engineering, Bandung Institute of Technology, Indonesia Thesis : *"Usteady State Hydrogen Permeation Through Palladium Membrane in Presence of CO in Start-Up"* | Advisor: Dr. Yogi Wibisono and Dr. Irwan Noezar

Languages

English: Fluent
Indonesian: Mother tongue
German: Intermediate

Computer Skills

Intermediate Knowledge: Excel, Word, PowerPoint, OriginLab, ECLab
Basic Knowledge: MATLAB, Aspen HYSYS, LaTeX